Spring 1-1-2013

Dynamics, Control, and Fabrication of Micro Embedded Heaters and Sensors for Micro SMA Active Endoscopes

Sutha Aphanuphong
University of Colorado at Boulder, aphanups@colorado.edu

Dynamics, Control, and Fabrication of Micro Embedded Heaters and Sensors for Micro SMA Active Endoscopes

by

Sutha Aphanuphong

B.Eng., Computer Engineering, Prince of Songkla University, Thailand,

1999

M.S., Aerospace Engineering, University of Colorado at Boulder, 2008

A thesis submitted to the

Faculty of the Graduate School of the

University of Colorado in partial fulfillment

of the requirements for the degree of

Doctor of Philosophy

Department of Aerospace Engineering Sciences

2013

This thesis entitled:
Dynamics, Control, and Fabrication of Micro Embedded Heaters and Sensors for Micro SMA Active Endoscopes
written by Sutha Aphanuphong
has been approved for the Department of Aerospace Engineering Sciences

____

Dale A. Lawrence

____

Bart Van Zeghbroeck

Date ________________

The final copy of this thesis has been examined by the signatories, and we find that both the content and the form meet acceptable presentation standards of scholarly work in the above mentioned discipline.

Aphanuphong, Sutha (Ph.D., Aerospace Engineering)

Dynamics, Control, and Fabrication of Micro Embedded Heaters and Sensors for Micro SMA Active Endoscopes

Thesis directed by Professor Dale A. Lawrence

This research investigates design and control of an active catheter for minimally invasive medical procedures. Microfabrication techniques are developed and several prototypes were constructed. The understanding and analysis results from each design iteration are utilized to improve the overall design and the performance of each revision. An innovative co-fabrication method is explored to simplify the fabrication process and also improve the quality, repeatability, and reliability of the active catheter. This co-fabrication method enables a unique compact integrated heater and sensor film to be directly constructed on a shape memory alloy (SMA) sheet and to be utilized as an outline mask to pattern a micro SMA actuator. There are two functions integrated in the sensor film: heat sources to actuate the micro SMA actuator and sensors to provide temperature and strain of the active catheter to closed-loop control algorithms. Three main aspects are explored in this dissertation: thermal dynamics in the MicroFlex (μF) film and its effect on the sensor capabilities; non-minimum phase behavior and its effect on control performance, and film micro fabrication design and its effect on thermal dynamics. The sensor film developed from this understanding is able to deliver excellent heating and sensing performance with a simple design.

Dedication

To all my friends, family, and especially Nongluck Aphanuphong for their patience, understanding, motivation and encouragement.

Acknowledgements

This dissertation could not have been accomplished without the help of my advisor, Professor Dale A. Lawrence.

This research was funded by National Institutes of Health (NIH) under a Phase II STTR: MicroFlex Tools to Improve Sinus Diagnostics and Surgery.

Contents

Chapter

Tables

Table

Figures

Figure

Chapter 1

Introduction

Medical procedures can be divided into three main categories based upon their invasiveness: invasive, non-invasive, and minimally invasive procedures. Invasive procedures involve an incision to enable direct access to perform the medical procedure, e.g. organ transplant, neurosurgery, cardiac surgery, etc. Non-invasive procedures do not require any perforation, incision, catheterization or other entry into the body to perform the procedure, e.g. radiation therapy, lithotripsy, and electrocardiography, etc. Minimally invasive procedures or minimally invasive surgery (MIS) utilizes natural passages or small incisions to perform treatment with special instruments (e.g. endoscopes, laparoscopes, catheters etc.). MIS can remarkably shorten recovery time, lower patient risk, and in some cases, may transform the type of procedure from an inpatient treatment in a hospital to an outpatient procedure in a physician's office.

Some surgical procedures are not appropriate for MIS techniques because these procedures manipulate large organs and require large forces, e.g. colectomy, pneumonectomy, organ transplant, etc. Many other procedures could benefit from MIS with suitable advancement in instrument technology. For example, existing catheters are not small and flexible enough to navigate beyond the 4^{th} branch of the human lung, and they also do not provide direct visualization. Instruments designed for sinus surgery are not flexible enough to access sinus passages.

The small flexible catheters utilized in these procedures are passive, i.e. with no tip articulation, making it difficult to precisely control their tip. Endoscopes are active instruments also often used in MIS procedures. They contain fiber optic image guides and illumination to supply visualization but are limited by tip articulation and the stiffness of the image guide. Newer active catheters add articulation to allow operators to directly control the bending of their tip, but they have large bend radii, and few degrees of freedom, limiting their access through torturous passages, and their ability to work in small spaces.

This dissertation focuses on improving the capabilities of MIS active catheters. It utilizes technology first prototyped in the M.S. thesis [Aphanuphong, 2008]. This technology was developed under support from three grants from the National Institutes of Health (NIH), in cooperation with Quest Product Development Corporation. This was an ultra-flexible catheter, having the capability of direct visualization and direct multi degree of freedom control of its tip via embedded actuators. Two medical procedures were used to guide this technology development; sinus surgery and lung disease treatment. These provided different design objectives but were based on similar technology. However, there were several key problems with this first prototype. This dissertation is dedicated to study and understand those issues in depth, in order to improve the capabilities of active catheters. The specific research objectives are discussed in Section 2.3.

The remainder of this chapter provides background on existing catheter designs to place this work in context. The discussion is divided into the three main aspects: actuation, sensing, and control.

1.1 Actuator Designs

Active catheters can be divided into several categories, e.g, based on types of medical procedures, or based on materials/actuation methods. There are a variety of actuation methods, including hydraulic pressure based actuators, shape memory alloy (SMA) based actuators, and piezoelectric based actuators. In this dissertation, only SMA based actuators are emphasized because of their advantages. SMA is an alloy having two unique properties: the shape memory effect (SME) and pseudolasticity (PE). SME is a phenomenon whereby the deformed alloys can reverse transformation to their original shape when they are heated beyond their transition temperature. The recovery process happens when the crystal structure of the SMA transforms from the low temperature phase called "martensite" to the high temperature phase, which is stronger, called "austenite" by shear lattice distortion. During this phase transformation, the SMA also recovers the strain due to the deformation in the martensitic phase to its lower strain state (or its thermally set trained shape) in the austenitic phase. When the SMA is cooled down, the crystal structure is transformed from austenite back to martensite and the shape remains unchanged, if no external force is applied to the SMA. PE is a property of the SMA associated with stress-induced transformation, causing strain recovery upon unloading at the temperature above the SMA transition temperature. Both unique properties enable SMA to be utilized as actuators in active catheters, which can be activated by varying the amount of applied heat. The response speed of heat-activated actuators depends on their heating and cooling rates. In order to achieve fast response time, actuators must be small [Ikuta, 1990]. Fortunately, small size SMA actuators, resulting from small diameter active catheters, are desirable for MIS procedures.

SMA actuators have several advantages. SMA actuators are clean because they do not have friction, hence no lubricant is required. SMA actuators are quiet since they do not have motors or gears. Furthermore SMA actuators are easy to scale up, down or pattern to desired shapes because these actuators can be fabricated using microelectronic processes for patterning metals. On the other hand, SMA actuators also have various disadvantages, e.g., SMA is difficult to weld to other metals, SMA actuators cannot be large in size due to their heating and cooling rate limitations, the amount of strain recovery due to increased temperature is difficult to control because the relationship between temperature and strain is highly nonlinear and hysteretic. A control algorithm is needed to compensate for this nonlinearity in order to achieve the desired strain recovery. In addition, special sensors (e.g. temperature, strain/position or force sensors) are necessary to provide feedback of the SMA states to control algorithms.

There are two conventional heating methods for SMA actuators: direct and indirect heating. Both use a Joule-heating process (using electrical current). The direct heating method provides heat to the SMA by driving electrical current directly through the SMA itself, whereas indirect heating methods heat the SMA by applying electrical current through separate heating elements, which can transfer heat to the SMA by thermal conduction. The actuator geometry depends on the heating method. The direct heating method requires high resistance SMA actuators in order to reduce the applied heating current. Thus, the SMA actuators must have a small cross sectional area and a long length. The suitable shapes for these SMA actuators are wires and coil springs.

[Dario et al., 1991, 1997; Fukuda et al., 1994; Takizawa et al., 1999] employed SMA wires in their active catheters and utilized a flexible tube or a linear spring as a skeleton (a support structure of the catheter), and a flexible polymer to encapsulate the skeleton and SMA wires. The catheters were constructed from multiple short active segments. The SMA wires were placed inside lumen tubes (small tubes inside the sheath), which were on the side of skeleton along the longitudinal axis on every active segment. SMA wires on the active segments were fixed by bonding both ends of the SMA wires to the proximal end of the active segment, or one end of SMA wires to the proximal and the other end to the distal end of the active segment. In addition, each segment deflection could be individually controlled.

[Fu et al., 2006; Haga et al., 1998, 2001, 2005; Ikuta et al., 1988; Lim et al., 1995, 1996; Maeda et al., 1996; Park and Esashi, 1999] utilized SMA coil springs in their catheters. These catheters also used a flexible tube or a linear spring as their skeleton. Small SMA coil springs were attached along the longitudinal axis of each bending section of the catheters. There were two arrangements of the SMA coil springs: two SMA coil springs attached to the skeleton in antagonist pairs, and three small SMA coils attached at 120° apart around the skeleton. The whole catheter was encapsulated in a silicone sheath to isolate them from contacting their environment. Each active segment also could be individually bent.

Both types above are actuated by applying electrical current directly through SMA wires or coil springs to cause the actuators to contract. In order to individually control the deflection of each segment with this direct heating method, it is important that each segment is electrically isolated, hence only the SMA actuators with applied electrical current are heated. Most elements of these catheters are made from metals, thus it is difficult to achieve strong mechanical connections when every SMA actuator must be electrically insulated from the other SMA elements. Typically, these active catheters use polymer glues for mechanical attachment, which cannot provide strong and reliable mechanical connections.

In contrast, the indirect heating method does not need high resistance in the SMA. Although a large surface area is required to attach the heater elements. Hence, both SMA coil springs and wires are not in the appropriate shapes for this heating method. [Aramaki et al., 1995; Kaneko et al., 1996] utilized an indirect heating method in their active catheters. They used a flexible silicone tube as a skeleton. Each active segment had a long rectangular two-way SMA strip with three heater films attached on its surface. These active segments were attached to the silicone tube with glue. These catheters were actuated by applied electrical current to heaters on the SMA surface, causing the catheter tip to deflect. When the catheter tip was cooled down, the SMA actuators returned to their low temperature trained shapes, causing the tip to return to its nominal position. Because this design used glue to bond the SMA actuators, it could not provide strong mechanical connections and forces produced were very small.

Figure 1.1 is a CAD model of the active catheter, called "MicroFlex (μF) catheter", presented in the M.S. thesis [Aphanuphong, 2008]. This catheter employed a triangular-shape precipitation-hardening steel spring as its skeleton and used indirect heating as the actuation method. Three SMA actuator strips with a smooth contour shape were attached along the longitudinal axis of the skeleton at 120° spacing. The μF films, which were fabricated separately, were bonded on the surface of the SMA actuators during the assembly process. All active segments of the SMA actuators were compressed inward between the skeleton spring turns. These active segments had a flat trained shape. Hence, they pushed skeleton turn apart when they were heated by applying electrical current through the heater film on the SMA surface, called a "μF film", causing the tip to deflect. Stainless steel welding bands were wrapped around the SMA actuator strips and spot-welded to secure these actuators on the skeleton spring to provide strong mechanical connections.

The μF catheter is differentiated from the other active catheters primarily by the amount of force that can be produced. The μF catheter employs SMA actuator strips that have a relatively large cross sectional area compared the other active catheter designs (e.g. SMA wires, SMA coil

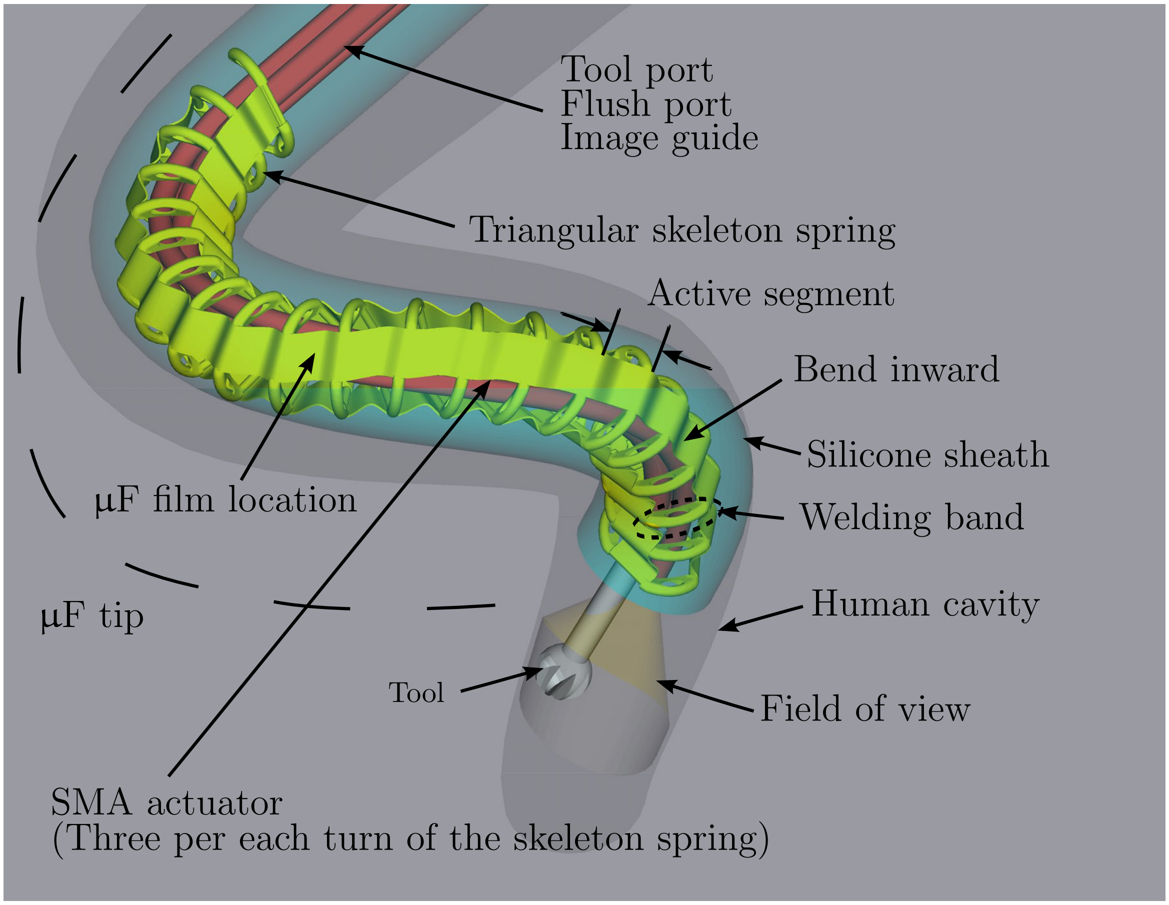

Figure 1.1: CAD drawing of a μF tip prototype presented in [Aphanuphong, 2008], drawing courtesy of Quest Product Development Corp.

springs). This large cross sectional area enables the μF catheter to generate larger force than the other SMA active catheters at the equivalent catheter diameter. In addition, metal welding bands and the spot-welding technique enable the μF catheter to achieve stronger mechanical connections than the other SMA actuators that use glued connections, enabling large actuator forces to be transferred to the catheter.

1.2 Sensor Designs

Temperature and position feedback are two methods employed to control the μF actuators. Common external sensing methods include thermocouples, linear variable differential transformers

(LVDT), and potentiometers. These sensing methods are not appropriate for controlling the μF actuators because of their size. Another approach utilizes SMA resistance but this method is impractical because the large SMA cross section makes the resistance too small to measure. [Aramaki et al., 1995; Kaneko et al., 1996] proposed a sensing method that integrated both temperature and position sensors into their heaters and used these multifunction integrated films (MIF) as both heating sources and sensors. MIF had one layer with two types of metal (titanium and platinum) connected in series. The titanium layer was used for both heating and sensing purposes, but the platinum layer was utilized for sensing only. This proposed MIF is not desirable because it utilizes an expensive metal (platinum), which also requires special equipment to deposit (e-beam evaporator). Also, the external sensing circuit is complex because it must switch between heating and sensing phases.

The μF tip prototype presented in [Aphanuphong, 2008] utilized a similar integrated thin film as both heater and sensor. This thin film was designed in a compact integrated form. It included temperature sensors, strain sensors and heaters. There were several differences between the μF film and the MIF film: the μF film could reduce manufacturing costs by using aluminum instead of platinum, the sensing circuit was simplified by eliminating the switching between heating and sensing modes, all heaters on the same strip are ganged in parallel and were designed to equally deliver heat in all segments. In addition, the μF film fabrication process utilized a metal sacrificial substrate to provide fast release from the substrate. Thin multiple metal layer structures were utilized as terminal pads to allow the signal interfacing cables to be soldered.

1.3 Control Techniques

Hysteresis nonlinearity in the SMA is a major challenge in control. There are many research groups proposing complex control methods as discussed below. SMA control methods can be divided to two major schemes: inversion/cancellation based schemes, and high gain feedback based schemes.

Inversion and cancellation based schemes handle the SMA hysteresis by canceling and inverting this nonlinearity. The control algorithm starts by identifying a nonlinear model of the actuator based on the relationship between the input (e.g., heating voltages, heating power) and the output (e.g., SMA resistance, position, temperature, force). Then a controller is designed to cancel and undo that nonlinearity, resulting a linearized SMA model. Finally, a linear control method is utilized to control the linearized SMA actuator model. The plant identification process is the most important task in this control scheme because inaccurate plant identification can cause imperfect cancellation and inversion, resulting an inaccurate linearized model to conduct closed-loop control design. In addition, a small variation on the actuator can cause significant change in its behavior. In this case, the actuator model must be periodically re-identified to produce an accurate linearized model. Control algorithms based on this scheme include [Arai et al., 1995; Dickinson and Wen, 1998; Hasegawa and Majima, 1998; Ma et al., 2004; Majima et al., 2001].

High gain feedback based schemes manage the SMA hysteresis by applying a tight feedback loop to swamp out the nonlinearity with a relatively large linear effect. The tight feedback loop can be achieved by using a high gain linear controller. In some cases, extremely accurate plant identification may not be necessary because this control scheme does not require any model inversion. Two high gain techniques commonly used in SMA actuator controls are variable structure control and high gain PID control. Variable structure control is an extreme version of the high gain PID control. This control method is a discontinuous control, which changes the structure of the controller or switches the controller when it reaches particular switching surfaces. SMA control algorithms based on a variable structure control method include [Elahinia and Ashrafiuon, 2002; Grant and Hayward, 1997a, 2000; Kai and Chengin, 2002]. On the other hand, high gain PID control is a basic method that has been used in many applications. SMA control algorithms based on the high gain PID control method include [Dickinson et al., 1996; Gorbet and Morris, 2003; Gorbet and Russell, 1995; Ikuta, 1990; Troisfontaine et al., 1997].

In this dissertation, the high gain PI control is used. This type of control is simple and it can provide reasonable stability and performance in both temperature and position feedback controls. The goal of this control design is to evaluate simple approaches to control the μF tip, and to provide a basis for understanding the capability of the SMA actuators associated with PI control methods.

1.4 Dissertation Outline

This dissertation is organized as follows. Chapter 2 begins with some more background on the first μF tip prototype design presented in the M.S. thesis [Aphanuphong, 2008], including the configuration of the μF tip and the design objectives. These design objectives are utilized as a baseline of the μF tip development in this dissertation. Then key problems with the first μF tip prototype are discussed since they provide the motivation for the 3 research questions of this dissertation, which are: "1) Is there a better way to attach the μF film to the SMA actuator?", "2) What causes the loops between temperature and strain signals in the μF film?", and "3) What causes the non-minimum phase dynamics?". Literature in strain sensing technology is then reviewed in detail. Finally, the specific research objectives of this dissertation are presented.

Chapter 3 introduces a signal conditioning circuit and a modified Wheatstone bridge, which are utilized to provide heating voltages to the μF tip and provide sensory information for feedback control algorithms. The calibration methods for extracting temperature and strain from the outputs of the signal condition circuit are discussed next. Then, a sinusoidal Electro-Thermo-Mechanical (ETM) model, which is used to analyze the source of the phase shift between $\frac{V_s}{V_h}$ and $\frac{V_t}{V_h}$, is discussed at the end of the this chapter.

Chapter 4 discusses the strain sensing technique and the effective gage factor of the μF film, the simple method to construct $\frac{V_s}{V_h}$ and $\frac{V_t}{V_h}$ model avoiding non-linearity of the SMA material, and the details of four design variations of the μF heaters/sensors (μF films) presented in the dissertation. A sinusoidal ETM model of each μF film design is constructed and utilized to understand the impact of each modification on the dynamics of the heaters/sensors. It is shown how the results of this study can improve the sensing performance of the μF film.

Chapter 5 introduces an innovative fabrication process, called "co-fabrication", which is utilized to construct the μF actuators in this dissertation. This fabrication method can increase reliability of the μF films, improve the alignment quality of the μF actuators, and reduce complexity of the μF tip construction.

Finally, Chapter 6 provides concluding remarks, a summary of the contributions of this dissertation, and suggested areas for future work.

Chapter 2

Background

The μF tip prototypes presented in this dissertation share similar design objectives with the first μF tip prototype developed in [Aphanuphong, 2008]. Hence, it is important to understand the fundamental requirements previously discussed in [Aphanuphong, 2008]. In addition, one must be aware of the problems discovered in the first μF tip prototype. Therefore, this chapter is focused on revisiting the design constraints and understanding the key issues that limit the capabilities of the μF design from [Aphanuphong, 2008]. To investigate solutions, alternative micro heating and sensing technologies are then reviewed. Finally the main research questions of this dissertation are introduced.

2.1 μF Tip Configuration in the M.S. Thesis

The principal goal of the μF tip presented in [Aphanuphong, 2008] was to demonstrate the feasibility of the μF catheter in both fabrication and usability. The study in the M.S. thesis showed that the μF tip prototype could be successfully fabricated and assembled. In addition, closed-loop temperature and position feedback control were implemented. The closed-loop temperature control had outstanding performance. The closed-loop position control performance was not satisfactory because it suffered from a non-minimum phase zero in the position control loop. The rest of this section reviews the key design objectives of this first μF tip prototype, as these were also used to guide the work in this dissertation.

2.1.1 Actuation Methods

As previously discussed in Section 1.1, shape memory alloys (SMA) were the selected actuators for μF tips. Hence the heating method to activate the SMA was the first design constraint that drove the design of the μF tip. It defined how the actuators were designed and built, what types of sensors were compatible and necessary, and finally, how the actuators, heating elements, and sensors were attached to the μF tip.

There are two types of heating methods. The first and most common is the direct heating method. This was not suitable for the μF tip, as noted earlier, because it demanded high resistance SMA actuators resulting in small cross sectional area SMA actuator designs. On the other hand, the indirect heating method used in the M.S. thesis did not have this limitation because it employed external heating elements. These were constructed separately from the SMA actuators and they were electrically insulated in a polymer. These heaters were attached to the SMA actuators during the assembly process.

The heaters in the μF tip in the M.S. thesis were designed as thin films consisting of long, narrow, and thin metal traces serving as resistors embedded between thin polymer layers. When electrical current was passed through these metal traces, the temperature of the metal traces increased due to power dissipation. At steady state, the temperature of these heaters above the ambient was proportional to the square of the electrical current applied to them. Since the heater films were thin and the SMA actuators had good thermal conduction and small thermal mass, the steady state temperature of the SMA actuators directly under the heater films was approximately the same as the temperature of the heaters.

2.1.2 Size, and Degree of Freedom of the μF Tips

The main factors that defined size and degrees of freedom (DOF) of the μF tips were determined by their medical applications. There were two initial applications for the μF architecture in the M.S. thesis. The first was for detection, diagnosis, and treatment of lung diseases. The μF tips for this application needed a cross section smaller than 1mm in order to navigate beyond the 4^{th} branch generation in the human lung. However, the ability to control each SMA actuator segment individually was not necessary because navigation in lung branches did not require complex bending. The second proposed application was for sinus diagnosis and surgery procedures. The μF tip for these procedures needed a cross section diameter smaller than 5mm in order to work in the sinus cavities. However, the size of the μF tips could not be too small because they could not produce appropriate forces to perform tasks required in these procedures. In addition, the tips had to be flexible and also have the ability to individually control the bending of each group of the actuator elements in order to pass through tortuous passages (e.g. to access maxillary sinuses from through the nasal opening).

From the above requirements, the resulting design of the μF tip presented in the M.S. thesis for lung procedures had 1mm diameter and had three SMA actuator strips wrapped around a skeleton spring at 120° apart. Each actuator strip had three actuator segments which were ganged together in parallel into a single set. This heater connection method did not allow operators to actuate each SMA actuator segment individually. Hence these μF tips could only bend into simple shapes (e.g. a C-shape). On the other hand, the μF tips for sinus procedures had an outside diameter of approximately 3mm due to higher forces required in these procedures. There were two actuator strips and a passive spine attached at 120° apart per each μF tip. Each actuator strip had twelve elements that were ganged into four sets of three elements in order to produce a suitable range of motion. This design allowed operators to send four individual heating commands per strip. In addition, with two actuator strips per tip, this configuration enabled the μF tips to bend in two independent directions per each ganged section for a total of eight degrees of freedom and the ability to bend into more complex shapes.

2.1.3 Shape of the μF SMA Actuators

By selecting the indirect heating method, the size of the SMA actuators was not constrained by a SMA resistance requirement. Hence the SMA actuators could be designed to maximize forces by increasing the SMA cross section area or maximize range of motion by optimizing the forces between SMA actuators and a skeleton spring. From the descriptions of medical applications in the prior section, the μF tips designed for lung procedures had a long narrow strip pattern with total dimension of 7400μm × 700μm. There were three SMA actuator elements per strip with the element size of 800μm × 700μm and a narrow neck width of 500μm. The SMA pattern had a smooth contour to avoid stress concentration areas. The thickness of the SMA pattern was also not uniform in order to compensate for the high bending stress areas due to the tight bend around the narrow hinge areas in the neck of each segment. Figure 2.1 is the lung-size SMA pattern, the dark brown color area indicates the areas of of 12.5μm thickness, and the light brown area indicates the areas of 25μm thickness. The small triangle notches at both ends of the strip are marks for aligning the μF film to the SMA actuator during assembly.

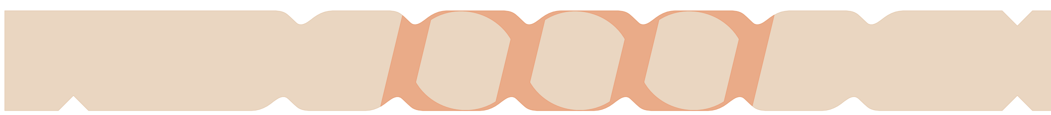

Figure 2.1: The μF actuator strip pattern with three SMA active elements presented in the M.S. thesis

2.1.4 Sensing Methods

Closed-loop temperature and position (strain) feedback were implemented to control the deflection of the μF tip. This section discusses the techniques used to measure both temperature and strain by the design of μF films.

Temperature Sensing Method Since SMA is activated by heat, temperature control is needed to ensure that the actuators follow the operator's commands in the presence of varying tissue contact (varying thermal paths). This is combined with visual feedback by the operator to position the tip. If the μF tip is not at the desired position, the operator can increase or decrease the actuation commands to correct the position. There are various methods to measure the temperature of the SMA actuators, e.g. thermocouples, infrared sensors, or SMA resistance (using the electro-thermal properties of the material). However, in minimally invasive surgery, external sensors are inappropriate because of their size and difficulty of micro-assembly. SMA resistance cannot be measured unless the actuators are electrically isolated, which is difficult to do when strong mechanical joints are needed, as noted earlier.

Instead, the resistance temperature detection (RTD) method is employed, using the electro-thermal properties of the existing heater/sensor layers. When the temperature of the heaters increase, their resistance could increase or decrease, depending on the coefficient of thermal expansion of the metal film, the coefficient of thermal expansion of the substrate, and the thickness and relative stiffness of the metal film and substrate [Hall, 1968; Warkusz, 1978]. The resulting property that quantifies the relationship between temperature and resistance is the Temperature Coefficient of Resistance (TCR). Most metals have a positive TCR, which means when the temperature increases, the resistance also increases. μF films utilize aluminum as a heater/sensor metal on a polyimide substrate, which results in a positive TCR. The most important benefit of the metal film temperature sensor was that it could be integrated into the heaters for an indirect heating method without any extra fabrication or assembly steps.

Position (Strain) Sensing Method For use in force feedback teleoperation, a means of sensing tissue contact force is needed. One approach [Hongan, 1985; Kim, 1992; Ni and Wang, 2004; Sherman et al., 2000; Tavakoli et al., 2005] is to use the error between desired and actual position in a position control loop as a proxy for this contact force. Position can be measured with several direct sensing techniques, for example, using a LVDT, using a potentiometer, etc. However, separate sensors would be cumbersome to integrate into a μF tip.

Tip position depends on a balance of antagonistic forces between the skeleton spring and the SMA actuators in both the austenitic and martensitic phases. At low temperature, the skeleton spring is stronger, causing compression of the SMA. At high temperature, the SMA becomes stronger than the spring, pushing the spring away to return to a flat shape. The curvature of the

SMA actuator varies between these two states, which causes surface strain variation. Hence SMA strain sensing provides a method to sense bending position of the tip.

The typical method to measure strain is to use strain gages. These are made from thin electrically conducing layers, and bonded to the substrate with insulating materials. Deformation of the substrate causes deformation in the strain gage, causing a change in resistance. The resistance variation due to strain depends on the Gage Factor, which is a function of gage material and layer pattern. These resistance changes are typically measured from voltage changes in a Wheatstone bridge circuit. These voltage measurements are subsequently calibrated to strains or positions. However, conventional strain gages are inappropriate for the μF design because they are large and difficult to integrate. Instead, the strain gage ideas was integrated into the design of the heater layers, as discussed below.

Integrated Temperature and Strain Sensing Methods A multifunction integrated film, which could be used as a heater, as well as a temperature and strain sensor, was proposed by [Aramaki et al., 1995; Kaneko et al., 1996]. The film consisted of a single heater/sensor layer with two different metals (titanium and platinum) encapsulated in polyimide. The strain sensing function of this film depended on the difference of titanium and platinum gage factors (titanium had a gage factor of −1.22, and platinum had a gage factor of 5.06). The advantage of this design was that it had only one heater/sensor layer, reducing complexity in fabrication. However, the two different types of metals required two metal deposition processes. In addition, platinum may be too costly for mass production.

The μF film in the M.S. thesis also used integrated heater/temperature and strain sensors. Two aluminum layers were used that had identical gage factors, but these layers were subjected to two different strains (compressive and tensile) because the neutral bending axis of the structure was located in between the aluminum layers. The advantage of this design was that it utilized aluminum as a heater/sensor metal layer, which is low cost and easy to deposit and pattern. However, this μF design used a soft silicone adhesive to attenuate the strain between the SMA surface and the μF film. This approach tremendously increased the complexity in fabrication and also significantly reduced strain sensitivity of the μF film.

When heater, temperature, and strain sensors were combined into one element, Wheatstone bridge circuits could no longer sense both temperature and strain concurrently. In the M.S. thesis, an alternative "modified Wheatstone bridge" was proposed and utilized to simultaneously sense both temperature and strain. When this circuit was integrated with specific calibration techniques, both temperature and strain could be extracted from the voltage differences measured from the bridge. This was also utilized in the dissertation research, hence details are discussed in Chapter 3.

2.1.5 Heater/Sensor Materials and Layout

Sputtered (amorphous) aluminum and polyimide were the selected materials for fabricating the μF films in both the M.S. thesis and in this dissertation. Sputtered aluminum had appropriate resistivity, enabling the required heater power dissipation with safe voltage levels. It also had superior mechanical properties with high ultimate tensile strength but low Young's modulus, enabling it to survive relatively high bending strain. Polyimide was chosen because it had good adhesion to the SMA surface, high dielectric strength for thin layers, was easy to apply in thin layers, was mechanically tough, and had good chemical resistance when cured.

An important design constraint in the heaters required that the ratio of power dissipation in the heaters to power dissipation in the connecting buses was large, i.e. more than 90% of the total heating power was dissipated in the heaters. From this requirement, the total resistance of the heaters had to be approximately 10 times greater than the total resistance of the buses. Since both heaters and buses were fabricated on the same metal layers, the bus resistance could be only varied by changing the width of the buses. The width of the bus was limited by the area of the SMA actuators. Hence the heater and bus patterns had to be carefully planned in order to satisfy this constraint.

The resistance of the layout of the heaters and buses can be calculated from Equation 2.1.

ρ is the resistivity of the material [$\Omega \cdot m^2$], L is the length of the pattern [m], A is the cross section area of the heater trace [m^2], t is the thickness of the pattern [m], W is the width of the pattern [m], R_s is the sheet resistance of the material [Ω/square], and $\frac{L}{W}$ is the aspect ratio of the pattern (number of squares). The 0.100µm thick unannealed sputtered aluminum utilized in the heater/sensor fabrication had a sheet resistance of 2 Ω/square (determined from experiments). The heaters had a long meandering rectangle pattern. Hence the resistances of the heaters can be estimated by dividing the length of the heaters by their width, then multiplying by the sheet resistance.

$$R = \rho \frac{L}{A} = \rho \frac{L}{t \cdot W} = R_s \frac{L}{W}, \quad R_s = \frac{\rho}{t} \tag{2.1}$$

A typical value of the heater resistance is 1000 Ω, enabling 0.08 W to be dissipated in each heater with an applied voltage of only 27 V.

2.1.6 Key Problems in the µF Tip Discovered in the M.S. Thesis

Key problems in the M.S. µF design can be divided into two categories: functionality and design/fabrication. Both categories are equally important and must be addressed in order to advance µF technology. The key problems in functionality are related to the capabilities of the µF tips after they are assembled. The issues in this category are mostly associated with the µF heater/sensor films. The experimental results in the M.S. thesis confirmed that these films provided suitable heating and excellent temperature sensing, resulting the −3dB bandwidth of the closed-loop temperature control at 6.6Hz. The performance of strain sensing and control was not suitable, however. The strain sensors did not have high enough strain sensitivity, and troublesome “looping”, “drifting”, and “non-minimum phase” characteristics were obtained in the control loop dynamics. These issues are briefly reviewed below.

Figure 2.2 illustrates the comparison of $\frac{V_s}{V_h}$ and $\frac{V_t}{V_h}$ plots measured from the first µF prototype with the signal conditioning circuit, described in Chapter 3, between temperature-only (blue color, small temperature change without any strain change) and full scale strain-only (green color, deflection of the μF tip at a constant temperature). The magnitude of the variation in the strain-only data is unacceptably small and cannot provide enough resolution in the strain measurement. Thus, these strain sensors are not suitable to supply position measurements to the closed-loop position control of the μF tip.

Figure 2.2 also indicates the looping problem between the $\frac{V_s}{V_h}$ and $\frac{V_t}{V_h}$ signals from the modified Wheatstone bridge. These loops cause false measurements in the calibrated temperature and strain. Ideally, when the calibrated temperature-only data is plotted on the temperature-strain axes, the plot would vary only in the temperature direction. However, if the temperature-only measurement has loops, there is also an apparent variation in strain that is a false measurement. Similarly, the drifting of successive loops causes incorrect temperature and strain calibration.

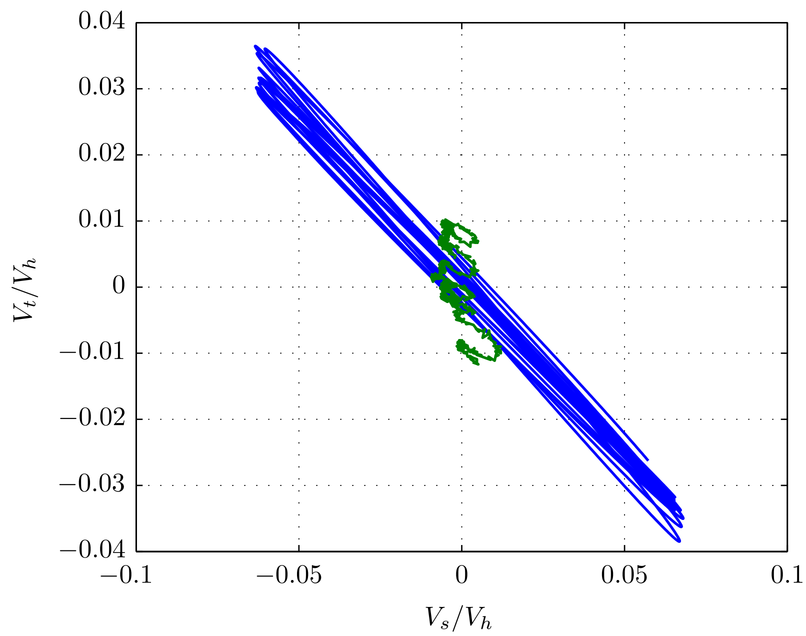

Figure 2.2: $\frac{V_t}{V_h}$ vs. $\frac{V_s}{V_h}$ of temperature only (blue) and strain only (green) data

The non-minimum phase dynamics are a challenge because they limit the control gains, hence the closed loop performance of the control system. The non-minimum phase characteristic results from one or more transfer function zeros in the right-half of the complex plane. Figure 2.3 is the root-locus plot of the closed-loop proportional and integral position feedback control presented in the M.S. thesis. The position control plant of this μF tip is non-minimum phase, with one zero in the right-half plane. The resulting bandwidth of this closed-loop system is low (−3dB bandwidth at 0.6Hz). When the gains are increased, one of system poles is drawn toward the zero in the right-half of the complex plane, eventually causing the closed-loop system to be unstable. Hence, the control gains (and closed loop tracking bandwidth) must be decreased in order maintain stability.

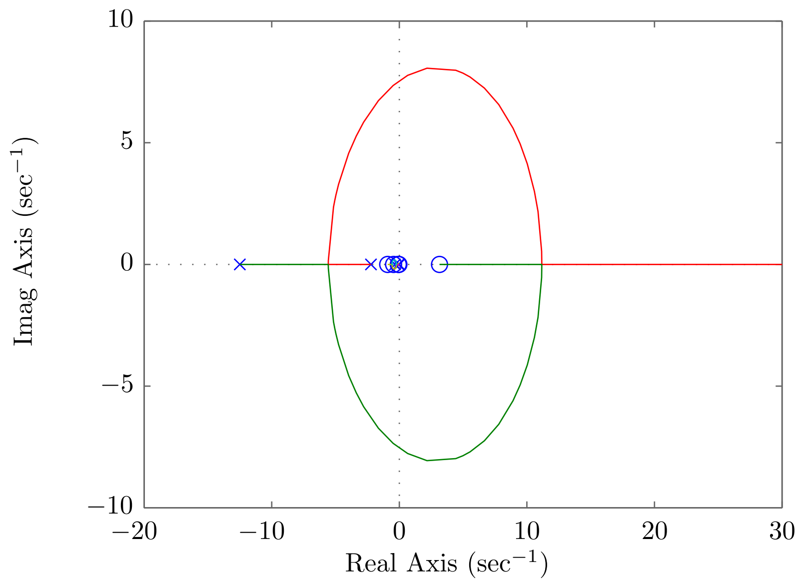

Figure 2.3: Root-locus plot of the PI position feedback control, $KP = -0.055\left[\frac{W}{V}\right]$, and $KI = -0.05\left[\frac{W}{V \times s}\right]$

In addition to the above functional problems, there were three key problems encountered in design and fabrication: poor reliability of the μF films, variability of the soft silicone bonds between the μF films to the SMA actuators, and difficulty providing equal power to each segment. The μF films were unreliable because the thin aluminum sidewalls on via holes between layers tended to become broken when the film was flexed. It would be highly desirable to remove via holes from the SMA actuator design. The soft silicone adhesive layer proved difficult to cure in thin layers. In some areas, this silicone layer remained liquid and could not hold the μF film tight to the SMA surface.

In addition, bonding the μF films to the SMA actuators was a laborious task because the μF films are difficult to align with acceptable errors. Finally, the parallel heater/sensor electrical design in the μF films did not support future expandability because uniform power dissipation requires a gradual reduction in heater resistance from one segment to the next. This is incompatible with the desire to keep bus resistance to a small fraction of total resistance in a many-segment device.

In the next section, the literature in strain sensing technology for micro actuators is reviewed to explore alternative strain sensing methods that may be able to provide higher strain sensitivity, lower false strain, and lower fabrication difficulty than the μF film, yet be compatible with the μF actuator fabrication process.

2.2 Strain Sensing Technology Review

There are three types of strain sensing technology that are commonly used to measure strain in micro actuators. The first type is based on fiber optic Bragg grating sensors. This method determines strain from the wavelength variation of the light reflected in the optical fiber. Strain sensing methods based on this scheme include [James et al., 1996; Melle et al., 1992; Morey et al., 1989; Patrick et al., 1996]. The second type is constructed upon MEMS technology. These sensors measure strain by observing the deformation of 3-D microstructures when they are subjected to strain. e.g., polysilicon beam structures micro strain sensors were utilized in [Lin et al., 1993, 1997; Pan and Hsu, 1999]. The strain measurements were by observing the end of the deformed beams under an optical microscope. These MEMS-based strain sensors were improved in [Que et al., 1999] by adding differential capacitive sensors to provide strain measurements via electrical signals. Both these optical and MEMS based strain sensors are incompatible with the μF catheters because they require separate MEMS or optical structures, which would be difficult to construct on, or attach to the μF actuators.

This brings us back to strain gages. Fundamental theory, fabrication methods, and thin metal film strain gage comparisons were provided in [Witt, 1974]. Extensive studies on thin film meandering strain gages (2mm $\times$ 2mm gage grid size) with sputtered oxide film materials were reported in Al_2O_3, Si_3N_4, HfO_2, SiO_2, were conducted in [Grant et al., 1983]. These strain gages were designed for high temperature strain measurement on compressor blades of turbojet engines. The impact of nickel-chromium alloy ratio (Ni:Cr 40:60, 50:50, and 60:40) in gage films for piezoresistive pressure transducers were studied in [Garcia-Alonso et al., 1993]. Platinum-tungsten strain gages for measuring thrust produced by stationary plasma thrusters on satellites were proposed by [Stephen et al., 2004].

Several research groups also improved these metal film strain sensors by combining temperature sensors in them to form multifunction sensors, which can concurrently measure both strain and temperature. Multifunction sensors with three meandering strain gages patterns arranged in triangular configuration with a circular thermopile at the center were proposed by [Martin et al., 2001; Wrbanek et al., 2001]. These sensors were designed to measure both heat flux and strain in high-pressure propulsion. The gage films and thermopile materials were platinum and Pt13Rh/Pt thermocouples, respectively. Multifunction sensors with flexible thin film sensor arrays were developed by [Lichtenwalner et al., 2007]. There, nickel-chromium alloy and platinum gage films on polyimide were utilized to measured temperature and strain in these sensor arrays.

Unfortunately, all the sensors discussed above are incompatible with the µF actuator because metal oxides are brittle and they cannot survive high bending strain. Sputtered nickel-chromium alloys have high resistance, which can not be utilized as heaters for the µF actuator because of the safe heating voltage limitation. The study in [Lee et al., 2004] indicated that platinum films could be cracked due to thermal expansion mismatch between polyimide and platinum during the high temperature polyimide curing process. Thus, the polyimide had to be cured at a temperature lower than 100C to avoid this thermal stress issue. Curing polyimide at temperatures lower than 100C results in low adhesion, causing the polyimide to de-laminate from the SMA surface. Therefore platinum strain gages were not considered for µF heater/sensor films.

The µF actuator utilizes sputtered, unannealed (amorphous) aluminum as a metal gage film and polyimide as an insulating substrate. In addition to the high tensile strength and low Young's modulus mentioned earlier, sputtered aluminum film also has strong adhesion to polyimide, and it does not crack during the high temperature polyimide curing process. Thus the original sputtered aluminum/polyimide film remains the best choice among all the other materials found for the μF application. Although some design changes will be needed to improve the strain sensitivity and to avoid the dynamics problems found in the closed-loop control with position feedback.

2.3 Research Questions and Objectives in this Dissertation

The studies in [Arata et al., 2005; Dargahi and Najarian, 2004; McCreery et al., 2007; Peirs et al., 2004; Piccin et al., 2009; Song and Guo, 2007; Wagner et al., 2002, 2007] indicated that teleoperation systems with force feedback could improve physicians' abilities in conducting medical procedures. The μF catheter also could utilize teleoperation to control the deflection of its tip, significantly enhancing the functionality and usability of the μF catheter. However, a force sensing capability must be included. As previously discussed in Section 2.1.4, external sensors are not appropriate for the μF tip. Force feedback teleoperation without explicit force sensing was proposed by [Hongan, 1985; Kim, 1992; Ni and Wang, 2004; Sherman et al., 2000; Tavakoli et al., 2005]. This teleoperation system utilized indirect force measurement derived from the position tracking error of its position control loop. This idea could be used with μF catheters provided the position control loop has good performance. Unfortunately the position sensing capability of the μF tip presented in the M.S. thesis was inadequate as discussed above. These limitations lead to the three main research questions in this dissertation, along with specific research objectives discussed below.

Is there a better way to attach the μF film to the SMA actuator? The μF films must be securely and precisely attached on the SMA surface to improve heating and sensing performance, and also prevent them from being broken. However, the μF film in [Aphanuphong, 2008] could not be held flat on the actuator surface because of the non-uniformly cured silicone adhesive layer, and the difficulty of alignment during the bonding step.

There are two paths which can be used to improve the μF film attachment. The first path is to continue to utilize the soft bonding method. With this path, an alternative technique must be explored to uniformly cure the silicone, or the silicone bonding layer must be changed to an alternative soft adhesive which can be uniformly spun-on and cured. The second path is to eliminate the soft bonding layer from the µF actuator design, by building the heater/sensor layers directly on the SMA actuator. This is the objective that will be pursued in this dissertation. Here, the µF film must be redesigned to sense the strain when the neutral bending axis is not located in between the aluminum heater/sensor layers. Since the high SMA strains are no longer isolated from the sensor layers, further experiments must be conducted on the aluminum to understand its strain limits.

What causes the loops between temperature and strain signals in the µF film? There are two sources of looping: non-linearity due to hysteresis between temperature and strain in the SMA, and thermal-dynamic differences between the sensors or phase differences in the signal processing paths.

The objective here is to identify the source of these loops, so they can be avoided by re-design. First, the relationship between $\frac{V_s}{V_h}$ and $\frac{V_t}{V_h}$ must be determined when a small sinusoidal heating power is applied to a flat SMA actuator in order to eliminate the effect of SMA hysteresis. If the relationship between $\frac{V_s}{V_h}$ and $\frac{V_t}{V_h}$ does not have loops, one can conclude that the loops are because of the non-linearity in the SMA. Then, a detailed thermo-mechanical SMA model must be constructed in order to understand and perhaps compensate for these loops. However, if the loops between $\frac{V_s}{V_h}$ and $\frac{V_t}{V_h}$ persist in this experiment, one can conclude that these loops are because of the thermal dynamic mismatches between $\frac{V_s}{V_h}$ and $\frac{V_t}{V_h}$. One possible cause of these mismatches is due to the thermal dynamic differences between the two heater/sensor elements. To verify that these differences are the source of the loops, experiments must be conducted on several heater/sensor designs in order to determine the impact of each design variation. Dynamic models of each heater/sensor design can be constructed based on these experiment results, and then utilized to understand the influences of the thermal dynamic mismatches between heaters on the loops between $\frac{V_s}{V_h}$ and $\frac{V_t}{V_h}$.

What causes the non-minimum phase dynamics? These dynamics must be eliminated (or moved to sufficiently high frequency) in order to obtain the desired closed-loop position control performance.

The objective here is to understand the source of this non-minimum phase behavior. First, a detailed dynamic model must be constructed from measurements of $\frac{V_s}{V_h}$ and $\frac{V_t}{V_h}$ behavior. This will be combined together with the calibration coefficients that produce uncoupled temperature and strain signals. Then this transfer function will be utilized to understand how a zero can be shifted to the right-half of the complex plane. Then this understanding can be applied to the μF film design to avoid the non-minimum phase in the position control plant.

Chapter 3

μF Signal Conditioning Circuit and Calibration Techniques

There are three topics discussed in this chapter. The first topic is the μF signal conditioning circuit design and functionality. This circuit is designed to provide heating current to actuate the μF tip and to detect temperature and strain through voltage changes in the μF film. The second topic is calibration techniques to extract temperature and strain from the voltages measured from the μF film. The third topic is a sinusoidal electro-thermo-mechanical model which is utilized to analyze the source of the phase shift between $\frac{V_s}{V_h}$ and $\frac{V_t}{V_h}$ of each μF film design.

3.1 μF Signal Conditioning Circuit

The μF technology is built upon innovative shape memory alloy (SMA) actuators (μF SMA actuators), which can track both temperature and position commands by varying their temperature through micro heaters (μF films) laminated on their surface. As discussed earlier in Section 2.1.4, these μF films are also capable of sensing temperature and strain changes in the SMA actuators. Therefore, a signal conditioning circuit is needed with abilities to concurrently drive heating current to deflect the μF tip and sense change of voltages on the micro heaters due to thermo-mechanical properties of the μF film. Figure 3.1 is the overall schematic of the μF signal conditioning circuit.

3.1.1 μF Signal Conditioning Circuit Design

The μF signal conditioning circuit can be divided into four functional parts. The first part, in the green dashed box, is the power supply filtering circuit. Two DC power supply voltages,

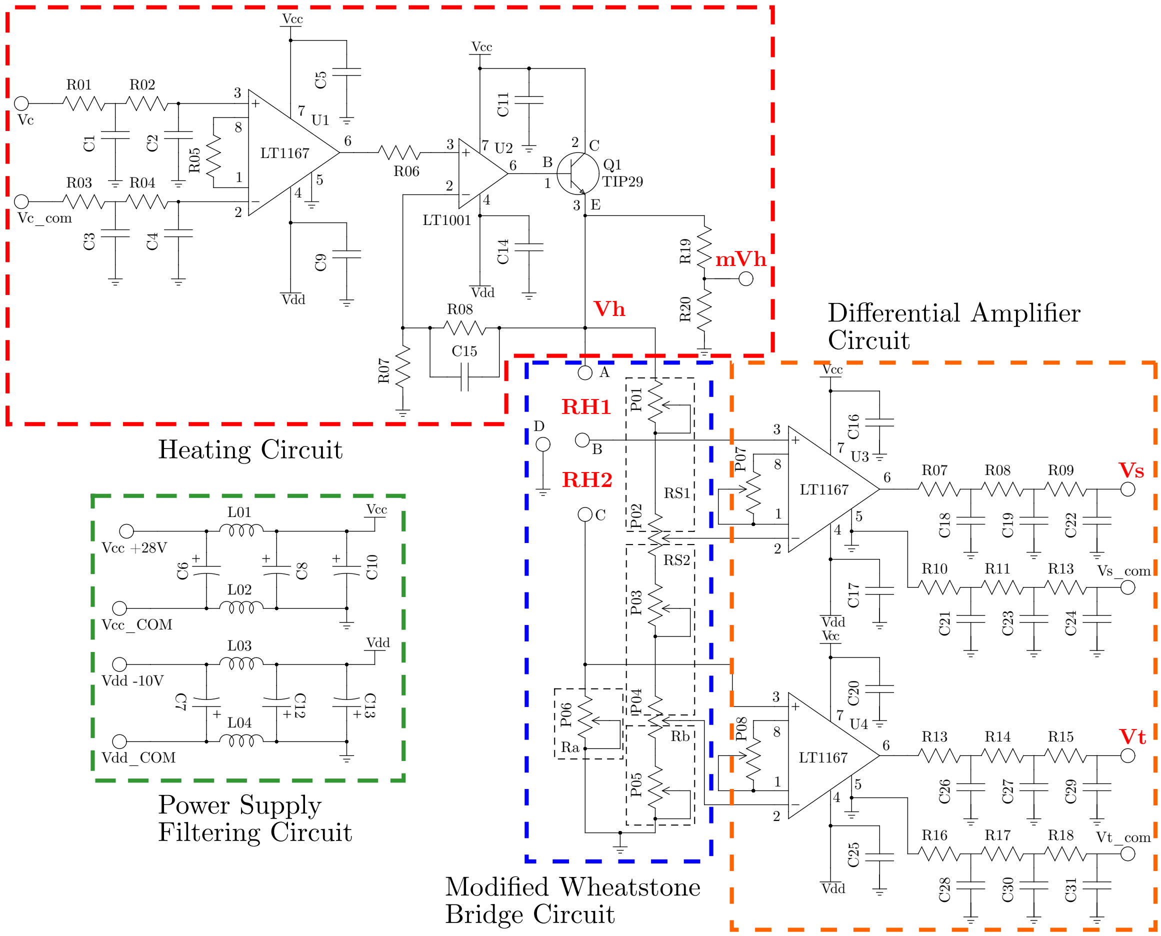

Figure 3.1: µF signal conditioning circuit schematic

+30V (V_{cc}) and -10V (V_{dd}), are filtered through this circuit to ensure that high frequency noise is removed before connecting to other electronic components in the circuit.

The second part, in the red dashed box, is a voltage source heating circuit. This circuit drives a heating voltage (V_h) to the µF film to actuate the SMA actuators. This part of the signal conditioning circuit has two improvements over the circuit used in the author's M.S. thesis. The first improvement is an instrumentation amplifier (U1) at the input from the digital-to-analog converter of the control computer to remove common mode signal noise in the heating voltage command (V_c). The second improvement is the addition of power transistor (Q1) to increase the maximum heating current to drive the modified Wheatstone bridge circuit. The heating voltage (V_h) at terminal A is equal to $V_h = 4.72 \times (V_c - V_{c\_com})$. The maximum V_h of the current configuration is +28V. Due to limited analog-to-digital converter range, the scaled V_h (with the gain of 0.272) is fed back to the control computer via mV_h instead of V_h.

The third part, in the blue dashed box, is a modified Wheatstone bridge circuit, which is used to detect voltage division ratio differences between the μF film and regular resistors. This circuit is composed of two heaters/sensors (RH_1, RH_2), which have the same temperature coefficient of resistance but a different gauge factor, and four regular potentiometers to provide offset adjustments. This circuit is designed to concurrently measure both temperature and strain. This feature will be discussed in detail in Section 3.1.3.

The forth part, in the orange dashed box, is a differential amplifier detection circuit. The signal conditioning circuit maximizes the measurement range of the analog-to-digital converter by utilizing two differential amplifiers (U3: V_s, U4: V_t) with the gains of 17.5 and 18.3 to compare the voltage differences when temperature and strain changes between heater/sensor and regular resistor legs. Both differential amplifier outputs are filtered with 3-stage cascade RC low-pass filter before returning back to the control computer through the analog-to-digital converter. Two differential amplifiers utilized in this part of the circuit are LT1167: single resister gain programmable, precision instrumentation amplifier from Linear Technology. This instrumentation amplifier is typically used as Wheatstone bridge, strain gauge, or thermocouple amplifier.

V_s and V_t signals output from LT1167 amplifiers exhibit unexpected loops because of the phase difference between both signals, when their input impedance are not matched. Figure 3.2 demonstrates this looping problem. The blue color plot is the relationship between $\frac{V_t}{V_h}$ and $\frac{V_s}{V_h}$ signals, when $R_a \approx 0.15 \times RH_1$ is utilized in the modified Wheatstone bridge circuit. The green color plot represents the relationship between $\frac{V_s}{V_h}$ and $\frac{V_t}{V_h}$ of the identical μF actuator as in the blue plot except R_a is equal to RH_1. The green plot does not indicate any loop in it. Therefore, the input impedance of both differential amplifier circuits must be matched in order to avoid this unexpected phase shift issue.

Figure 3.3 shows a photo of the signal conditioning circuit using in this dissertation designed

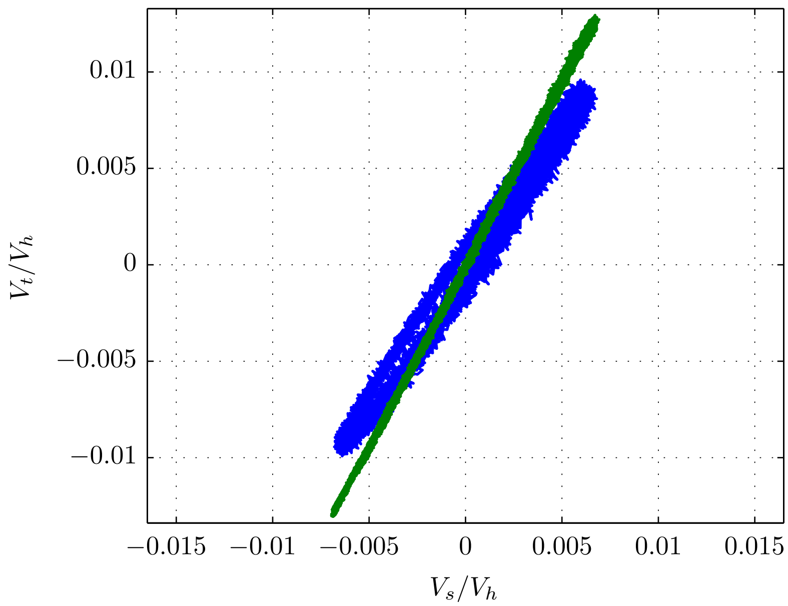

Figure 3.2: Comparison between matched and unmatched input impedance of $\frac{V_s}{V_h}$ and $\frac{V_t}{V_h}$ signals (green: matched input impedance, blue: unmatched input impedance)

by the University of Colorado at Boulder research team and fabricated by Quest Product Development Corporation. This circuit utilized a large ground plane on the backside of the printed circuit board to reduce noise in the circuit. Resistors in the modified Wheatstone bridge circuit and at the gain adjustments are replaced with potentiometers in order to fine tune both offsets and gains to be suitable for the analog-to-digital converter measurement range. The circuit is packed in an aluminum box and all external wires connecting between the circuit and control computer are shielded to reduce noise in the signals.

3.1.2 Voltage Source vs. Current Source in Heating Circuit

One of the contributions in this dissertation is to understand the source of looping due to phase delay between $\frac{V_t}{V_h}$ and $\frac{V_s}{V_h}$. An experiment in Section 3.1.1 suggests that the input impedances between both differential amplifiers are required to be matched in order to eliminate the loop between $\frac{V_t}{V_h}$ and $\frac{V_s}{V_h}$. Figure 3.4 illustrates the voltage source heating circuit of the modified Wheat-

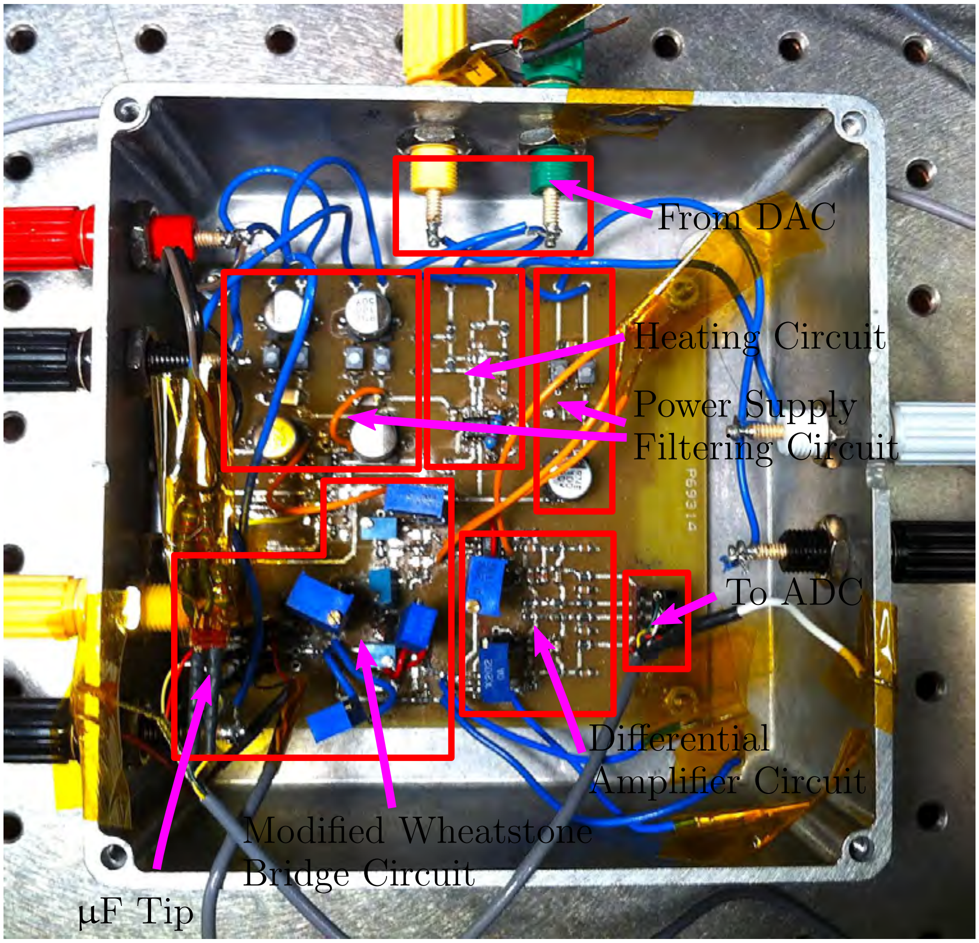

Figure 3.3: Simplified voltage source heating circuit

stone bridge just discussed at the four input terminals of the differential amplifiers (U3, and U4). These circuits can be simplified to Thevenin equivalents as shown in Figure 3.5. Equations 3.1 to 3.4 are V_{th} and Z_{th} of the circuit in Figure 3.4 (A) to (D), respectively. To match input impedances between differential amplifiers, Z_{th} in Equation 3.1 is required to equal to Z_{th} in Equation 3.3, and Z_{th} in Equation 3.2 is required to equal to Z_{th} in Equation 3.4. This matching can be achieved if and only if $R_a = RH_1$, and $R_b = RS_1$.

$$V_{th}(A) = \frac{RH_2 + R_a}{RH_1 + RH_2 + R_a} V_h, \quad Z_{th}(A) = \frac{RH_1 + RH_2 + R_a}{RH_1(RH_2 + R_a)} \tag{3.1}$$

$$V_{th}(B) = \frac{RS_2 + R_b}{RS_1 + RS_2 + R_b} V_h, \quad Z_{th}(B) = \frac{RS_1 + RS_2 + R_b}{RS_1(RS_2 + R_b)} \tag{3.2}$$

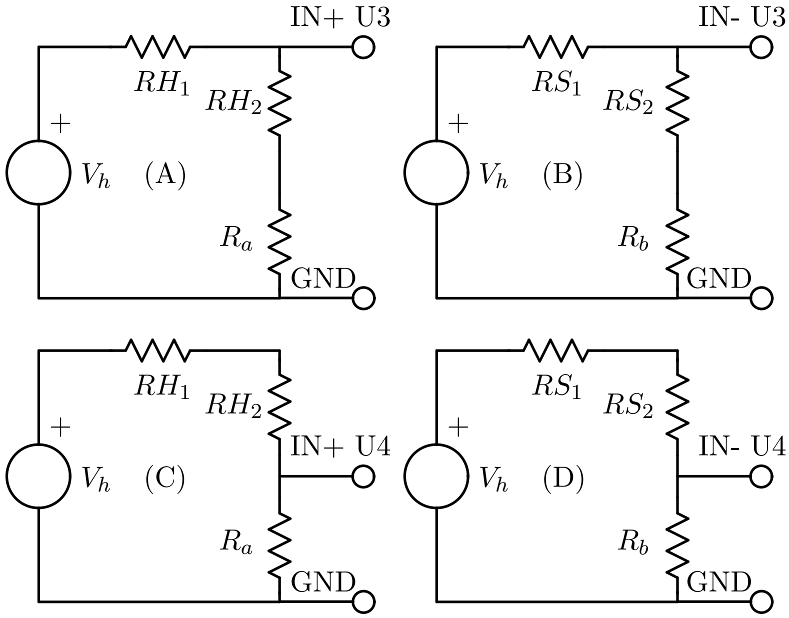

Figure 3.4: Simplified voltage source heating circuit

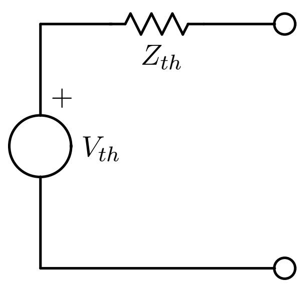

Figure 3.5: Thevenin equivalent circuit

$$V_{th}(C) = \frac{R_a}{RH_1 + RH_2 + R_a} V_h, \quad Z_{th}(C) = \frac{RH_1 + RH_2 + R_a}{R_a(RH_1 + RH_2)} \tag{3.3}$$

$$V_{th}(D) = \frac{R_b}{RS_1 + RS_2 + R_b} V_h, \quad Z_{th}(D) = \frac{RS_1 + RS_2 + R_b}{R_b(RS_1 + RS_2)} \tag{3.4}$$

On the other hand, Figure 3.6 (A) to (D) describe the current source heating circuit. Equations 3.5 to 3.8 are V_{th} and Z_{th} of the corresponding Thevenin equivalent circuits. These equations indicate that input impedances between (A) and (C) and between (B) and (D) cannot be matched unless $RH_1 = RS_1 = 0$. Therefore, current source heating is not suitable for the µF signal conditioning circuit.

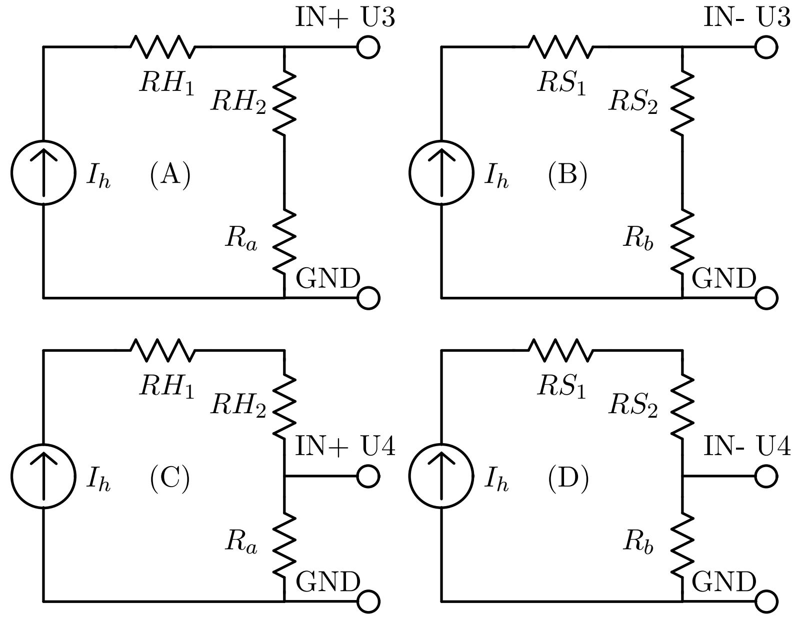

Figure 3.6: Simplified current source heating circuit

$$V_{th}(A) = I_h(RH_1 + RH_2 + R_a), \quad Z_{th}(A) = RH_1 + RH_2 + R_a \tag{3.5}$$

$$V_{th}(B) = I_h(RS_1 + RS_2 + R_b), \quad Z_{th}(B) = RS_1 + RS_2 + R_b \tag{3.6}$$

$$V_{th}(C) = I_h(RH_2 + R_a), \quad Z_{th}(C) = RH_2 + R_a \tag{3.7}$$

$$V_{th}(D) = I_h(RS_2 + R_b), \quad Z_{th}(D) = RS_2 + R_b \tag{3.8}$$

3.1.3 Independent Measurement between Temperature and Strain

An important feature of the signal conditioning circuit is to simultaneously measure the change of voltages when temperature and strain changes. This measurement can be done by utilizing the combination of the heaters/sensors on the µF film and regular resistors in the modified Wheatstone bridge circuit (above) together with differential amplifiers. Figure 3.7 is the simplified schematic of this sensing circuit. RH_1 and RH_2 are heaters/sensors on the µF film. RS_1, RS_2, R_a, and R_b are potentiometers used to adjust offsets of the measurement. G_s and G_t are gains of the differential amplifiers. When heating voltage (V_h) is applied to the circuit, it causes the resistance of RH_1, and RH_2 to vary due to temperature and strain changes as indicated in Equations 3.9, and 3.10. Both Equations 3.9, and 3.10 are called “static Electro-Thermo-Mechanical (ETM) models” of heaters/sensors in μF films. Each of these equations is composed of three elements: the resistance of heaters/sensors at nominal (RH_{10}, RH_{20}), these resistances are measured at room temperature when the μF actuator is at the rest bending state; the resistance change due to temperature change ($\Delta RH|_{\Delta T}$); and the resistance change due to the strain change ($\Delta RH|_{\Delta\epsilon}$). When the temperature on the μF film changes, $\Delta RH|_{\Delta T}$ varies proportional to this temperature by the temperature coefficient of resistance (TCR; ν_1, ν_2). TCR of both heaters/sensors is positive because of the electro-thermal characteristics of the aluminum. In addition, the SMA starts to recover its bending strain ($\Delta\epsilon_1$, $\Delta\epsilon_2$) causing $\Delta RH|_{\Delta\epsilon}$ to vary, when the temperature on the μF film increases. The variation of $\Delta RH|_{\Delta\epsilon}$ is proportional to the effective gauge factors (η_1, η_2). The magnitude of the effective gauge factor is depended on the heater/sensor pattern. The detail of the effective gauge factor is discussed in Section 4.1.

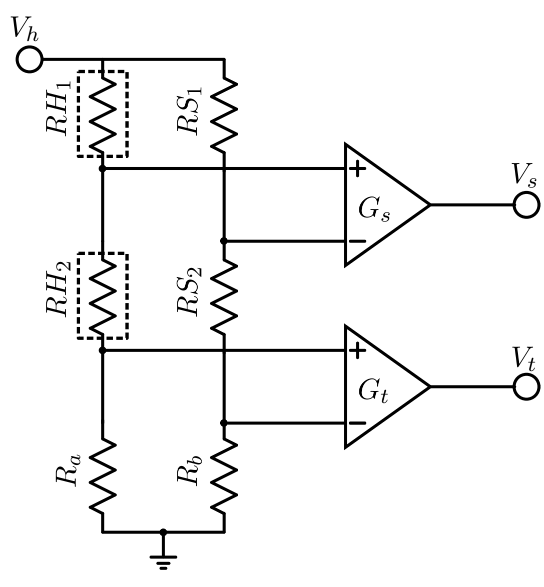

Figure 3.7: The simplified sensing part of the μF signal conditioning circuit

To quantify this effect, let:

RH_{10}, RH_{20} = Nominal resistance values of heaters/sensors at room temperature

ν_1, ν_2 = Temperature coefficients of resistance of RH_1, and RH_2

η_1, η_2 = Effective gauge factors of RH_1, and RH_2 ($\eta = \frac{\Delta R/R}{\Delta \epsilon}$)

ΔT = Change in temperature

$\Delta\epsilon_1$, $\Delta\epsilon_2$ = Change in strain of RH_1, and RH_2

Then the heater resistances are given by

$$\begin{aligned} RH_1 &= RH_{10} + \Delta RH_1|_{\Delta T} + \Delta RH_1|_{\Delta\epsilon} \\ \Delta RH_1|_{\Delta T} &= RH_{10} \cdot \nu_1 \cdot \Delta T \\ \Delta RH_1|_{\Delta\epsilon} &= RH_{10} \cdot \eta_1 \cdot \Delta\epsilon_1 \end{aligned} \tag{3.9}$$

$$\begin{aligned} RH_2 &= RH_{20} + \Delta RH_2|_{\Delta T} + \Delta RH_2|_{\Delta\epsilon} \\ \Delta RH_2|_{\Delta T} &= RH_{20} \cdot \nu_2 \cdot \Delta T \\ \Delta RH_2|_{\Delta\epsilon} &= RH_{20} \cdot \eta_2 \cdot \Delta\epsilon_2 \end{aligned} \tag{3.10}$$

The outputs at V_s and V_t are given by the differences of voltage division ratios:

$$V_s = G_s \left(\frac{RH_2 + R_a}{RH_1 + RH_2 + R_a} - \frac{RS_2 + R_b}{RS_1 + RS_2 + R_b} \right) V_h \tag{3.11}$$

$$V_t = G_t \left(\frac{R_a}{RH_1 + RH_2 + R_a} - \frac{R_b}{RS_1 + RS_2 + R_b} \right) V_h \tag{3.12}$$

Substitute Equations 3.9 and 3.10 in Equations **??** and **??**, then divide V_s and V_t by V_h in order to obtain resistance ratios that are free of V_h.

$$\frac{V_s}{V_h} = G_s \left(\frac{RH_{20}(1 + \nu_2\Delta T + \eta_2\Delta\epsilon_2) + R_a}{RH_{10}(1 + \nu_1\Delta T + \eta_1\Delta\epsilon_1) + RH_{20}(1 + \nu_2\Delta T + \eta_2\Delta\epsilon_2) + R_a} - \frac{RS_2 + R_b}{RS_1 + RS_2 + R_b} \right) \tag{3.13}$$

$$\frac{V_t}{V_h} = G_t \left(\frac{R_a}{RH_{10}(1 + \nu_1\Delta T + \eta_1\Delta\epsilon_1) + RH_{20}(1 + \nu_2\Delta T + \eta_2\Delta\epsilon_2) + R_a} - \frac{R_b}{RS_1 + RS_2 + R_b} \right) \tag{3.14}$$

Linearize Equations 3.13, and 3.14 with respect to ΔT, $\Delta\epsilon_1$, and $\Delta\epsilon_2$ to separate temperature and strain effects:

$$\begin{aligned}\frac{\partial}{\partial(\Delta T,\ \Delta\epsilon_1,\ \Delta\epsilon_2)}\left(\frac{V_s}{V_h}\right) = G_s\Bigg(&\frac{RH_{20}+R_a}{RH_{10}+RH_{20}+R_a} - \frac{RS_2+R_b}{RS_1+RS_2+R_b}\\ &+\frac{(RH_{10}+RH_{20}+R_a)RH_{20}\nu_2-(RH_{20}+R_a)(RH_{10}\nu_1+RH_{20}\nu_2)}{(RH_{10}+RH_{20}+R_a)^2}\Delta T\\ &+\frac{(RH_{10}+RH_{20}+R_a)RH_{20}\eta_2-(RH_{20}+R_a)RH_{20}\eta_2}{(RH_{10}+RH_{20}+R_a)^2}\Delta\epsilon_2\\ &-\frac{(RH_{20}+R_a)RH_{10}\eta_1}{(RH_{10}+RH_{20}+R_a)^2}\Delta\epsilon_1\Bigg)\\ &+H.O.T\ in\ \Delta T,\ \Delta\epsilon_1,\ and\ \Delta\epsilon_2\end{aligned} \tag{3.15}$$

$$\begin{aligned}\frac{\partial}{\partial(\Delta T,\ \Delta\epsilon_1,\ \Delta\epsilon_2)}\left(\frac{V_t}{V_h}\right) = G_t\Bigg(&\frac{R_a}{RH_{10}+RH_{20}+R_a} - \frac{R_b}{RS_1+RS_2+R_b}\\ &-\frac{R_a(RH_{10}\nu_1+RH_{20}\nu_2)}{(RH_{10}+RH_{20}+R_a)^2}\Delta T\\ &-\frac{R_aRH_{20}\eta_2}{(RH_{10}+RH_{20}+R_a)^2}\Delta\epsilon_2-\frac{R_aRH_{10}\eta_1}{(RH_{10}+RH_{20}+R_a)^2}\Delta\epsilon_1\Bigg)\\ &+H.O.T\ in\ \Delta T,\ \Delta\epsilon_1,\ and\ \Delta\epsilon_2\end{aligned} \tag{3.16}$$

Equations 3.17 and 3.18 are the linearized voltage changes in $\frac{V_s}{V_h}$ and $\frac{V_t}{V_h}$ when only the temperature changes.

$$\Delta\frac{V_s}{V_h}\bigg|_{\Delta T} = G_s\frac{(RH_{10}+RH_{20}+R_a)RH_{20}\nu_2-(RH_{20}+R_a)(RH_{10}\nu_1+RH_{20}\nu_2)}{(RH_{10}+RH_{20}+R_a)^2}\Delta T \tag{3.17}$$

$$\Delta\frac{V_t}{V_h}\bigg|_{\Delta T} = -G_t\frac{R_a(RH_{10}\nu_1+RH_{20}\nu_2)}{(RH_{10}+RH_{20}+R_a)^2}\Delta T \tag{3.18}$$

Therefore, the slope between $\frac{V_s}{V_h}$ and $\frac{V_t}{V_h}$, when only the temperature changes can be simplified by dividing Equation 3.18 by Equation 3.17, resulting Equation 3.19.

$$\frac{\Delta\frac{V_t}{V_h}}{\Delta\frac{V_s}{V_h}}\Bigg|_{\Delta T} = -\frac{G_t}{G_s}\frac{R_a(RH_{10}\nu_1+RH_{20}\nu_2)}{RH_{10}RH_{20}(\nu_2-\nu_1)-R_aRH_{10}\nu_1} \tag{3.19}$$

From the current configuration of the μF film, both RH_1 and RH_2 are fabricated on the same aluminum layer, thus both heaters/sensors should have the same temperature coefficients of resistance ($\nu_1 = \nu_2 = \nu$). Therefore Equation 3.19 can be simplified to Equation 3.20.

$$\left.\frac{\Delta \frac{V_t}{V_h}}{\Delta \frac{V_s}{V_h}}\right|_{\Delta T} = \frac{G_t}{G_s}\frac{RH_{10} + RH_{20}}{RH_{10}} \tag{3.20}$$

Equations 3.21 and 3.22 are the linearized voltage changes in $\frac{V_s}{V_h}$ and $\frac{V_t}{V_h}$, respectively when only the strain changes.

$$\left.\Delta \frac{V_s}{V_h}\right|_{\Delta\epsilon} = G_s \frac{RH_{10}RH_{20}\eta_2\Delta\epsilon_2 - (RH_{20} + R_a)RH_{10}\eta_1\Delta\epsilon_1}{(RH_{10} + RH_{20} + R_a)^2} \tag{3.21}$$

$$\left.\Delta \frac{V_t}{V_h}\right|_{\Delta\epsilon} = -G_t \frac{R_a(RH_{10}\eta_1\Delta\epsilon_1 + RH_{20}\eta_2\Delta\epsilon_2)}{(RH_{10} + RH_{20} + R_a)^2} \tag{3.22}$$

Equation 3.23 is the slope between $\frac{V_s}{V_h}$ and $\frac{V_t}{V_h}$, when only the strain changes.

$$\left.\frac{\Delta \frac{V_t}{V_h}}{\Delta \frac{V_s}{V_h}}\right|_{\Delta\epsilon} = -\frac{G_t}{G_s}\frac{R_a(RH_{10}\eta_1\Delta\epsilon_1 + RH_{20}\eta_2\Delta\epsilon_2)}{RH_{10}RH_{20}\eta_2\Delta\epsilon_2 - (RH_{20} + R_a)RH_{10}\eta_1\Delta\epsilon_1} \tag{3.23}$$

Consider the case when the gauge factors $\eta_1 = \eta_2 = \eta$, due to both RH_1 and RH_2 having identical pattern as in the M.S. thesis. The slope between $\frac{V_s}{V_h}$ and $\frac{V_t}{V_h}$ of the strain-only data is linearly independent from the slope of the temperature-only data only when the strain $\Delta\epsilon_1 \neq \Delta\epsilon_2$ as indicated in Equation 3.24. The strain $\Delta\epsilon_1$ can be unequal to $\Delta\epsilon_2$ when RH_1 and RH_2 are located on different metal layers.

$$\left.\frac{\Delta \frac{V_t}{V_h}}{\Delta \frac{V_s}{V_h}}\right|_{\Delta\epsilon} = -\frac{G_t}{G_s}\frac{R_a(RH_{10}\Delta\epsilon_1 + RH_{20}\Delta\epsilon_2)}{RH_{10}RH_{20}(\Delta\epsilon_2 - \Delta\epsilon_1) - R_aRH_{10}\Delta\epsilon_1} \tag{3.24}$$

On the other hand, if the strain $\Delta\epsilon_1 = \Delta\epsilon_2 = \Delta\epsilon$ due to both RH_1 and RH_2 are located on the same metal layer. The slope between $\frac{V_s}{V_h}$ and $\frac{V_t}{V_h}$ of the strain-only data is linearly independent from the slope of the temperature-only data only when the gauge factors $\eta_1 \neq \eta_2$ as indicated in Equation 3.25. The gauge factor η_1 can be unequal to η_2 when both RH_1 and RH_2 are oriented differently.

$$\left.\frac{\Delta \frac{V_t}{V_h}}{\Delta \frac{V_s}{V_h}}\right|_{\Delta\epsilon} = -\frac{G_t}{G_s}\frac{R_a(RH_{10}\eta_1 + RH_{20}\eta_2)}{RH_{10}RH_{20}(\eta_2 - \eta_1) - R_aRH_{10}\eta_1} \tag{3.25}$$

From Equations 3.20, 3.24, and 3.25, one can conclude that as long as $\Delta\epsilon_1 \neq \Delta\epsilon_2$ or $\eta_1 \neq \eta_2$ temperature and strain produce linearly independent changes in $\frac{V_s}{V_h}$ and $\frac{V_t}{V_h}$. Therefore temperature and strain can be uncoupled with calibration techniques discussed in the next section.

3.2 Calibration Techniques

Two types of control methods are used to control the μF tip in this research: closed-loop temperature feedback and closed-loop position feedback. These control techniques require either T, temperature data corresponding to the surface temperature of the μF film, or S, strain data corresponding to μF segment deflection, to feed into the control algorithm. However, the outputs of the signal conditioning circuit discussed in Section 3.1.1 are coupled versions of temperature and strain information. The discussion in Section 3.1.3 indicates that $\frac{V_s}{V_h}$ and $\frac{V_t}{V_h}$ respond differently to temperature and strain. Therefore, this section is dedicated to describe the calibration process shown in the center rectangle box in Figure 3.8. There are two calibration processes studied in this dissertation: orthogonal and non-orthogonal projection. Both methods require slightly different data to construct a calibration matrix but produce significant differences in temperature and strain sensitivity.

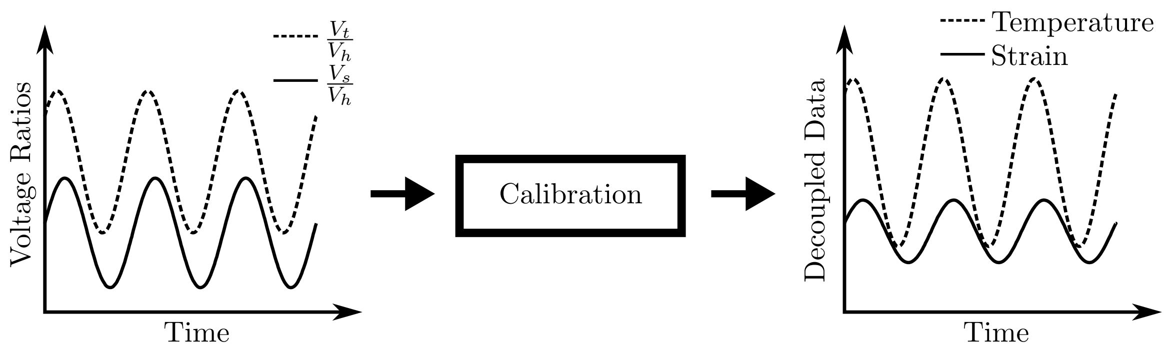

Figure 3.8: Calibration process

3.2.1 Orthogonal Projection Technique

This method was originally utilized to decouple T and S in the Master's thesis [Aphanuphong, 2008]. The process is started with a given low sinusoidal heating power with small amplitude variation to heat the µF film. This small change in temperature does not produce any deflection on the µF tip because it is well below the transition temperature of the SMA. Therefore, the resistance variations on the RH_1 and RH_2 are due to temperature change only. V_s, V_t, and mV_h, (mV_h is the scaled down V_h to be within analog-to-digital converter measurement range, Figure 3.1) measured in this condition, are named "temperature-only data". The actual heating voltage V_h is reproduced from the recorded mV_h. Both measured V_s and V_t are divided by V_h in order to obtain the resistance ratios, which are free of V_h. This $\frac{V_t}{V_h}$ is plotted against $\frac{V_s}{V_h}$ (blue dashed line in Figure 3.9). This plot is called "temperature excursion direction" and the slope of this line is m_t. The "strain excursion direction" (green dashed line in Figure 3.9) is constructed in the direction that is perpendicular to the temperature excursion direction, i.e. with the slope of $-\frac{1}{m_t}$. The red solid line is a typical measurement that has both influences from temperature and strain. The blue and green solid lines are the orthogonal uncoupled temperature and strain of the red solid line.

Equation 3.26 is the relationship from S and T to $\frac{V_s}{V_h}$ and $\frac{V_t}{V_h}$. The matrix M^{-1} in Equation 3.27 is the calibration matrix to uncouple S and T from $\frac{V_s}{V_h}$ and $\frac{V_t}{V_h}$. Offsets and scale factors can be applied to S and T later to match with desired scales for temperature and deflection of the µF tip. Equation 3.28 and 3.29 are the orthogonal temperature and strain calibration.

$$\begin{pmatrix} \frac{V_s}{V_h} \\ \frac{V_t}{V_h} \end{pmatrix} = M \begin{pmatrix} S \\ T \end{pmatrix}, \quad M = \begin{pmatrix} -m_t & 1 \\ 1 & m_t \end{pmatrix} \tag{3.26}$$

$$\begin{pmatrix} S \\ T \end{pmatrix} = M^{-1} \begin{pmatrix} \frac{V_s}{V_h} \\ \frac{V_t}{V_h} \end{pmatrix}, \quad M^{-1} = \frac{1}{\det(M)} \begin{pmatrix} m_t & -1 \\ -1 & -m_t \end{pmatrix} \tag{3.27}$$

$$S = \frac{1}{\det(M)}(m_t \frac{V_s}{V_t} - \frac{V_t}{V_h}) \tag{3.28}$$

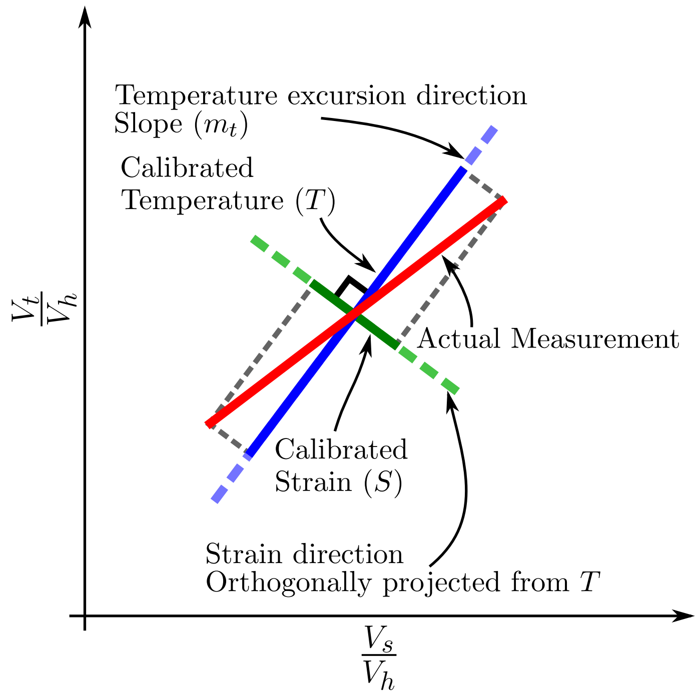

Figure 3.9: Orthogonal projection plot

$$T = \frac{1}{\det(M)}(-\frac{V_s}{V_t} - m_t\frac{V_t}{V_h}) \tag{3.29}$$

The advantage of this calibration method is that it requires only one set of measured data: temperature excursions. This data can be easily measured from the µF tip using the µF signal conditioning circuit. However, the decoupled strain can be small because the direction perpendicular to the temperature excursion direction is not the physical strain direction of the µF tip. Therefore, a new projection method, called non-orthogonal projection, has been investigated to provide stronger strain measurement.

3.2.2 Non-orthogonal Projection Technique

This calibration method can maximize strain measurement by uncoupling the µF film's strain on the actual strain excursion direction. This calibration process is more complex than orthogonal projection technique because it requires both temperature-only and strain-only data. Temperature-only data is measured with the same configuration as described in Section 3.2.1. Strain-only data, which is used to provide strain excursion direction, is not quite as easy to measure because it requires an additional custom fixture. This data needs to be measured at the state when the µF tip is deflected with external forces at a constant temperature. A constant temperature can be achieved when the µF tip is heated at a constant heating power for approximately 3-4 minutes to reach steady state. External forces can be smoothly applied to the µF tip without changing tip's temperature by using a small diameter stiff rod attached to a high precision translational stage. When the translational stage is carefully positioned close to the µF tip, the small rod can be moved slowly, causing the tip to deflect. Thus, the strain on the µF film is varied.

The recorded V_s and V_t in both cases are divided by the recorded V_h to obtain resistance ratios which are free of V_h as discussed in Section 3.1.3. Then the strain-only $\frac{V_t}{V_h}$ is plotted against $\frac{V_s}{V_h}$ in both data sets as shown in Figure 3.10. The blue dashed plot with the slope of m_t is the temperature-only data (as before) and the green dashed plot with the slope of m_s is the strain-only data. The red solid line is a typical measurement from the µF tip that has both temperature and strain influences. The blue and green solid lines are temperature and strain extracted from the red solid line.

A non-orthogonal projection matrix is constructed by first describing the forward relation from S and T to $\frac{V_s}{V_h}$ and $\frac{V_t}{V_h}$ as in Equation 3.30. A non-orthogonal projection matrix is the matrix H^{-1} in Equation 3.31, which computes S and T from $\frac{V_s}{V_h}$ and $\frac{V_t}{V_h}$. Equation 3.32 and 3.33 are implemented in the control algorithm to uncouple temperature and strain in real-time before feeding them into the control loop. As before, both S and T can also be scaled and shifted to match with the desired µF tip temperature and deflection scales.

$$\begin{pmatrix} \frac{V_s}{V_h} \\ \frac{V_t}{V_h} \end{pmatrix} = H \begin{pmatrix} S \\ T \end{pmatrix}, \quad H = \begin{pmatrix} 1 & 1 \\ m_s & m_t \end{pmatrix} \tag{3.30}$$

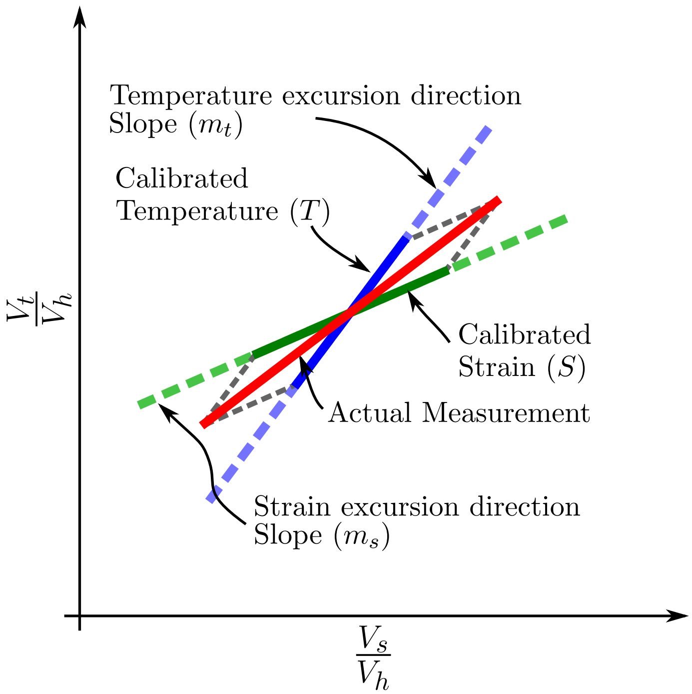

Figure 3.10: Non-orthogonal projection plot

$$\begin{pmatrix} S \\ T \end{pmatrix} = H^{-1} \begin{pmatrix} \frac{V_s}{V_h} \\ \frac{V_t}{V_h} \end{pmatrix}, \quad H^{-1} = \frac{1}{\det(H)} \begin{pmatrix} m_t & -1 \\ -m_s & 1 \end{pmatrix} \tag{3.31}$$

$$S = \frac{1}{\det(H)} \left(m_t \frac{V_s}{V_h} - \frac{V_t}{V_h} \right) \tag{3.32}$$

$$T = \frac{1}{\det(H)} \left(-m_s \frac{V_s}{V_h} + \frac{V_t}{V_h} \right) \tag{3.33}$$

The advantages of this method are that it is able to produce larger strain measurement and also reduce false strain due to temperature because the extracted strain is decoupled on the strain-only direction, which does not have any temperature component in it. On the other hand, this method requires an additional strain-only direction, which needs a custom fixture to deflect the tip in the data acquisition process. Therefore, it is not straightforward to re-calibrate the μF tip after it is used.

3.2.3 Problems in the Calibration Process

As discussed earlier in Chapter 2, the main issue that prevents the position control on the μF tip is due to false strain due to temperature. Figure 3.11 shows an example of the uncoupled temperature and strain plot (the red solid line) of temperature-only data. Ideally, uncoupled temperature-only data would be a vertical line when it is plotted in the Temperature-Strain axes. However, the plot in this example indicates large false strain due to temperature. There are three causes: The first is the phase shift between $\frac{V_t}{V_h}$ and $\frac{V_s}{V_h}$ and this phase shift cannot be removed in the temperature and strain uncoupling process. However, this false strain can be removed by matching input impedances of both V_t and V_h differential amplifiers. The second cause of false strain is due to different time constants in $\frac{V_s}{V_h}$ and $\frac{V_t}{V_h}$. It turns out that these different time constants can be matched only by a special μF film layout, which is discussed in detail in Chapter 4. The third cause of false strain is due to a tilt angle in the uncoupled data. This vertical tilt can occur in the uncoupled data if wrong temperature-only and strain-only data are used to construct the H matrix. Thus, this vertical tilt can be simply removed by recomputing the H^{-1} matrix with correct temperature and strain-only data.

3.3 Sinusoidal Electro-Thermo-Mechanical (ETM) Model

The source of the phase shift between $\frac{V_s}{V_h}$ and $\frac{V_t}{V_h}$ signals cannot be explained by using the static ETM model in Section 3.1.3. Therefore, a sinusoidal ETM model, which includes dynamics of heating power, temperature and strain changes due to the heating power, is constructed in order to utilize to understand the source of this phase shift. The sinusoidal ETM model is modeled based on when a sinusoidal heating power (from a voltage source) is applied to a μF film. The temperature of the μF film rises with the applied heating power at a thermal time constant (τ_t) due to the thermal mass of the μF tip. When the temperature on the μF film varies above the SMA transition temperature, the SMA actuator moves following the temperature with a time constant (τ_m) due to the mass of the μF tip. However, $\tau_m \approx 0$ because the mass of the μF tip is negligible. From these

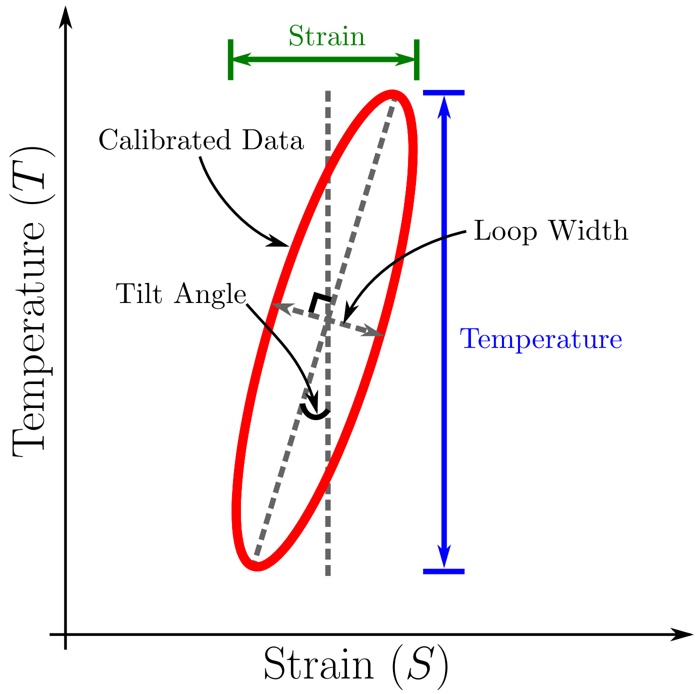

Figure 3.11: Temperature and Strain Loop

considerations, a sinusoidal ETM model of a µF film can be setup as in Equation 3.34. Figure 3.12 indicates temperature (red dashed line) and strain (blue dotted line) changes when a sinusoidal heating power $P = \Delta P \sin(\omega t)$ (black solid line) is applied to a µF film. RH_p, RH_o are nominal resistances of the parallel and orthogonal heaters/sensors respectively. Ω is the phase shift from the applied power to the temperature change due to τ_t. θ is the phase shift from the applied power to the strain change due to $\tau_t + \tau_m$ and $\theta \approx \Omega$. These heater/sensor models are substituted into V_s and V_t models in Equation 3.11, 3.12 and used to analyze heater/sensor designs in Chapter 4. η_p, ν_p, η_o, ν_o are the TCR and effective gauge factor of the parallel and orthogonal heater/sensor designs, respectively. ΔT, $\Delta\epsilon$ are the temperature change from room temperature and the strain change from the strain at room temperature of the µF film.

$$\begin{aligned} RH_1 &= RH_p + RH_p\eta_p\Delta T\sin(\omega t+\Omega) + RH_p\nu_p\Delta\epsilon\sin(\omega t+\theta) \\ RH_2 &= RH_o + RH_o\eta_o\Delta T\sin(\omega t+\Omega) + RH_o\nu_o\Delta\epsilon\sin(\omega t+\theta) \end{aligned} \tag{3.34}$$

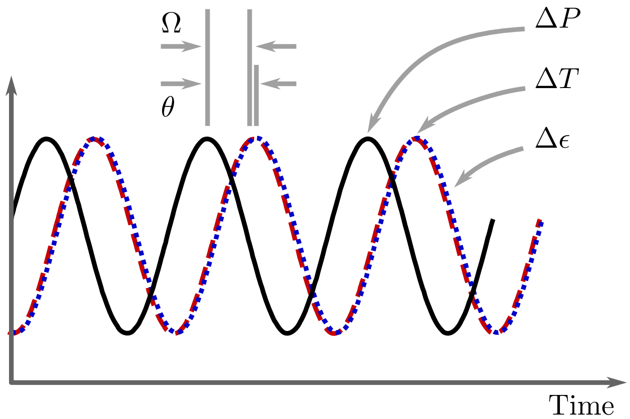

Figure 3.12: Change of temperature and strain when a sinusoidal heating power is applied to a μF film

Signal conditioning circuit, utilized to sense voltage changes due to temperature and strain variations, and temperature and strain decoupling techniques are explored in details in this chapter. These are two key elements of μF systems that enable μF tips to interface with external hardware. Next chapter will be discussed μF embedded heater/sensor designs, and important discoveries and contributions, which entitle μF films to be used to concurrently measure temperature, and strain and provide heat to actuate μF tips.

Chapter 4

μF Film Design and Analysis

The excessive false strain because of temperature and the non-minimum phase position control plant are two key issues obstructing the development of μF catheters. Two possible sources of the excessive false strain are the tilt angle in the calibrated temperature and strain data and the phase shift between $\frac{V_s}{V_h}$ and $\frac{V_t}{V_h}$ from the signal conditioning circuit. This tilt angle can be simply removed by utilizing accurate decoupling coefficients, which are computed from correct temperature-only and strain-only data as discussed in 3.2.3. However, the sources of phase shift between $\frac{V_s}{V_h}$ and $\frac{V_t}{V_h}$ can be due to either the non-linearity between temperature and strain in SMA, or the dynamic differences in $\frac{V_s}{V_h}$ and $\frac{V_t}{V_h}$ in the μF films.

The non-minimum phase dynamics in the position control plant can counteract the closed-loop system from achieving high bandwidth control performance. This high bandwidth position control is required to measure tip's contact force without using explicit force sensors as discussed in Chapter 2. It turns out that the non-minimum phase characteristic in the position control plant is related to the dynamic differences between $\frac{V_s}{V_h}$ and $\frac{V_t}{V_h}$.

These two key issues are investigated in depth in this chapter by studying the impact of heater/sensor patterns in four μF film designs. However before each μF film design can be discussed in details, it is important to understand how μF films measure strain, how heater/sensor patterns affect gauge factors, and how $\frac{V_s}{V_h}$ and $\frac{V_t}{V_h}$ models are constructed from data measured from each μF film design. These models are utilized to analyze and understand characteristics of μF films and develop control algorithms for μF tips. Then four μF film designs using in this dissertation are explored emphasizing in these aspects: heater/sensor configuration, temperature and strain calibration, $\frac{V_s}{V_h}$ and $\frac{V_t}{V_h}$ models, pole-zero analysis of both temperature and position control plant models, the influence of heater/sensor pattern on false measurements utilizing ETM model, and concluding with key problems of the µF film design. Finally, the understanding accumulated from each µF film pattern is utilized to design a µF film with minimum false strain and phase dynamic mismatch. Details of this µF film are presented in the last section of this chapter.

4.1 Strain Measurement and Effective Gauge Factor of µF Films

µF films can be utilized to measure strain when they are combined with signal conditioning circuits discussed in Chapter 3. Both heaters/sensors in the modified Wheatstone bridge circuit must have different resistance changes when they are subjected to identical deformation as discussed in Section 3.1.3. Dissimilar resistance changes can be achieved when both heaters/sensors are subjected to different types of stress e.g. compressive and tensile stresses, or both heaters/sensors have different gauge factors. This dissertation utilizes both methods to measure strain. The first configuration is inherited from the M.S. thesis. It has the neutral bending axis located at the middle between both heaters/sensors. This µF film design consists of two sets of identical heater/sensor patterns fabricated in two separate aluminum layers and this µF film is bonded to an SMA actuator with a soft silicone adhesive to isolate large strain from the SMA actuator bending. When the µF film is bent, one aluminum layer is subjected to tensile strain and the other layer is exposed to compressive strain, which results different heater/sensor resistance changes. The heaters/sensors in both layers are connected together through a via hole located on a pad terminal, forming the center tap of the series connection of heater/sensor pairs in the modified Wheatstone bridge to provide temperature and strain measurements.

The second configuration has the neutral bending axis located at the middle of the SMA thickness because µF films are stiffly laminated on SMA actuators. Therefore both heaters/sensors in µF films are subjected to similar type of strain, e.g. either compressive or tensile strain. This µF film configuration can measure strain because both heaters/sensors have different gauge factors, which can be achieved when heaters/sensors are fabricated with different metals or they have dissimilar patterns. However, different metal for each heater/sensor is not suitable in the μF film because it increases complexity in the fabrication process. μF films with this configuration have two distinct heater/sensor patterns. Heater/sensor traces of the first pattern are parallel to maximum strain direction. Hence, this heater/sensor layout has large resistance change when SMA actuators are bent. On the other hand, traces in the second pattern are oriented orthogonal to the maximum strain. When actuators are bent, this pattern has minimum resistance change.

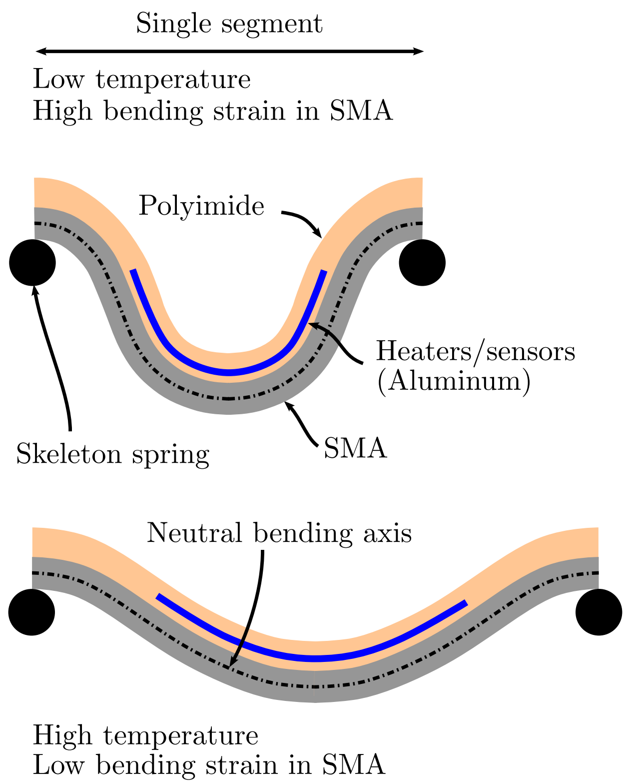

Figure 4.1: Cross-sectional bending profile of a single segment of μF actuator

Figure 4.1 illustrates cross-sectional bending profiles of a single segment (not to scale) μF actuator. The light brown, blue, gray, and black colors are polyimide, aluminum heaters/sensors, SMA, and skeleton spring, respectively. The top diagram is the μF actuator at a low temperature state or a nominal state, which the μF film's temperature is lower than the SMA's transformation temperature. At this state, the SMA is weak (the SMA is partially to fully martensitic), thus the skeleton spring can compress the actuator inward until forces between spring and μF actuator are balanced. The bottom diagram is the μF actuator at high temperature state, which the μF film's temperature is higher than the SMA's transformation temperature (the SMA is partially to fully austenitic). At this state, the SMA is stronger than the skeleton spring, hence, the actuator can recover its strain back to flat trained shape by pushing the spring away.

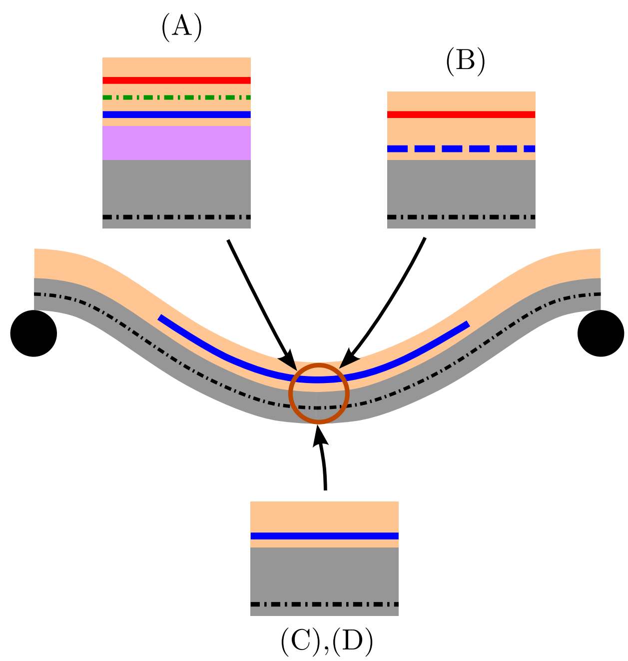

Figure 4.2: Zoom-in of single element cross-sectional profile of μF film designs in Table 4.2

Figure 4.2 presents zoom-in views of the μF film designs when they are subjected to bending. (A) is the profile of two-layer top-bottom symmetric design with a soft silicone adhesive bonding layer, which is indicated in magenta color. When this μF film design is bent, there are two neutral bending axes in this profile because the soft silicone layer prevents the strain of the SMA (gray) from transferring to the μF film (light brown structure). The black color dash-dot line is the neutral bending axis of the SMA located at the middle of the SMA thickness. The green dash-dot line is the neutral bending axis of the μF film located at the middle between top (red) and bottom (blue) aluminum heaters/sensors. Therefore the top aluminum layer is subjected to compressive stress. If the heater/sensor traces have the length, width, and thickness of l, w, and t, respectively. The length of these traces are oriented parallel to the longitudinal axis of the μF actuator strip. This compressive stress (negative stress) causes the length of the heater/sensor traces to be significantly shortened, and the thickness to be increased. The width of these traces, which is on the transverse direction with respect to the actuator strip orientation, is subjected to minimal tensile stress because of the low Poisson's ratio ($0 < \mu << 1$) in the μF film structure. Equation 4.1 indicates that compressive stress reduces resistance of heaters/sensors (ρ is the resistivity of aluminum). Therefore the effective gage factor, (η) indicated in Equations 3.9 and 3.10, of this top aluminum heater/sensor is positive because the negative strain from the compressive stress causes negative resistance change in the heater/sensor.

$$\Delta R = \rho \frac{(l - \Delta l)}{(w + \mu \Delta w)(t + \Delta t)} - \rho \frac{l}{wt}$$
$$\Delta R < 0 \tag{4.1}$$

On the other hand, the bottom aluminum heater/sensor is subjected to tensile stress. This tensile stress (positive stress) increases the length, but decreases the width and the thickness of the heater/sensor traces. Equation 4.2 indicates that tensile stress increases the resistance of the heaters/sensors. Therefore the effective gage factor of this bottom aluminum layer is also positive because the positive strain from the tensile stress causes positive resistance change in the heater/sensor. In addition, effective gage factors of the top and bottom aluminum heaters/sensors are equal because both heaters/sensors have a similar pattern.

$$\Delta R = \rho \frac{(l + \Delta l)}{(w - \mu \Delta w)(t - \Delta t)} - \rho \frac{p}{wt}$$
$$\Delta R > 0 \tag{4.2}$$

The μF films in Figure 4.2 (B), (C), and (D) are stiffly bonded to SMA actuators, thus there is only a neutral bending axis located at the middle of the SMA thickness (black dot-dash line) in each of these designs. Hence, aluminum heaters/sensors in the μF films are subjected to compressive stresses. The detail bending profiles of these films are illustrated in Figure 4.3. In the

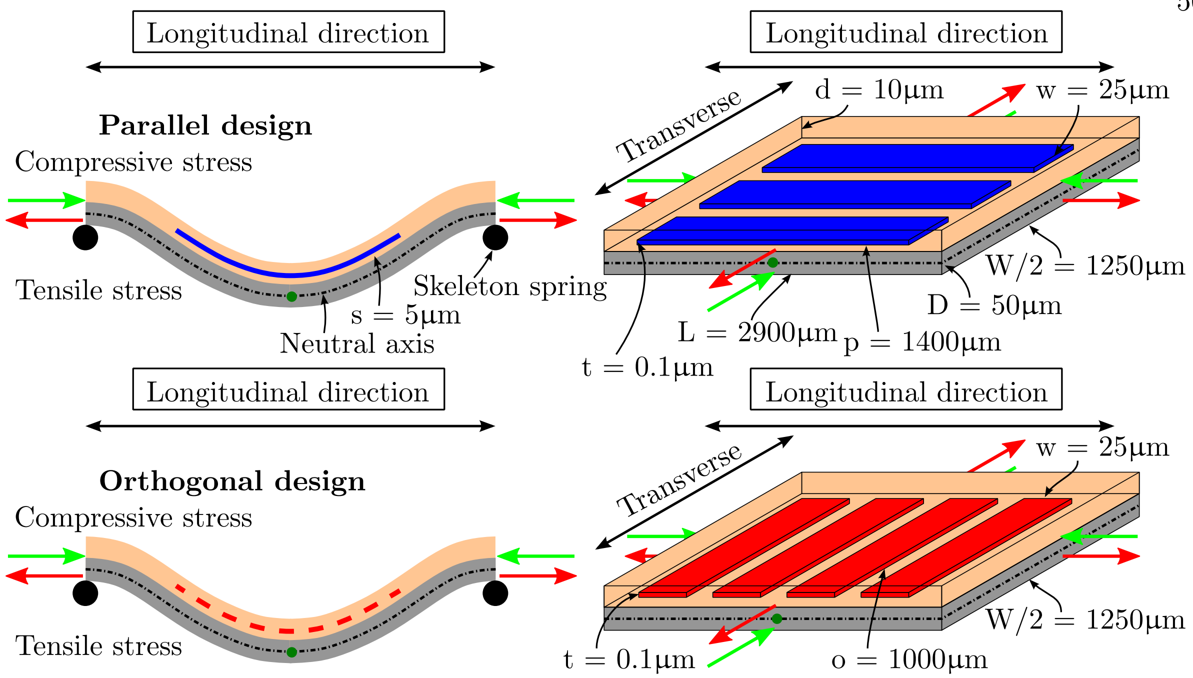

Figure 4.3: Bending profile of single SMA actuator segment with two different heater/sensor orientations when they are compressed between a skeleton spring turn

parallel heater/sensor design, where the length of heater/sensor traces is parallel to the longitudinal axis of the actuator. Since each aluminum trace is thin and has long but narrow bonding area on the polyimide, the magnitude of the shear stress in every trace is diminished to zero at a short distance from both edges of the trace. The remaining stress is axial compressive stress, which shortens the length (p) and thickens the thickness (t) of the heater/sensor traces. The transverse direction of each trace with respect to the actuator is subjected to low axial tensile stress due to the small Poisson's ratio of the µF film structure ($0 < \mu << 1$). Hence, the width (w) of the heater/sensor traces is minimally increased.

$$\Delta R = \rho\frac{(p - \Delta p)}{(w + \mu\Delta w)(t + \Delta t)} - \rho\frac{p}{wt}$$
$$\Delta R < 0 \tag{4.3}$$

Equation 4.3 is the resistance change of the parallel heater/sensor design on a single actuator element, when it is subjected to compressive stress from the actuator bending. p, t, w are the dimensions of the heater/sensor as previously described. This equation indicates that the resistance change on this heater/sensor element is reduced under the bending. All heaters/sensors on actuator segments are connected in series by a bus that is also parallel to the longitudinal axis of the actuator strip. Most areas of the bus are subjected to compressive stress similar to heaters/sensors, except at small areas across the skeleton spring, where the bending changes the direction. However, these areas are small comparing to the total bus area. Hence, the total bus resistance is also reduced. Therefore the total resistance of the parallel heaters/sensors including the bus resistance is reduced, when the parallel heaters/sensors are subjected to compressive stress due to the SMA bending.

The orthogonal heater/sensor design in the bottom row of Figure 4.3, is subjected to the identical bending condition as in the parallel design, but in this design, the width of the heater/sensor traces is subjected to the maximum compressive stress, causing the shortened width (w) and the thickened thickness (t). The length (o) of the heater/sensor traces, on the transverse direction with respect to the actuator strip, is subjected to the tensile stress. However, the heater/sensor traces are long and have large area, therefore the length (o) of the heater/sensor traces does not change. Equation 4.4 is resistance variation of the a single segment orthogonal heater/sensor design, when it is subjected to the same bending condition as in the parallel heater/sensor design. This equation indicates that the resistance change is approximately zero. All heaters/sensors on actuator segments are also connected in series by a bus which is parallel to the longitudinal axis of the actuator. This bus resistance is reduced, when it is subjected to compressive stress due to SMA bending as described earlier in the parallel heater/sensor design. Therefore, the total resistance of this orthogonal heaters/sensors including the bus resistance is reduced, when they are subjected to compressive stress due to the SMA bending.

$$\begin{aligned} \Delta R &= \rho\frac{o}{(w-\Delta w)(t+\Delta t)} - \rho\frac{o}{wt} \\ \Delta R &\approx 0 \end{aligned} \tag{4.4}$$

The resistance of both parallel and orthogonal heaters/sensors are decreased when they are subjected to compressive stress due to the SMA actuator bending. However, when comparing the percentage of the resistance change of both designs with the identical compressive stress, the percentage of the resistance change in the orthogonal heater/sensor design is lower than the parallel heater/sensor design as discussed earlier. Therefore the effective gage factors of both parallel and orthogonal heaters/sensors are positive, but the effective gage factor of the parallel heater/sensor design is greater than the orthogonal heater/sensor design. Hence independent strain measurement can be achieved when both heaters/sensors have different orientation.

4.2 $\frac{V_s}{V_h}$ and $\frac{V_t}{V_h}$ Models Construction

There are two types of closed-loop control implemented on the μF tip prototype: temperature and position control. Both temperature and position cannot be directly measured from the μF films with the signal conditioning circuit, but they can extract from $\frac{V_s}{V_h}$ and $\frac{V_t}{V_h}$ signals as discussed in Section 3.2.1. Therefore, the first task in the control design is to construct the temperature and position control plant models by identifying dynamics relating the change in $\frac{V_s}{V_h}$ and $\frac{V_t}{V_h}$ due to a change in heating power. Typically, a plant model in closed-loop control system is derived from a physical configuration of the actuator, e.g. spring-mass-damper and electro-thermo-mechanical systems, etc. This is difficult for the μF tip because of the non-linearity of the SMA material and the geometry of the μF tip. The ETM model constructed in Section 3.3 also is not possible to use in control design because it describes behavior at only a single frequency. In addition, the temperature and strain in this model are not measured from the μF film.

Therefore, in order to simplify the plant dynamic model construction, both V_s and V_t signals are measured from the μF tip when a step heating voltage (V_h), converted from a step heating power (P_h), is applied to the μF film. Then both V_s and V_t are divided by V_h to form a dataset free of V_h. Both $\frac{V_s}{V_h}$ and $\frac{V_t}{V_h}$ signals are called "empirical data" in the modeling process. Next transfer functions are constructed by selecting denominator and numerator polynomials such that the output of the transfer functions matched the empirical data in the time domain when the identical step heating power is applied. Consider the response of the μF tip when a step heating power is applied to the μF film. The large μF tip's thermal mass (leading to large thermal time constant) acts as a low-pass filter that prevents the tip from instantly jumping to a new position. The μF tip smoothly stretches out until the forces between skeleton spring and SMA actuators are balanced. V_s and V_t signals measured from the μF film also smoothly and monotonically vary following the deflection of the μF tip. They reach steady state when the forces are balanced. When both signals are divided by V_h, the smooth monotonic variation of the ratios is still preserved. One method to match this type of signal is to construct a model from the parallel sum of multiple low-pass filtered signals as shown in the block diagram in Figure 4.4.

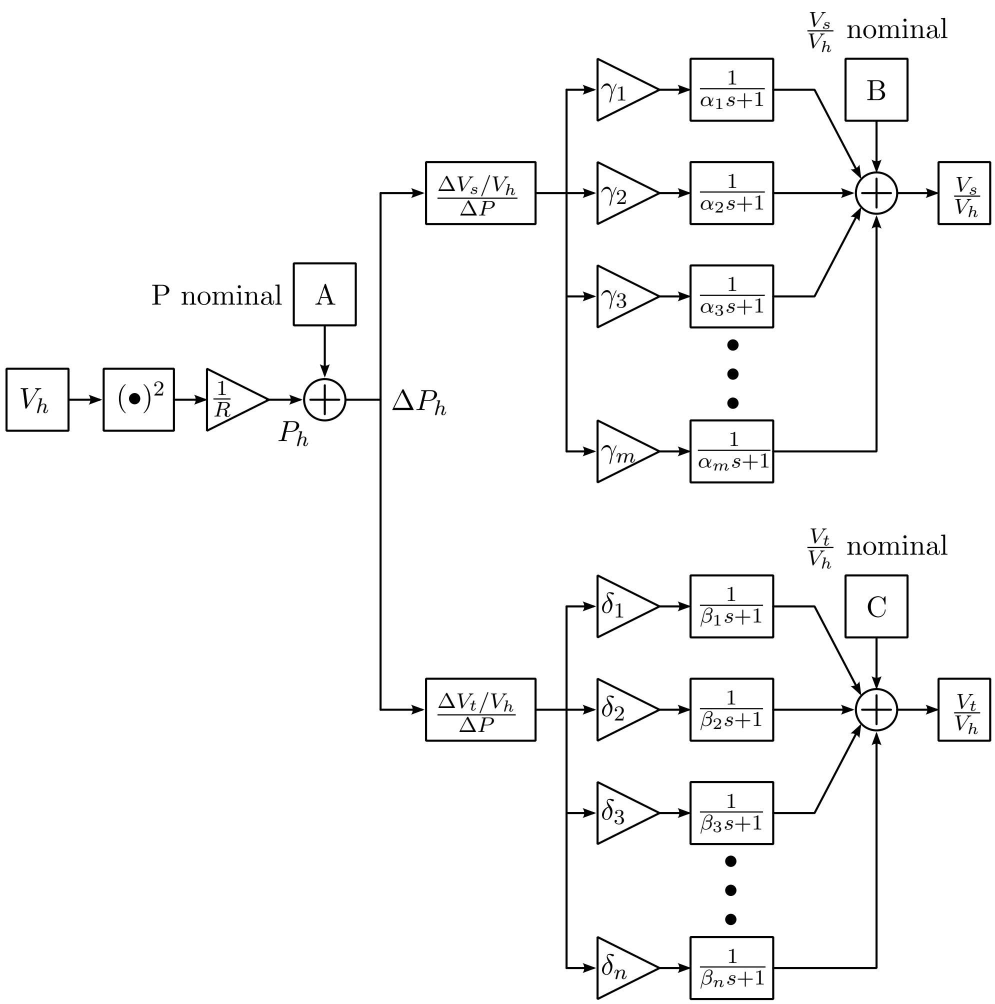

Figure 4.4: The simplified model of $\frac{V_s}{V_h}$ and $\frac{V_t}{V_h}$ used to design closed-loop control system for the μF tip

P_h is the heating power corresponding to the hating voltage V_h. ΔP is the step size of the heating power. $\Delta V_s/V_h$, $\Delta V_t/V_h$ are the changes of $\frac{V_s}{V_h}$ and $\frac{V_t}{V_h}$ at the steady state with given ΔP. $\gamma_1, ...\gamma_m$, and $\alpha_1, ...\alpha_m$ are gains and time constants of each low-pass filter of the $\frac{V_s}{V_h}$ signal. $\delta_1, ...\delta_n$, and $\beta_1, ...\beta_n$ are gains and time constants of each low-pass filter of the $\frac{V_t}{V_h}$ signal. Both $\alpha_1, ...\alpha_m$, and $\delta_1, ...\delta_n$ are constrained to be a partition of unity, which means $\gamma_1 + \ldots + \gamma_m = 1$ and $\delta_1 + \ldots + \delta_n = 1$. A, B, C are constants representing nominal power, nominal $\frac{V_s}{V_h}$, and nominal $\frac{V_t}{V_h}$, respectively. R is the total nominal resistance of both heaters/sensors on the µF film plus R_a from the modified Wheatstone bridge circuit. When a step heating voltage V_h is applied at the input, it is converted to a step heating power. This heating power is scaled to match with the change of $\frac{V_s}{V_h}$ and $\frac{V_t}{V_h}$, multiplied with γ and δ gains, and applied to low-pass filters to adjust their dynamics such that the sum of them is identical with $\frac{V_s}{V_h}$ or $\frac{V_t}{V_h}$ signals.

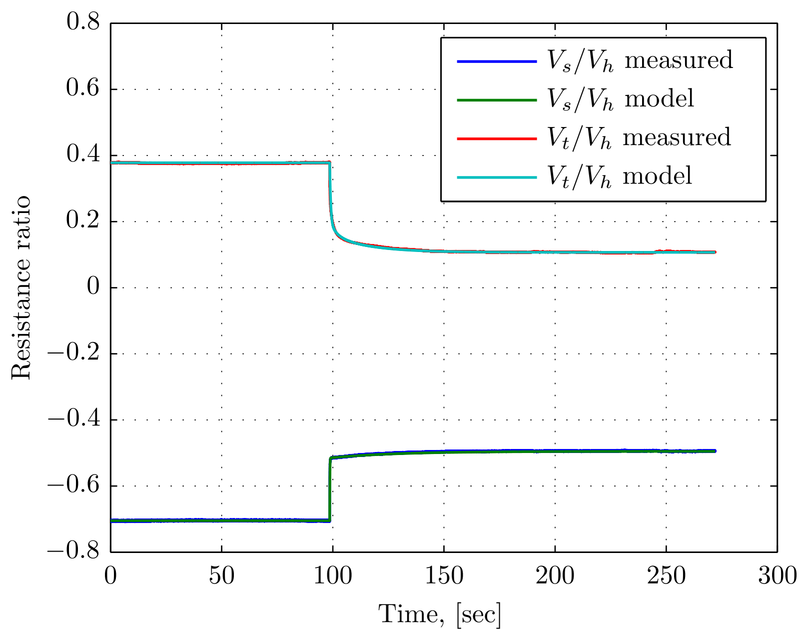

Figure 4.5: Step responses of both measured and simulated $\frac{V_s}{V_h}$ and $\frac{V_t}{V_h}$ from the µF tip prototype utilized in the M.S. thesis

Figure 4.5 is an example of the empirical $\frac{V_s}{V_h}$ and $\frac{V_t}{V_h}$ signals measured from the µF film presented in the M.S thesis and simulated $\frac{V_s}{V_h}$ and $\frac{V_t}{V_h}$. Both $\frac{V_s}{V_h}$ and $\frac{V_t}{V_h}$ signals are simulated from the plant that was constructed by the sum of parallel low-pass filtered signals technique as described above. This model consists of two parallel low-pass filters in the $\frac{V_s}{V_h}$ branch and three parallel low-pass filters in the $\frac{V_t}{V_h}$ branch. The parameters of this model are listed in Table 4.1. Both simulated $\frac{V_s}{V_h}$ and $\frac{V_t}{V_h}$ signals are matched with the empirical data with maximum error less than 5%. This model was utilized for designing both closed-loop temperature and position controls in the M.S. thesis. Both temperature and position tracking simulations were well matched with the temperature and position measured from the µF tip. The details of this discussion can be found in Chapter 4 in [Aphanuphong, 2008]. Hence one can conclude that $\frac{V_s}{V_h}$ and $\frac{V_t}{V_h}$ models constructed from the sum of multiple low-pass filtered signals is suitable to utilize in the µF tip closed-loop proportional and integral control with temperature and position feedback design because it can capture important dynamics of the µF tip required in this type of closed-loop control system. Therefore this modeling method will be utilized to construct $\frac{V_s}{V_h}$ and $\frac{V_t}{V_h}$ signals measured from each µF film design. Then these models will be utilized in close-loop control design of each µF tip in this dissertation.

Table 4.1: Parameters of the two-layer top-bottom symmetric parallel heater/sensor design model

Parameter	Value
A	0.0057 W
B	−0.7050 V/V
C	0.3780 V/V
ΔP	0.0056 W
$\Delta V_s/V_h$	0.2100 V/V
$\Delta V_t/V_h$	−0.2710 V/V
γ_1	0.9048
γ_2	0.0952

Parameter	Value
α_1	0.0800 s
α_2	30.0000 s
δ_1	0.6568
δ_2	0.1476
δ_3	0.1956
β_1	0.4500 s
β_2	3.0000 s
β_3	17.3000 s

4.3 µF Film Design Variations

Table 4.2 is the summary of all four heater/sensor design variations that have been investigated in this dissertation. The first column indicates the name of each design variation. [A] is a two-layer top-bottom symmetric heater/sensor design, which has identical heater/sensor patterns

Table 4.2: Summary of the μF film heater/sensor design variations utilized in this dissertation

μF Flim Design	Schematic μF Film Layout	Modified Wheatstone Bridge Configuration
[A] Two-layer top-bottom symmetric design (soft silicone)	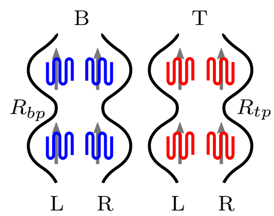	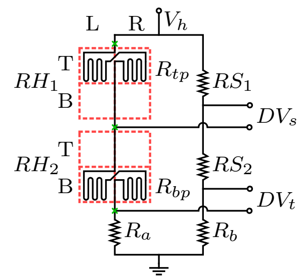
[B] Two-layer top-bottom asymmetric design	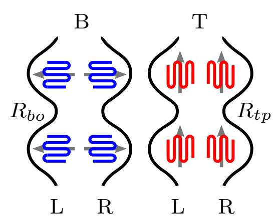	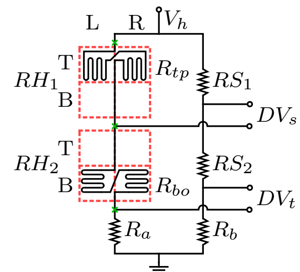
[C] One-layer left-right asymmetric design	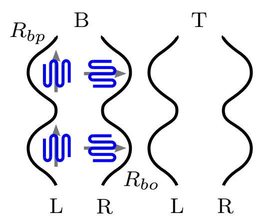	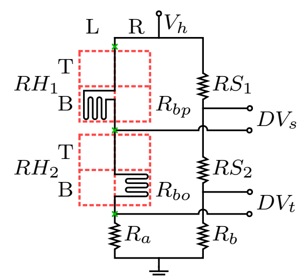
[D] One-layer pairwise left-right symmetric design	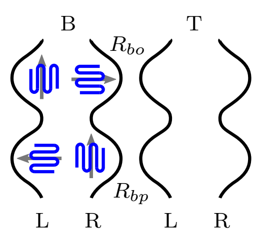	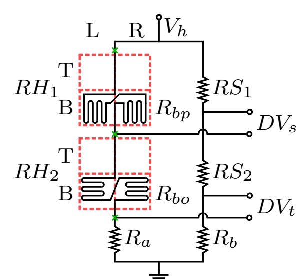

on both top and bottom aluminum layers. [B] is a two-layer top-bottom asymmetric heater/sensor design, which has parallel (with respect to longitudinal axis of the actuator strip) heaters/sensors on the top aluminum layer, and orthogonal heaters/sensors on the bottom aluminum layer. [C] is a one-layer left-right asymmetric heater/sensor design, which has parallel heaters/sensors on the left and orthogonal heaters/sensors on the right sides of an actuator strip. [D] is a one-layer pairwise symmetric pattern, which has both parallel and orthogonal heaters/sensors alternated evenly on the same aluminum layer. The design schematics in the second column show both orthogonal (O) and parallel (P) heater/sensor elements in two SMA actuator segments. However, the buses, which connect these heater/sensor elements in series, are not shown for clarity. The top (T) and bottom (B) aluminum layers are presented in red and blue respectively. The µF film is also divided into left (L) and right (R) sides along the longitudinal axis of the tip. R_{bp} and R_{bo} are the bottom aluminum layer parallel and orthogonal heater/sensor designs, R_{tp} and R_{to} are the top aluminum layer parallel and orthogonal heater/sensor designs, respectively. The third column illustrates how heaters/sensors are connected in the modified Wheatstone bridge circuit. Parallel and orthogonal heaters/sensors are connected at the top (RH_1) and the bottom (RH_2) resistors of the left leg and fixed resisters are utilized in the right leg. The red dashed boxes divides RH_1 and RH_2 into four quadrants to represent the location of the heaters/sensors in the µF film. For example, the top-left and top-right in the top first row indicate that the heater/sensor patterns are located on the top aluminum layer and on the left and right sides along longitudinal orientation of the actuator, respectively. All µF film designs are discussed through out the rest of this chapter.

4.4 [A] Two-Layer Top-Bottom Symmetric Design

This µF film design was created to address two key design and fabrication problems in the design from the M.S. thesis: the reliability of the µF film and the poor adhesion of the soft silicone adhesive in the µF tip construction discussed in Section 2.1.6. Hence this new heater/sensor pattern should not have any via holes on the active segments to lower the chance of broken heaters/sensors. The via holes were relocated to a terminal pad at the proximal stiff segment. Extensive experiments were also conducted on soft silicone adhesive materials to explore an appropriate process to uniformly cure thin soft adhesive bonding layer. Furthermore, the non-orthogonal projection was utilized to uncouple temperature and strain to increase the sensitivity of the strain measurement.

This μF tip prototype consisted of three SMA actuators attached around a super elastic skeleton spring at 120° spacing. SMA actuators were welded on the skeleton spring using welding tabs integrated in the SMA actuator pattern, instead of separated welding bands as utilized in the M.S. thesis. The details of this re-design are discussed in the following subsections.

4.4.1 The μF Film Design [A] Layout

Several heater/sensor layouts were explored in order to remove vias from all active segments or relocate them to the area where strain was minimal. Although, the parallel heater/sensor arrangement, utilized in the M.S. thesis, could not produce suitable heater/sensor layout due to limited actuator area. Therefore, a new heater/sensor topology was investigated, resulting a new heater/sensor arrangement that all heaters/sensors were connected in series. The number of vias in this design could be reduced to only one via per actuator strip and this via was located on a terminal pad on the proximal end of the μF tip where bending strain was low. The series heater/sensor design also had a secondary benefit of reducing the complexity in the design for uniform heating in all actuator segments. This could be achieved with an identical heater/sensor pattern in every actuator segment because equal amount of heating current was applied to all heaters/sensors in the series connection. Compared to the parallel arrangement, as discussed in Section 2.1.6 in [Aphanuphong, 2008], this enables more actuator segments, since the number of squares in the pattern does not have to vary from segment to segment.

Figure 4.6 shows the layout of the series heater/sensor design. This μF film consisted of two aluminum heater/sensor layers (red: top layer, blue: bottom layer). The heater/sensor patterns were constructed from long narrow lines meandering to cover the heating area of each active section. All heaters/sensors on the same aluminum layer were connected in series, then connected to heaters/sensors on the other aluminum layer through via holes (dark green rectangles) on the terminal pad. The welding bands utilized to attach SMA actuators to the skeleton spring were integrated into the actuator pattern at the spacing between actuator strips to reduce complexity of the fabrication and assembly process. The skeleton spring was changed from a steel wire to a super elastic (NiTi) wire to allow SMA actuators to be welded on the skeleton. Non-uniform thickness SMA actuators were utilized in this μF prototype to control the actuator bending shape and to decrease the maximum strain on the SMA (light brown: thick SMA area, dark brown: thin SMA area). The left, middle, and right pads (bright green rectangles) were connected to top, bottom, and center tap of the heaters/sensors respectively. This μF tip still used soft silicone adhesive to bond μF films to SMA actuators. The fabrication process of these μF films and SMA actuators was identical to the process described in Section 2.2 in [Aphanuphong, 2008].

All μF heaters in this design were intact after fabrication, and had expected resistances during on-substrate verification. However, only one μF tip was successfully assembled with acceptable quality because the thin soft silicone adhesive layer was difficult to uniformly cure. Most of the fabrication time was utilized to explore an alternative material and/or a curing method to produce uniform thin soft tacky adhesive layers to bond μF films to μF SMA actuators. None of the silicones investigated could produce a suitable bonding layer. The two-part soft silicone adhesives could not be uniformly cured in thin layers ($\sim$ 25μm). Some one-part silicones could be cured in thin layers but could not be spun-on uniformly on the SMA actuator surface. Tacky Gel from Factor II, as utilized in the M.S. thesis, could be spun on and partially cured at the desired thickness but the adhesion was poor, thus the μF films were either lifting or slipping off the SMA actuators during the μF tip assembly. In addition, the alignment between μF films and SMA actuators was difficult because the alignment marks could not be seen through the silicone adhesive layer. This led to exploration of an alternative method to fabricate the μF actuators without using a silicone adhesive, instead aligning the μF films on the SMA actuators during fabrication. This fabrication method will be discussed in Chapter 5.

4.4.2 Temperature and Strain Calibrations of the μF Film Design [A]

The non-orthogonal projection method was utilized to extract temperature and strain from $\frac{V_s}{V_h}$ and $\frac{V_t}{V_h}$ in the μF tip prototype with the μF film design [A]. The details of this calibration method were described earlier in Section 3.2.2. Figure 4.7 shows the measured $\frac{V_s}{V_h}$ and $\frac{V_t}{V_h}$ in

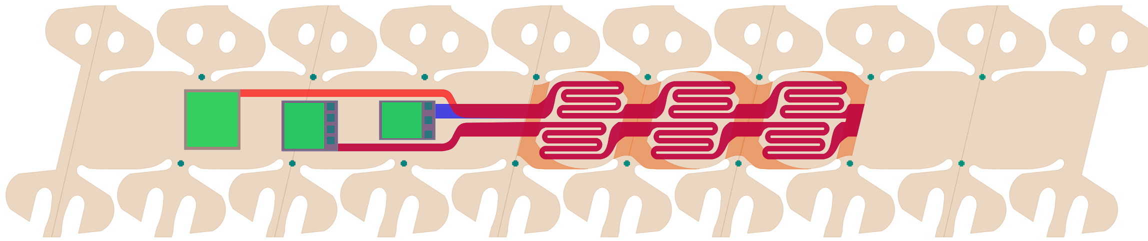

Figure 4.6: three active segments of the µF SMA actuator with two-layer symmetric series heater/sensor layout, the µF film design [A] in Table 4.3

both temperature-only (blue) and strain-only (green) conditions. Equation 4.5 gives the forward transformation matrix (H), where the coefficients of this matrix were extracted from the slopes of the temperature-only and strain-only data from Figure 4.7 (A). H^{-1} provided the non-orthogonal projection coefficients for decoupling temperature and strain. Figure 4.7 (B) shows the corresponding uncoupled temperature and strain of the data. The uncoupled temperature-only signal was perpendicular to the uncoupled strain-only signal, showing that H^{-1} could adequately produce independent temperature and strain.

However the strain measurement indicated in Figure 4.7 (B) was still poor because the size of the full scale strain measurement decoupled from the strain-only measurement (green) was only 20% greater than the false strain (blue). Therefore, this µF film could not be used to measure strain for the closed-loop position feedback control. One possible source of this low strain measurement was because the soft, low adhesion silicone layer allowed the µF film to lift off and slip from the SMA surface instead of conforming itself to bending shape of the SMA actuator. In addition, this bending strain was also proportional to the distance from heaters/sensors to the neutral bending axis. The neutral bending axis of this design was located in the middle of the polyimide separation layer, which was only approximately 0.75µm to the top and bottom aluminum layers. The combination of both problems led to the small strain signal in the µF film design [A].

$$H = \begin{pmatrix} 1.0000 & 1.0000 \\ -0.1914 & -0.8389 \end{pmatrix}, \qquad H^{-1} = \begin{pmatrix} 1.2957 & 1.5444 \\ -0.2957 & -1.5444 \end{pmatrix} \tag{4.5}$$

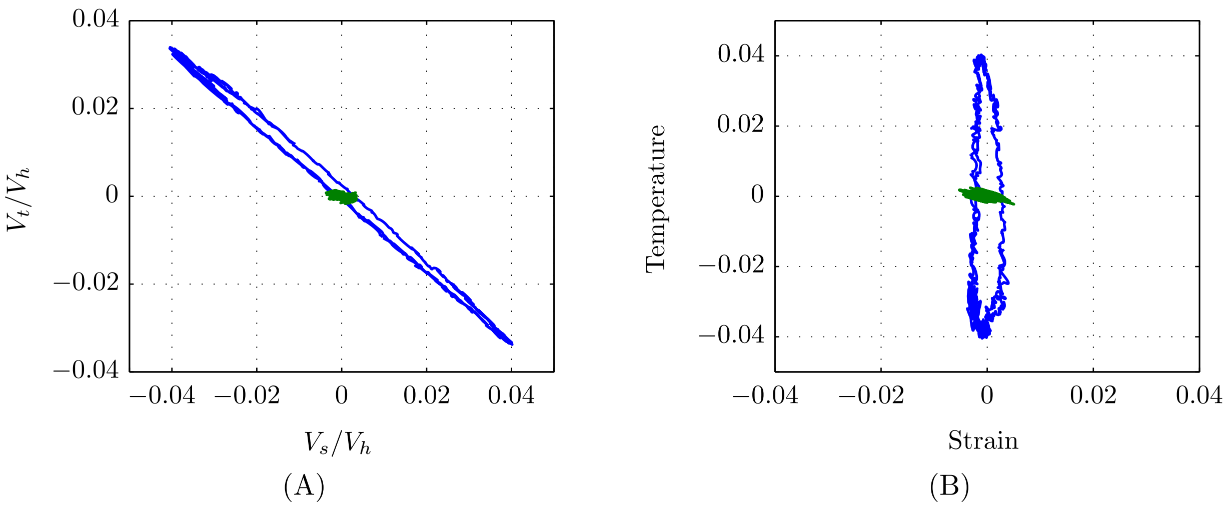

Figure 4.7: Comparison between uncalibrated (A) and calibrated (B) temperature and strain of μF tip with the μF film design [A] (blue: temperature-only measurement, green: strain-only measurement)

4.4.3 $\frac{V_s}{V_h}$ and $\frac{V_t}{V_h}$ Models of the μF Film Design [A]

Figure 4.8 presents both measured and simulated $\frac{V_s}{V_h}$ and $\frac{V_t}{V_h}$ of the μF film design [A]. Both simulated $\frac{V_s}{V_h}$ and $\frac{V_t}{V_h}$ plots are constructed using the technique described in Section 4.2. In this case, the plant model has three parallel low-pass filters in both the $\frac{V_s}{V_h}$ and $\frac{V_t}{V_h}$ branches. The parameters of both branches are provided in Table 4.3. When the $\frac{V_s}{V_h}$ and $\frac{V_t}{V_h}$ plots in Figure 4.8 for the μF film design [A] are compared to the $\frac{V_s}{V_h}$ and $\frac{V_t}{V_h}$ plots of the μF film from the M.S. thesis in Figure 4.5, the dynamics of the μF film design [A] are significantly better matched between $\frac{V_s}{V_h}$ and $\frac{V_t}{V_h}$ since each branch has equal numbers of the parallel low-pass filters, instead of two and three parallel low-pass filters presented in Table 4.1. In addition, the shapes of $\frac{V_s}{V_h}$ and $\frac{V_t}{V_h}$ signals are more similar in the transient region. However, at steady state, $\frac{V_s}{V_h}$ is slowly drifting because of the relaxation of the soft silicone adhesives. The relaxation causes strain to change but not the temperature. Since $\frac{V_s}{V_h}$ is sensitive to both temperature and strain, but $\frac{V_t}{V_h}$ has low sensitivity to strain, the effect of this drifting is present in $\frac{V_s}{V_h}$ but not in $\frac{V_t}{V_h}$.

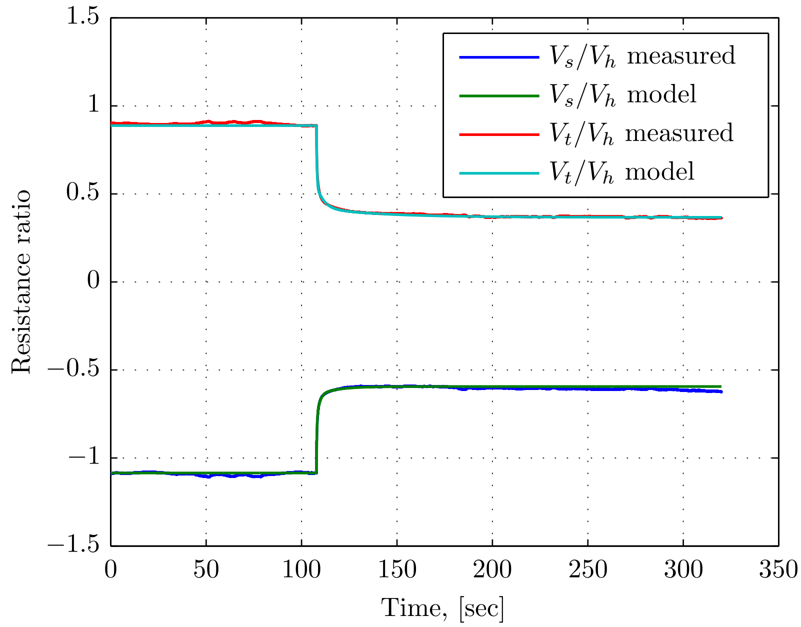

Figure 4.8: Step response of $\frac{V_s}{V_h}$ and $\frac{V_t}{V_h}$ in both empirical and model of the µF film design (A)

4.4.4 Temperature and Position Control Plant Models of the µF Film Design [A]

Figure 4.9 and Table 4.4 show pole and zero plots and lists of the temperature and position control plant parameters, which were constructed using $\frac{V_s}{V_h}$ and $\frac{V_t}{V_h}$ models and the H^{-1} matrix computed previously. Interestingly, both plants were stable and also had minimum phase (all zeros are in the left-half of the complex plane). Dynamically, these plants might be suitable for the closed-loop control system. However, the false strain due to temperature in the temperature-only data shown in Figure 4.7 (B) was large when it was compared to the full scale strain-only data. Therefore, the µF film design [A] could not provide acceptable strain measurement int the µF tip. Hence, closed-loop temperature and position control systems were not implemented on this µF tip prototype.

Table 4.3: Parameters of the dynamic $\frac{V_s}{V_h}$ and $\frac{V_t}{V_h}$ models of the µF film design [A]

Parameter	Value
A	0.0168 W
B	−1.0850 V/V
C	0.8880 V/V
ΔP	0.0145 W
$\Delta V_s/V_h$	0.4910 V/V
$\Delta V_t/V_h$	−0.5210 V/V
γ_1	0.6000
γ_2	0.3000
γ_3	0.1000

Parameter	Value
α_1	0.0800 s
α_2	1.5000 s
α_3	10.0000 s
δ_1	0.6500
δ_2	0.2500
δ_3	0.1000
β_1	0.2500 s
β_2	3.8000 s
β_3	35.0000 s

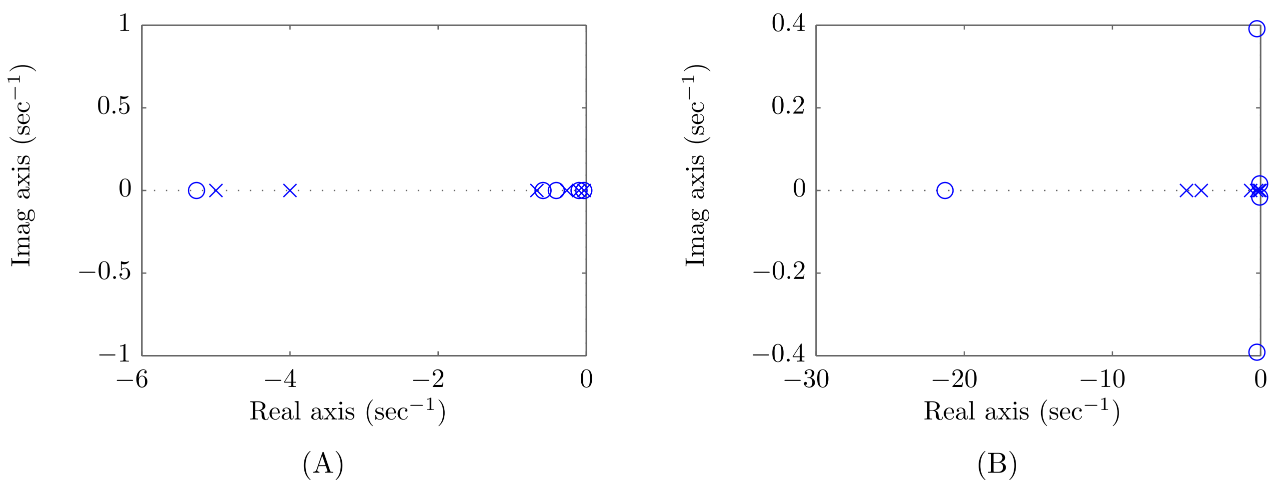

Figure 4.9: Pole and zero plots of the temperature (A) and position (B) control plant models of the µF film design [A]

4.4.5 Summary of Key Difficulties and Solutions

There were several problems newly discovered in the µF film design [A]. Most of them were because of the utilization of a thin soft silicone adhesive layer. Extensive experiments were conducted to explore a proper silicone curing method or an alternative material, but a suitable material or a proper curing technique could not be found as discussed earlier. Therefore, the next µF film design was aimed at exploring an alternative fabrication process without utilizing soft silicone adhesive to bond the µF films to the SMA actuators.

Table 4.4: Poles and zeros of the temperature (A) and position (B) control plant models of the μF film design [A]

(A)

poles	zeros
−5.0000	−5.2620
−4.0000	−0.5830
−0.6667	−0.4043
−0.2632	−0.0979
−0.1000	−0.0324
−0.0286	

(B)

poles	zeros
−5.0000	−21.2979
−4.0000	$-0.2430 \pm 0.3913i$
−0.6667	$-0.0574 \pm 0.0161i$
−0.2632	
−0.1000	
−0.0286	

4.5 [B] Two-Layer Top-Bottom Asymmetric Design

One possible fabrication technique that could eliminate soft silicone adhesives from the μF tip construction was to stiffly bond a μF film on an SMA actuator surface. However additional experiments to determine feasibility of the fabrication process, usability and fatigue of the μF film had to be conducted to ensure that they satisfied the μF tip requirements. An initial experiment was to bond an existing μF film on an SMA sheet utilizing cyanoacrylate. However this method could not produce a uniform bonding between the μF film and the SMA sheet and the μF film also broke off the SMA surface when it was bent because the cyanoacrylate could not conform with the SMA bending. The next experiment was to bond the μF film on an SMA sheet using uncured polyimide. One of the by-products that occurred during the polyimide thermal curing process was water vapor. Most of the liquid could not diffuse out of the thin large polyimide bonding area. It formed micro bubbles in this adhesion layer leading to the nonuniform bond between the μF film and the SMA actuator.

The final experiment was to construct a μF heater film directly on an SMA foil. This fabrication technique could successfully produce an SMA sheet with a uniformly laminated μF heater film on its surface. However, the high bending strain in the SMA actuator might break the aluminum heater/sensor traces, when the film was stiffly bonded to the SMA surface. Several bending experiments were conducted on SMA strips that had simple one-layer heaters/sensors built on their surface. Each strip was bent at small bending radii with the maximum strain of approximately 6%. Then, all heaters were measured their resistance using an ohmmeter. The measurement results indicated that all heaters were intact. Finally, each heater strip was carefully inspected under a high magnification optical microscope to ensure that the heaters did not delaminate from the SMA surfaces. This showed that sufficient adhesion could be obtained to enable a potential of fabricating heaters/sensors directly on SMA surface. An alternative fabrication technique called "co-fabrication" enabled the μF films to be fabricated on the SMA foil and to be utilized as a protection mark for patterning the SMA actuators without employing soft silicone adhesive in the construction process. The details of the co-fabrication method will be discussed in Chapter 5. In addition, these experiments also indicated that the uniform thickness SMA (without thin areas as shown in dark brown color in Figure 4.6) was able to survive the minimum bending radii required on the μF tip prototype.

4.5.1 The μF Film Design [B] Layout

When a μF film was stiffly bonded on an SMA actuator, the neutral bending axis of the μF film was located at approximately the middle of the SMA actuator thickness. The bending strain was proportional to the distance between heaters and the neutral bending axis. Typically, the spacing between the top and bottom metal heater layers in the μF film design was 1.5μm and the SMA actuator thickness was 50μm. Therefore both heater layers were subjected to approximately equal bending strain. As discussed in Section 4.1, independent temperature and strain measurements in stiffly bonded μF films could be achieved when both heaters/sensors in the modified Wheatstone bridge had unequal resistance changes. For example, one heater/sensor had large resistance changes because their traces were oriented parallel to the maximum bending strain direction. the other heater/sensor had small resistance changes when their traces were orthogonal to the maximum bending strain direction. On the other hand, dissimilar resistance changes also could be achieved when both heaters/sensors were constructed with different types of metals. However, to simplify the fabrication process, heaters/sensors of the μF film design [B] were fabricated with the same type of metal.

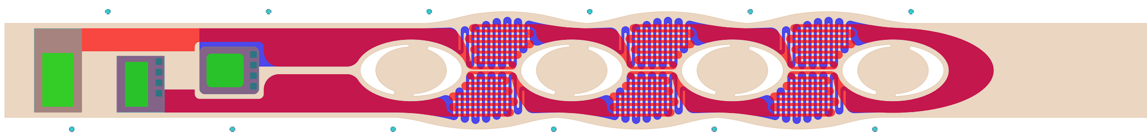

Figure 4.10: Two-layer asymmetric heater/sensor layout (the μF film design [B]) on an SMA actuator with three active segments

Figure 4.10 shows the μF film design [B] enabling independent temperature and strain measurement when it is stiffly bonded on SMA actuators. The μF film design [B] consisted of two aluminum layers. Top (red) and bottom (blue) heaters/sensors were oriented parallel and orthogonal to the longitudinal axis (maximum bending strain direction) of the SMA actuator, respectively. Heater/sensor patterns were constructed from long narrow lines meandering to cover the heating area of each active section as much as possible. The left, middle, and right pads were connected to top, bottom heater/sensor layers and center tap, where top and bottom aluminum heaters/sensors were connected in series, respectively.

The SMA actuator designed for the μF film design [B] had uniform thickness indicated in the consistent light brown color. Welding tabs were relocated to the center of the SMA actuator to reduce the number of welding spots by 50% compared to the SMA actuator of the μF film design [A]. The center welding tabs also behaved as pivots to allow the skeleton spring to twist when it was extended or compressed.

The number of the SMA actuators were reduced from three strips to only one strip per tip to eliminate the cross coupled dynamics and simplify the μF tip configuration. When two SMA actuator strips were removed, a new element called a "spine" was attached on the skeleton spring opposite to the SMA actuator to prevent the μF tip from extending and compressing but allow it to deflect sideways. The spine utilized in this μF tip prototype was a super elastic wire without any welding tab and it was attached to the skeleton spring using epoxy glue.

All heaters/sensors of the μF film design [B] fabricated with co-fabrication process were intact. A new μF tip was successfully constructed using the μF film design [B]. However, the spine was hard to precisely align and glue on the skeleton spring. The spine occasionally detached from the spring after long actuation cycles due to weak epoxy bonds. In the next μF tip prototype, the spine will be redesigned in order to precisely align on the spring and also to strengthen the bonds on the skeleton by welding.

4.5.2 Temperature and Strain Calibrations of the μF Film Design [B]

The non-orthogonal projection is utilized to decouple temperature and strain from $\frac{V_s}{V_h}$ and $\frac{V_t}{V_h}$ signals of the μF film design [B]. Figure 4.11 (A) is a plot of temperature-only (blue) and strain-only (green) data measured from the μF film design [B], and (B) is a plot of uncoupled temperature (blue) and strain (green) of the data presented in (A). Equation 4.6 is the calibration coefficients matrix utilized to decouple temperature and strain from $\frac{V_s}{V_h}$ and $\frac{V_t}{V_h}$ signals. The full range of motion strain measurement of the μF film design [B] is approximately 50% greater than the false strain due to temperature comparing to only 20% in the μF film design [A]. This stiff bonding μF film can reduce the false strain due to silicone relaxation. However, the false strain is still large, thus this μF prototype is not suitable to perform further closed-loop control experiments.

$$H = \begin{pmatrix} 1.0000 & 1.0000 \\ 0.1991 & -1.0017 \end{pmatrix}, \qquad H^{-1} = \begin{pmatrix} 0.8342 & 0.8328 \\ 0.1658 & -0.8328 \end{pmatrix} \tag{4.6}$$

An additional experiment was conducted on the μF film design [B] to ensure that loops between $\frac{V_s}{V_h}$ and $\frac{V_t}{V_h}$ were not because of the hysteresis between temperature and strain in SMA. Small sinusoidal heating voltages, resulting temperature change lower than the SMA transition temperature, were applied to the μF film design [B] on a flat SMA actuator strip. Low sinusoidal heating voltages and a flat SMA strip were utilized to ensure that the variations on both $\frac{V_s}{V_h}$ and $\frac{V_t}{V_h}$ were because of temperature changes but not strain changes. However the relationship between $\frac{V_s}{V_h}$ and $\frac{V_t}{V_h}$ from this experiment still had loops. Hence one could conclude that the source of the loops between $\frac{V_s}{V_h}$ and $\frac{V_t}{V_h}$ was not due to the hysteresis between temperature and strain in the SMA.

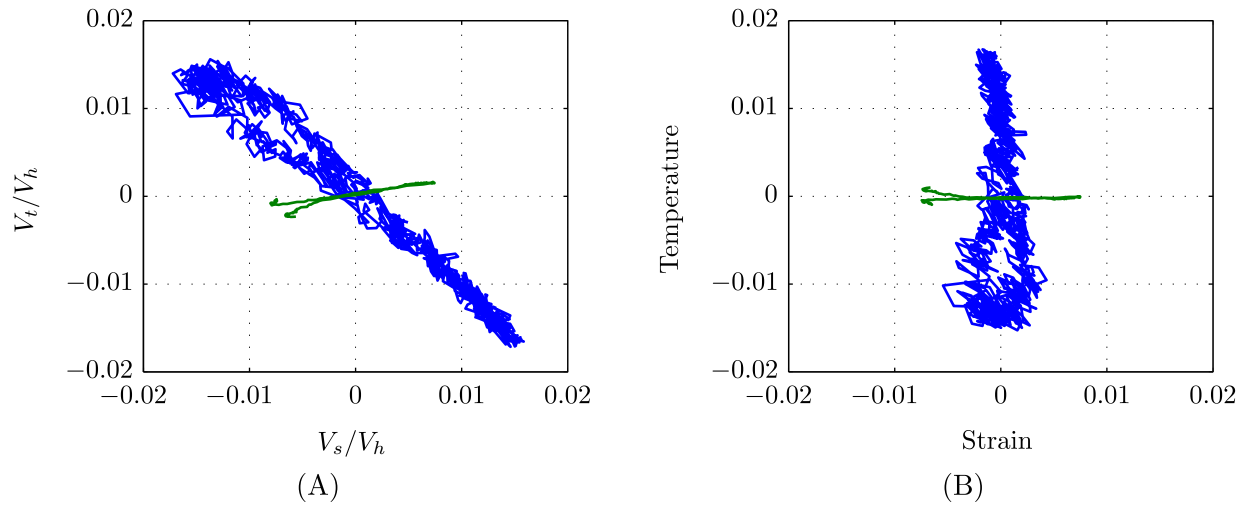

Figure 4.11: Comparison between (A) $\frac{V_s}{V_h}$ and $\frac{V_t}{V_h}$ signals with temperature-only and strain-only conditions measured from the µF film design [B] and (B) decoupled temperature and strain of the signals presented in (A) (blue: temperature-only measurement, green: strain-only measurement)

Subsequent analysis had be conducted to reveal the source of these loops.

4.5.3 $\frac{V_s}{V_h}$ and $\frac{V_t}{V_h}$ Models of the µF Film Design [B]

$\frac{V_s}{V_h}$ and $\frac{V_t}{V_h}$ models of the µF film design [B] are constructed in Simulink utilizing the parallel low-pass filter method in Section 4.2 and then simulated in MATLAB. Figure 4.12 and Table 4.5 present the step response plot of the measured and simulated $\frac{V_s}{V_h}$ and $\frac{V_t}{V_h}$ signals and parameters of both models. Both $\frac{V_s}{V_h}$ and $\frac{V_t}{V_h}$ models have three low-pass filters with remarkably dissimilar filter time constants. For example, $\frac{V_s}{V_h}$ model has the slowest time constant of 80 seconds which is approximately 128% slower than $\frac{V_t}{V_h}$ model. Different filter time constants can lead to dynamic mismatch between $\frac{V_s}{V_h}$ and $\frac{V_t}{V_h}$ signals. The source of this difference is because of thermal dynamic mismatches between the top and bottom aluminum heaters/sensors in the µF film design [B]. The top heater/sensor has the thermal path from the top aluminum layer to a thin polyimide layer and then air. On the other hand, the bottom heater/sensor has the thermal path from the bottom aluminum layer to a thin polyimide layer, to a thick SMA sheet, and then air. The thermal conductivity of the bottom heaters/sensors is greater than the thermal conductivity of the top heaters/sensors because of the thick SMA sheet. This difference leads to thermal time constant mismatches, which can cause the dynamics of the top and bottom heaters/sensors to be different. Surprisingly, it turns out only small dynamic difference between the orthogonal and parallel heaters/sensors can cause large phase differences between $\frac{V_s}{V_h}$ and $\frac{V_t}{V_h}$ signals. Further analysis on the thermal dynamic mismatch will be focused in Section 4.5.5.

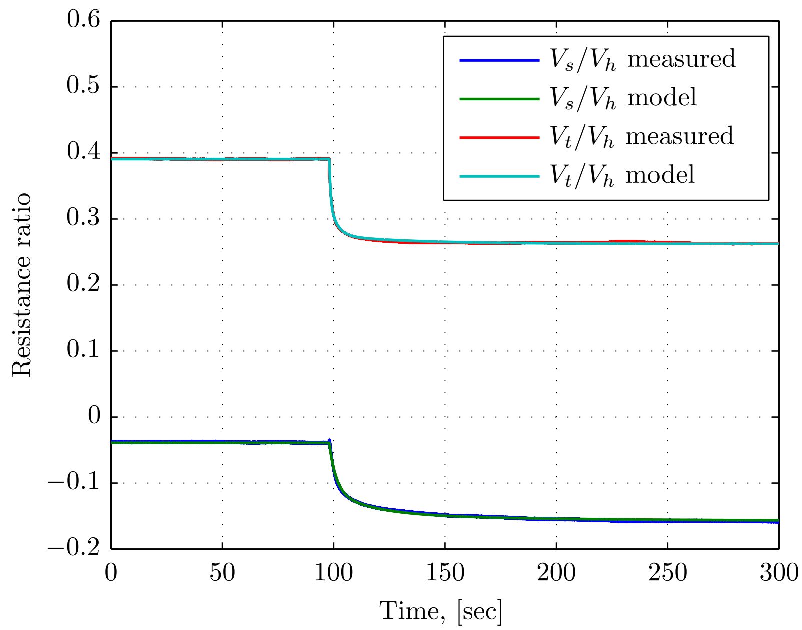

Figure 4.12: Step response of both measured and simulated $\frac{V_s}{V_h}$ and $\frac{V_t}{V_h}$ signals from the μF film design [B]

4.5.4 Temperature and Position Control Plant Models of the μF Film Design [B]

Figure 4.13 (A) and (B) are pole and zero plots of temperature and position control plant models constructed from $\frac{V_s}{V_h}$ and $\frac{V_t}{V_h}$ models in Section 4.5.3 and uncoupling matrix in Equation 4.5. These plots show that both temperature and position control plant models are stable and have minimum phase dynamics. However, the slowest pole of the μF film design [B] is approximately factor of 2 slower than the slowest pole in the μF film design [A] because it is stiffly bonded to a thick SMA, which can rapidly sink the heat from the bottom heater/sensor and dissipates it through

Table 4.5: Parameters of $\frac{V_s}{V_h}$ and $\frac{V_t}{V_h}$ models of the µF film design [B]

Parameter	Value
A	0.0300 W
B	−0.0390 V/V
C	0.3908 V/V
ΔP	0.0050 W
$\Delta V_s/V_h$	−0.1183 V/V
$\Delta V_t/V_h$	−0.1283 V/V
γ_1	0.6000
γ_2	0.3000
γ_3	0.1000

Parameter	Value
α_1	3.0000 s
α_2	17.0000 s
α_3	80.0000 s
δ_1	0.5000
δ_2	0.4000
δ_3	0.1000
β_1	0.6000 s
β_2	3.3000 s
β_3	35.0000 s

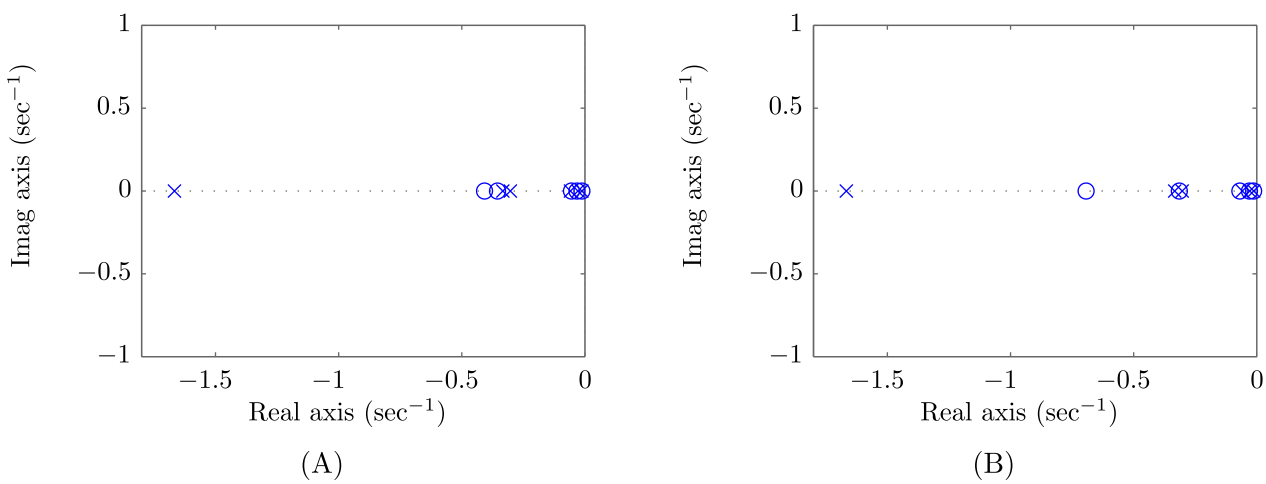

Figure 4.13: Pole and zero plots of the temperature (A) and position (B) control plant models of the µF film design [B]

neighboring elements. Hence the µF film design [B] takes more time to heat the SMA above the transition temperature, which can significantly increase the settling time of the $\frac{V_s}{V_h}$ signal. On the other hand, the µF film design [A] is mechanically and thermally isolated from the SMA with a thick silicone layer. The soft and thick silicone layer can prevent the heat from the µF film design [A] rapidly sinking through the SMA. Therefore, the temperature of the µF film design [A] can reach the steady state with a shorter settling time than the µF film design [B]. Table 4.6 shows poles and zeros of both temperature and position control plant models of the µF film design [B].

Table 4.6: Poles and zeros of the temperature (A) and position (B) control plant models of the µF film design [B] which has two aluminum heater/sensor layers orthogonally oriented to each other

(A)

poles	zeros
−1.6667	−0.4077
−0.3333	−0.3550
−0.3030	−0.0546
−0.0588	−0.0325
−0.0286	−0.0122
−0.0125	

(B)

poles	zeros
−1.6667	−0.6931
−0.3333	−0.3147
−0.3030	−0.0687
−0.0588	−0.0300
−0.0286	−0.0131
−0.0125	

4.5.5 Temperature and Strain Sensing Analyses of the µF Film Design [B]

Subsequent investigations on the source of the phase shift between $\frac{V_s}{V_h}$ and $\frac{V_t}{V_h}$ signals are conducted on a dynamic sinusoidal ETM model of the µF film design [B] using the modeling technique described in Section 3.3. The configuration of the µF film design [B] in the signal conditioning circuit is presented in the third column of Table 4.2. The top layer parallel and bottom layer orthogonal heaters/sensors are connected to the modified Wheatstone bridge at the left leg top (RH_1) and bottom (RH_2) resistors, respectively. As discussed in Section 4.5.3, the thermal paths of the top and bottom heaters/sensors are different causing thermal time constants of both heaters/sensors to be different. These differences are included in the ETM model as the phase shift between applied heating power and temperature changes: Ω_t and Ω_b for the top and bottom heaters/sensors, respectively. In addition, the strain in both heater/sensor layers are slightly different due to unequal distances between heaters/sensors and the neutral bending axis. Equations 4.7, and 4.8 are dynamic ETM models of the parallel (RH_1) and orthogonal (RH_2) heaters/sensors due to an applied sinusoidal heating power $P = \Delta P \sin(\omega t)$. The subscript t, b, p, and o indicate top, bottom aluminum layers, and parallel, orthogonal heater/sensor designs, respectively. ΔT, $\Delta\epsilon$, ν, and η are temperature, strain changes, temperature coefficient of resistance, and gauge factor of heaters/sensors in the µF film. $\Delta R|_{\Delta T}$ and $\Delta R|_{\Delta\epsilon}$ are resistance changes due to temperature and strain variations, respectively.

$$\begin{aligned} RH_1 =& R_{tp} + \Delta R_{tp}|_{\Delta T} + \Delta R_{tp}|_{\Delta \epsilon} \\ \Delta R_{tp}|_{\Delta T} =& R_{tp}\nu_{tp}\left(\Delta T_t \sin(\omega t + \Omega_t)\right) \\ \Delta R_{tp}|_{\Delta \epsilon} =& R_{tp}\eta_{tp}\left(\Delta \epsilon_t \sin(\omega t + \theta_t)\right) \end{aligned} \tag{4.7}$$

$$\begin{aligned} RH_2 =& R_{bo} + \Delta R_{bo}|_{\Delta T} + \Delta R_{bo}|_{\Delta \epsilon} \\ \Delta R_{bo}|_{\Delta T} =& R_{bo}\nu_{bo}\left(\Delta T_b \sin(\omega t + \Omega_b)\right) \\ \Delta R_{bo}|_{\Delta \epsilon} =& R_{bo}\eta_{bo}\left(\Delta \epsilon_b \sin(\omega t + \theta_b)\right) \end{aligned} \tag{4.8}$$

The μF film design [B] is composed of parallel and orthogonal heaters/sensors on the top and bottom aluminum layer, respectively. It is remarkably difficult to perfectly match their resistances since they have dissimilar patterns. Hence, the first design parameter to study is the effect of unequal R_{tp} (top parallel) and R_{bo} (bottom orthogonal) resistances. Second, the parallel and orthogonal heaters/sensors have unequal thermal time constants as discussed in Section 4.5.3. Therefore, the phase shift of temperature change due to applied heating voltage Ω_t of the top layer aluminum can be dissimilar from the phase shift Ω_b of the bottom layer. Third, both aluminum layers are not deposited at the same time, thus both aluminum layers can have slightly different material properties causing ν_{tp} is not equal to ν_{bo}. Forth, parallel and orthogonal heater/sensor layouts have different gauge factors, hence it is important to understand how this difference can improve the strain measurement of the μF film design [B]. The phase differences between $\frac{V_s}{V_h}$ and $\frac{V_t}{V_h}$ based on these four conditions can be invested by utilizing the linearized sinusoidal ETM models. These ETM models can be constructed using the methods below.

Equations 4.9, and 4.10 are the amplified voltage differences V_s and V_t between heater/sensor and fixed resistor legs in the modified Wheatstone bridge circuit. Both V_s and V_t are divided by V_h to decouple them from V_h.

$$\begin{aligned} \frac{V_s}{V_h} =& \frac{RH_2 + R_a}{RH_1 + RH_2 + R_a} - X_s, \quad X_s = \frac{RS_2 + R_b}{RS_1 + RS_2 + R_b} \\ \frac{V_s}{V_h} =& \frac{R_{bo} + \Delta R_{bo}|_{\Delta T} + \Delta R_{bo}|_{\Delta \epsilon} + R_a}{R_{tp} + \Delta R_{tp}|_{\Delta T} + \Delta R_{tp}|_{\Delta \epsilon} + R_{bo} + \Delta R_{bo}|_{\Delta T} + \Delta R_{bo}|_{\Delta \epsilon} + R_a} - X_s \end{aligned} \tag{4.9}$$

$$\begin{aligned}\frac{V_t}{V_h} &= \frac{R_a}{RH_1 + RH_2 + R_a} - X_t, \qquad X_t = \frac{R_b}{RS_1 + RS_2 + R_b} \\ \frac{V_t}{V_h} &= \frac{R_a}{R_{tp} + \Delta R_{tp}|_{\Delta T} + \Delta R_{tp}|_{\Delta\epsilon} + R_{bo} + \Delta R_{bo}|_{\Delta T} + \Delta R_{bo}|_{\Delta\epsilon} + R_a} - X_t\end{aligned} \tag{4.10}$$

Linearize $\frac{V_s}{V_h}$ with respect to $\Delta R_{tp}|_{\Delta T}$, $\Delta R_{tp}|_{\Delta\epsilon}$, $\Delta R_{bo}|_{\Delta T}$, and $\Delta R_{bo}|_{\Delta\epsilon}$ to uncouple temperature and strain effects in $\frac{V_s}{V_h}$.

$$\begin{aligned}\frac{\partial}{\partial(\Delta R)}\left(\frac{V_s}{V_h}\right) &= \frac{R_{bo} + R_a}{R_{tp} + R_{bo} + R_a} - X_s \\ &+ \frac{(R_{tp} + R_{bo} + R_a) - (R_{bo} + R_a)}{(R_{tp} + R_{bo} + R_a)^2} R_{bo}\nu_{bo}(\Delta T_b \sin(\omega t + \Omega_b)) \\ &+ \frac{(R_{tp} + R_{bo} + R_a) - (R_{bo} + R_a)}{(R_{tp} + R_{bo} + R_a)^2} R_{bo}\eta_{bo}(\Delta\epsilon_b \sin(\omega t + \theta_b)) \\ &- \frac{(R_{bo} + R_a)}{(R_{tp} + R_{bo} + R_a)^2} R_{tp}\nu_{tp}(\Delta T_t \sin(\omega t + \Omega_t)) \\ &- \frac{(R_{bo} + R_a)}{(R_{tp} + R_{bo} + R_a)^2} R_{tp}\eta_{tp}(\Delta\epsilon_t \sin(\omega t + \theta_t)) \\ &+ H.O.T\end{aligned} \tag{4.11}$$

$$\begin{aligned}\Delta\frac{V_s}{V_h} &= \frac{\partial}{\partial(\Delta R)}\left(\frac{V_s}{V_h}\right) - \frac{V_s}{V_h}\Big|_{nominal} \\ \frac{V_s}{V_h}\Big|_{nominal} &= \frac{R_{bo} + R_a}{R_{tp} + R_{bo} + R_a} - X_s\end{aligned} \tag{4.12}$$

Equation 4.13 is the linearized $\frac{V_s}{V_h}$ change due to temperature and strain variations

$$\begin{aligned}\Delta\frac{V_s}{V_h} = &\frac{1}{(R_{tp} + R_{bo} + R_a)^2}\Big[R_{tp}R_{bo}\nu_{bo}\Delta T_b \sin(\omega t + \Omega_b) + R_{tp}R_{bo}\eta_{bo}\Delta\epsilon_b \sin(\omega t + \theta_b) \\ &- (R_{bo} + R_a)R_{tp}\nu_{tp}\Delta T_t \sin(\omega t + \Omega_t) - (R_{bo} + R_a)R_{tp}\eta_{tp}\Delta\epsilon_t \sin(\omega t + \theta_t)\Big]\end{aligned} \tag{4.13}$$

$$\begin{aligned}\alpha &= R_{bo}\nu_{bo}\Delta T_b \\ \beta &= R_{bo}\eta_{bo}\Delta\epsilon_b \\ \gamma &= R_{tp}\nu_{tp}\Delta T_t \\ \kappa &= R_{tp}\eta_{tp}\Delta\epsilon_t\end{aligned} \tag{4.14}$$

Simplify Equation 4.13 by substituting with Equation 4.14

$$\begin{aligned}\Delta\frac{V_s}{V_h} =&\frac{1}{(R_{tp}+R_{bo}+R_a)^2}\Big[\\ &(R_{tp}(\alpha\cos(\Omega_b)+\beta\cos(\theta_b))-(R_{bo}+R_a)(\gamma\cos(\Omega_t)+\kappa\cos(\theta_t)))\sin(\omega t)\\ &+(R_{tp}(\alpha\sin(\Omega_b)+\beta\sin(\theta_b))-(R_{bo}+R_a)(\gamma\sin(\Omega_t)+\kappa\sin(\theta_t)))\cos(\omega t)\Big]\end{aligned} \tag{4.15}$$

Rewrite Equation 4.15 in a sinusoidal form

$$\begin{aligned}\Delta\frac{V_s}{V_h} =&\frac{1}{(R_{tp}+R_{bo}+R_a)^2}\Big[\\ &(R_{tp}(\alpha\cos(\Omega_b)+\beta\cos(\theta_b))-(R_{bo}+R_a)(\gamma\cos(\Omega_t)+\kappa\cos(\theta_t)))^2\\ &+(R_{tp}(\alpha\sin(\Omega_l)+\beta\sin(\Omega_r))-(R_{bo}+R_a)(\gamma\sin(\Omega_{tl})+\kappa\sin(\Omega_r)))^2\Big]^{1/2}\\ &\sin\left(\omega t+\angle\Delta\frac{V_s}{V_h}\right)\end{aligned} \tag{4.16}$$

$$\angle\Delta\frac{V_s}{V_h} =\tan^{-1}\left(\frac{R_{tp}(\alpha\sin(\Omega_b)+\beta\sin(\theta_b))-(R_{bo}+R_a)(\gamma\sin(\Omega_t)+\kappa\sin(\theta_t))}{R_{tp}(\alpha\cos(\Omega_b)+\beta\cos(\theta_b))-(R_{bo}+R_a)(\gamma\cos(\Omega_t)+\kappa\cos(\theta_t))}\right) \tag{4.17}$$

Equation 4.16 is the simplified sinusoidal form of the linearized $\Delta\frac{V_s}{V_h}$, which will be used in combination with the linearized $\Delta\frac{V_t}{V_h}$ in Equation 4.22 to investigate the dynamics of the μF film design [B] based on the four conditions discussed earlier. Equation 4.17 is the phase shift of the $\Delta\frac{V_s}{V_h}$ with respect to the applied heating power $P = \Delta P\sin(\omega t)$.

Linearize $\frac{V_t}{V_h}$ with respect to $\Delta R_{tp}|_{\Delta T}$, $\Delta R_{tp}|_{\Delta\epsilon}$, $\Delta R_{bo}|_{\Delta T}$, and $\Delta R_{bo}|_{\Delta\epsilon}$ to separate the temperature and strain effects.

$$\begin{aligned}\frac{\partial}{\partial(\Delta R)}\left(\frac{V_t}{V_h}\right) =&\frac{R_a}{R_{tp}+R_{bo}+R_a}-X_t\\ &-\frac{R_a}{(R_{tp}+R_{bo}+R_a)^2}R_{bo}\nu_{bo}(\Delta T_b\sin(\omega t+\Omega_b))\\ &-\frac{R_a}{(R_{tp}+R_{bo}+R_a)^2}R_{bo}\eta_{bo}(\Delta\epsilon_b\sin(\omega t+\theta_b))\\ &-\frac{R_a}{(R_{tp}+R_{bo}+R_a)^2}R_{tp}\nu_{tp}(\Delta T_t\sin(\omega t+\Omega_t))\\ &-\frac{R_a}{(R_{tp}+R_{bo}+R_a)^2}R_{tp}\eta_{tp}(\Delta\epsilon_t\sin(\omega t+\theta_t))\\ &+H.O.T\end{aligned} \tag{4.18}$$

$$\begin{aligned}\Delta\frac{V_t}{V_h} &= \frac{\partial}{\partial(\Delta R)}\left(\frac{V_t}{V_h}\right) - \frac{V_t}{V_h}\Big|_{nominal} \\ \frac{V_t}{V_h}\Big|_{nominal} &= \frac{R_a}{R_{tp}+R_{bo}+R_a} - X_t\end{aligned} \tag{4.19}$$

Equation 4.20 is the linearized of $\frac{V_t}{V_h}$ variation because of temperature and strain changes

$$\begin{aligned}\Delta\frac{V_t}{V_h} =& \frac{R_a}{(R_{tp}+R_{bo}+R_a)^2}\Big[-R_{bo}\nu_{bo}\Delta T_b\sin(\omega t+\Omega_b) - R_{bo}\eta_{bo}\Delta\epsilon_b\sin(\omega t+\theta_b) \\ & - R_{tp}\nu_{tp}\Delta T_t\sin(\omega t+\Omega_t) - R_{tp}\eta_{tp}\Delta\epsilon_t\sin(\omega t+\theta_t)\Big]\end{aligned} \tag{4.20}$$

Simplify Equation 4.14 by substituting with Equation 4.20

$$\begin{aligned}\Delta\frac{V_t}{V_h} =& \frac{R_a}{(R_{tp}+R_{bo}+R_a)^2}\Big[-(\alpha\cos(\Omega_b)+\beta\cos(\theta_b)+\gamma\cos(\Omega_t)+\kappa\cos(\theta_t))\sin(\omega t) \\ & -(\alpha\sin(\Omega_b)+\beta\sin(\theta_b)+\gamma\sin(\Omega_t)+\kappa\sin(\theta_t))\cos(\omega t)\Big]\end{aligned} \tag{4.21}$$

Rewrite Equation 4.21 in a sinusoidal form

$$\begin{aligned}\Delta\frac{V_t}{V_h} =& \frac{R_a}{(R_{tp}+R_{bo}+R_a)^2}\Big[(\alpha\cos(\Omega_b)+\beta\cos(\theta_b)+\gamma\cos(\Omega_t)+\kappa\cos(\theta_t))^2 \\ & +(\alpha\sin(\Omega_b)+\beta\sin(\theta_b)+\gamma\sin(\Omega_t)+\kappa\sin(\theta_t))^2\Big]^{1/2} \\ & \sin\left(\omega t + \angle\Delta\frac{V_t}{V_h}\right)\end{aligned} \tag{4.22}$$

$$\angle\Delta\frac{V_t}{V_h} = \tan^{-1}\left(\frac{-(\alpha\sin(\Omega_b)+\beta\sin(\theta_b)+\gamma\sin(\Omega_t)+\kappa\sin(\theta_t))}{-(\alpha\cos(\Omega_b)+\beta\cos(\theta_b)+\gamma\cos(\Omega_t)+\kappa\cos(\theta_t))}\right) \tag{4.23}$$

Consider the temperature-only case where $\Delta\epsilon = 0$, Equations 4.17, and 4.23 can be simplified to

$$\angle\Delta\frac{V_s}{V_h}|_{\Delta T} = \tan^{-1}\left(\frac{R_{tp}R_{bo}\nu_{bo}\Delta T_b\sin(\Omega_b) - (R_{bo}+R_a)R_{tp}\nu_{tp}\Delta T_t\sin(\Omega_t)}{R_{tp}R_{bo}\nu_{bo}\Delta T_b\cos(\Omega_b) - (R_{bo}+R_a)R_{tp}\nu_{tp}\Delta T_t\cos(\Omega_t)}\right) \tag{4.24}$$

$$\angle\Delta\frac{V_t}{V_h}|_{\Delta T} = \tan^{-1}\left(\frac{-R_{bo}\nu_{bo}\Delta T_b\sin(\Omega_b) - R_{tp}\nu_{tp}\Delta T_t\sin(\Omega_t)}{-R_{bo}\nu_{bo}\Delta T_b\cos(\Omega_b) - R_{tp}\nu_{tp}\Delta T_t\cos(\Omega_t)}\right) \tag{4.25}$$

The temperature-only relationship between $\Delta\frac{V_s}{V_h}$ and $\Delta\frac{V_t}{V_h}$ (presented in Equations 4.16, and 4.22) has minimum false strain, when $\left|\angle\Delta\frac{V_s}{V_h}|_{\Delta T} - \angle\Delta\frac{V_t}{V_h}|_{\Delta T}\right| = n \times 180°, n = 0, 1, 2, \ldots.$ For example, when the top and bottom heaters/sensors have identical thermal paths, $\Omega_b = \Omega_t = \Omega$, the plot of the temperature-only data between $\Delta\frac{V_s}{V_h}$ and $\Delta\frac{V_t}{V_h}$ has minimum false strain because the angles $\angle\Delta\frac{V_s}{V_h}|_{\Delta T} = \angle\Delta\frac{V_t}{V_h}|_{\Delta T} = \Omega$ (in Equations 4.24, and 4.25), resulting $\left|\angle\Delta\frac{V_s}{V_h}|_{\Delta T} - \angle\Delta\frac{V_t}{V_h}|_{\Delta T}\right| = 0$. However, when $\Omega_t \neq \Omega_b$, it is not obvious how each parameter can affect the magnitude of the false strain. Therefore a simulation model is constructed from Equations 4.16 and 4.22, then utilize it to analyze the influence of each parameter based on four physical conditions of the µF film design [B] discussed earlier.

Figure 4.14 (A) presents a simulation result of the relationship between $\Delta\frac{V_s}{V_h}$ and $\Delta\frac{V_t}{V_h}$ of the temperature-only data ($\Delta\epsilon_t = \Delta\epsilon_b = 0$) in dashed lines and strain-only data ($\Delta T_t = \Delta T_b = 0$) in solid lines, when $\frac{\nu_{bo}}{\nu_{tp}} = 1$, $\frac{\eta_{bo}}{\eta_{tp}} = 0.30$, $R_a = R_{tp}$, and $\frac{R_{bo}}{R_{tp}}$ is varied from 0.8 to 1.2. This plot indicates that the ratio between the parallel and orthogonal heaters/sensors ($\frac{R_{bo}}{R_{tp}}$) can cause variation in the slope of temperature-only and strain-only data plots, causing different temperature and strain decoupling coefficients for each pair of R_{tp} and R_{bo}. Figure 4.14 (B) is a normalized false strain magnitude extracted from the temperature-only data with respect to the magnitude of the full scale strain plot when $\Omega_t - \Omega_b$ is varied from $-3°$ to $3°$ and $\frac{R_{bo}}{R_{tp}}$ is varied from 0.8 to 1.2. This simulation result indicates that only minor offset between Ω_t and Ω_b can cause large false strain. However, $\frac{R_{bo}}{R_{tp}} \neq 1$ does not change the size of the false strain because the blue, green, and red plots are located on top each other.

Figure 4.15 (A) shows the relationship between simulated $\Delta\frac{V_s}{V_h}$ and $\Delta\frac{V_t}{V_h}$ of the temperature-only and strain-only data, when $\frac{R_{bo}}{R_{tp}} = 1.0$, $R_a = R_{tp}$, $\frac{\eta_{bo}}{\eta_{tp}} = 0.30$, and $\frac{\nu_{bo}}{\nu_{tp}}$ is varied from 0.8 to 1.2. The variation of $\frac{\nu_{bo}}{\nu_{tp}}$ causes slope of the temperature-only plot to vary but does not change slope of the strain-only plot, leading to the different temperature and strain uncoupling coefficients for each pair of ν. When the ratio $\frac{\nu_{bo}}{\nu_{tp}}$ increases, the temperature-only data is more independent from the strain-only data, which can be observed from the increasing angle between the lines. Figure 4.15 (B) is the normalized false strain of the temperature-only data with respect to the full scale strain when Ω_t is not equal to Ω_b. The size of the false strain is proportional to the phase difference between Ω_t and Ω_b. However the ratio between $\frac{\nu_{bo}}{\nu_{tp}}$ has only small effect on the false strain.

Figure 4.16 (A) presents the simulated temperature-only and strain-only data of the µF film

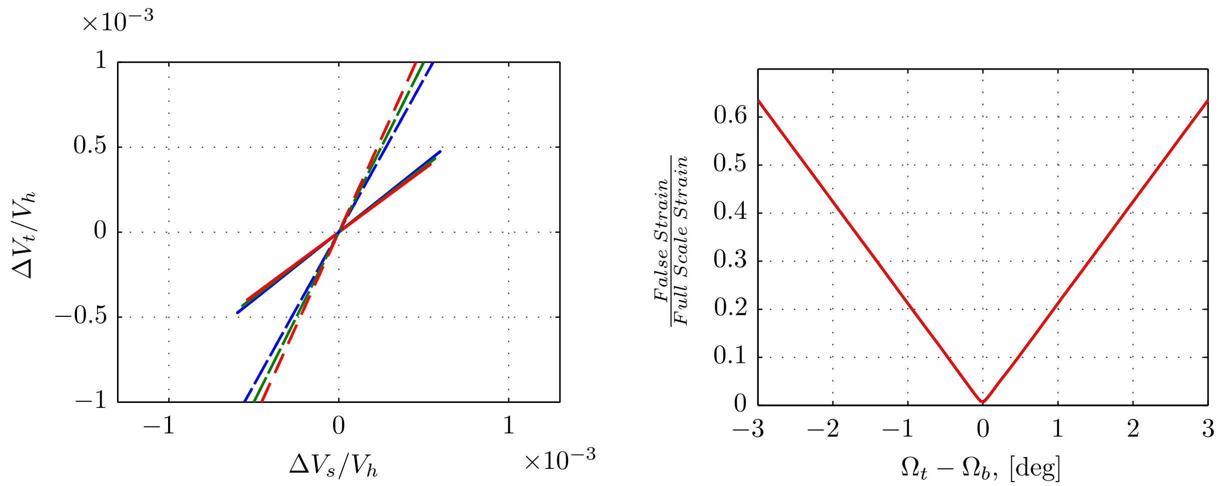

(A) (B)

Figure 4.14: (A) Temperature-only (dashed lines) and strain-only (solid lines) data plot when blue: $\frac{R_{bo}}{R_{tp}} = 0.8$, green: $\frac{R_{bo}}{R_{tp}} = 1.0$, red: $\frac{R_{bo}}{R_{tp}} = 1.2$, (B) Normalized false strain in the temperature-only data simulated from the sinusoidal ETM model of the µF film design [B] when blue: $\frac{R_{bo}}{R_{tp}} = 0.9$, green: $\frac{R_{bo}}{R_{tp}} = 1.0$, red: $\frac{R_{bo}}{R_{tp}} = 1.1$

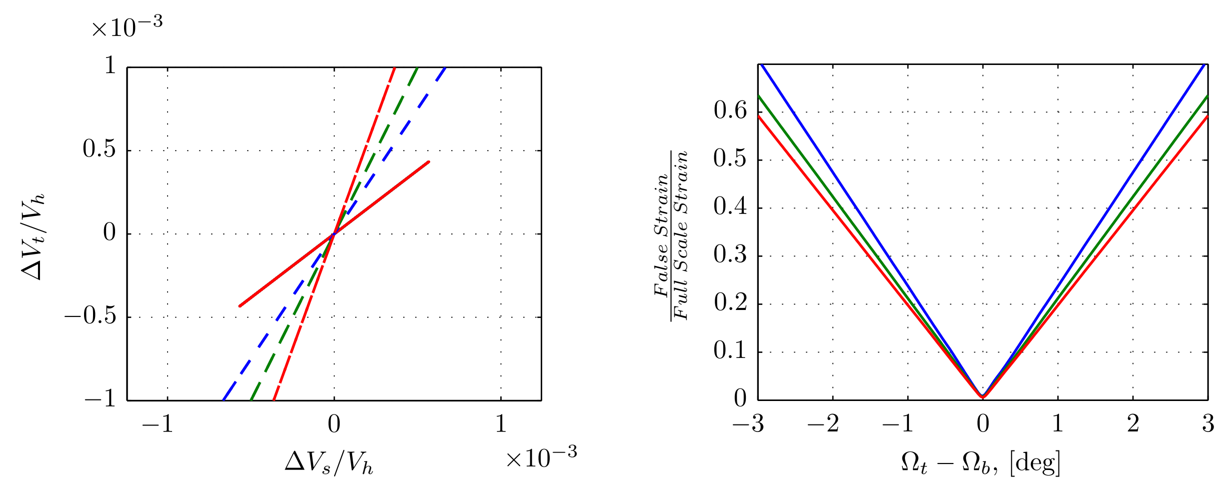

(A) (B)

Figure 4.15: (A) Temperature-only (dashed lines) and strain-only (solid lines) data plot when blue: $\frac{\nu_{bo}}{\nu_{tp}} = 0.8$, green: $\frac{\nu_{bo}}{\nu_{tp}} = 1.0$, red: $\frac{\nu_{bo}}{\nu_{tp}} = 1.2$, (B) Normalized false strain in the temperature-only data simulated from the sinusoidal ETM model of the µF film design [B] when blue: $\frac{\nu_{bo}}{\nu_{tp}} = 0.8$, green: $\frac{\nu_{bo}}{\nu_{tp}} = 1.0$, red: $\frac{\nu_{bo}}{\nu_{tp}} = 1.2$

design [B] ETM model, when $\frac{R_{bo}}{R_{tp}} = 1.0$, $R_a = R_{tp}$, $\frac{\nu_{bo}}{\nu_{tp}} = 1$, and $\frac{\eta_{bo}}{\eta_{tp}}$ is varied from 0.1 to 0.5. Only slope of the strain-only data is varied in this simulation because of different gauge factors. When the ratio of $\frac{\eta_{bo}}{\eta_{tp}}$ is reduced, the angle between temperature-only and strain-only data increases, which results in temperature and strain data that are more independent from each other. Figure 4.16 (B) is the normalized false strain plot when both $\Omega_t - \Omega_b$ and $\frac{\eta_{bo}}{\eta_{tp}}$ are varied. As indicated in the previous simulation conditions, small differences between Ω_b and Ω_t can cause large false strain due to temperature. The difference between η_{bo} and η_{tp} must be large in order to reduce the size of the false strain.

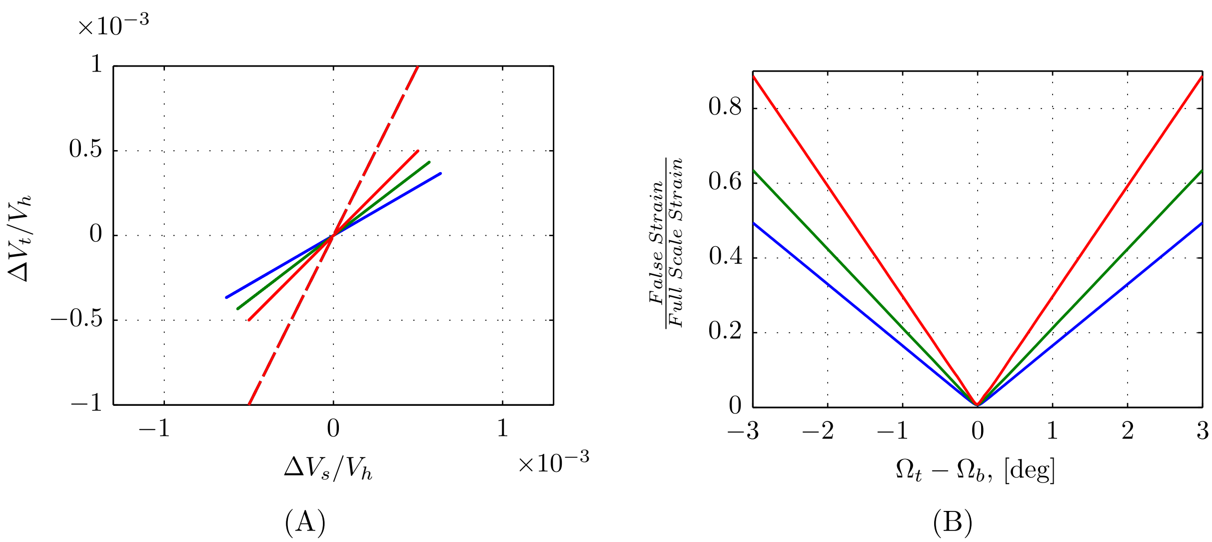

Figure 4.16: (A) Temperature-only (dashed lines) and strain-only (solid lines) plot when blue: $\frac{\eta_{bo}}{\eta_{tp}} = 0.1$, green: $\frac{\eta_{bo}}{\eta_{tp}} = 0.3$, and red: $\frac{\eta_{bo}}{\eta_{tp}} = 0.5$, (B) Normalized false strain in the temperature-only data simulated from the sinusoidal ETM model of the µF film design [B] when blue: $\frac{\eta_{bo}}{\eta_{tp}} = 0.1$, green: $\frac{\eta_{bo}}{\eta_{tp}} = 0.3$, red: $\frac{\eta_{bo}}{\eta_{tp}} = 0.5$

4.5.6 Summary of Key Difficulties and Solutions of the µF Film Design [B]

This µF film design [B] still had large false strain due to temperature. Figure 4.11 (B) indicated that the false strain magnitude was approximately 50% of the full scale strain. The dynamic ETM models were utilized to investigate sources of the false strain. This model predicted that thermal dynamic differences between the parallel and orthogonal heaters/sensors led to large phase shift between $\Delta\frac{V_s}{V_h}$ and $\Delta\frac{V_t}{V_h}$, resulting false strain due to temperature in the measurement. $R_{bo} \neq R_{tp}$ and $\nu_{bo} \neq \nu_{tp}$ did not produce a significant impact on the magnitude of the false strain. However η_{bo} and η_{tp} had to be notably different to reduce the size of the false strain. The μF film design [C] would be focused on matching the thermal dynamics between the parallel and orthogonal heaters/sensors to minimize this false strain.

4.6 [C] One-Layer Left-Right Asymmetric Design

The simplest design technique to eliminate the thermal path difference between the parallel and orthogonal heaters/sensors of the μF film design [B] is to construct both types of heaters/sensors on the same metal layer. The μF film design [C] is constructed based on this concept. The μF tip prototype with the μF film design [C] consists of only one SMA actuator strip to terminate cross coupling between actuator strips. The number of the actuation segments is increased to five segments in order to increase the range of motion. The spine is changed from a super-elastic wire to a patterned SMA, enabling the spine to be precisely aligned and spot-welded directly on the skeleton spring.

4.6.1 The μF Film Design [C] Layout

Figure 4.17 presents the μF film design [C] that has both orthogonal and parallel heaters/sensors on the bottom aluminum layer (blue) and a shared center tap on the top aluminum layer (red area covering over the whole heaters/sensors). Both orthogonal and parallel heaters/sensors were created with meandering pattern to cover the active areas of each segment as much as possible. Vias (dark green squares) connecting heaters/senors to the shared center tap were located on an unactuated segment at the distal end. The left, middle, and right pads were attached to parallel, orthogonal heaters/sensors and center tap, respectively. The μF film design [C] was also fabricated using the co-fabrication technique. All heaters/sensors were intact and had expected resistance during fabrication. However, when SMA actuators were preformed during assembly to enable actuators to be attached on a skeleton spring, the orthogonal heater/sensor design of every fabricated

SMA actuator broke. The μF tip prototype was not successfully built with the μF film design [C]. In addition, an optical microscope was not able to reveal the source of the broken orthogonal heaters/sensors because heaters/sensors were buried underneath the aluminum center tap.

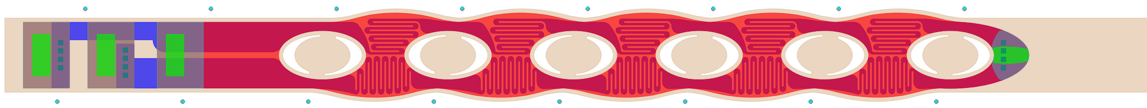

Figure 4.17: An SMA actuator with the μF film design [C] that has parallel and orthogonal heaters/sensors on the bottom aluminum layer and a shared center tap covering the whole heaters/sensors on the top layer

The main question about the μF film design [C] was why the orthogonal heaters/sensors could not survive the bending strain during the preforming process. The μF film design [C] pattern was modified as indicated in Figure 4.18 in order to investigate the source of broken orthogonal heaters/sensors. The μF film design [C*] had identical heater/sensor pattern with the μF film design [C] in Figure 4.17, except the orthogonal heaters/sensors were not covered under the center tap. It allowed orthogonal heaters/sensors to be inspected under an optical microscope, when they were bent. All heaters/sensors were measured their resistance using an ohm meter during fabrication and before preforming process. The measurement indicated that all heaters/sensor were intact. Then the μF film design [C*] was preformed using a custom fixture. The μF film design [C*] had to be able to survive the bending strain upto 6-7% in the preforming process. At the end of the preforming process, all heaters/sensors of the μF film design [C*] were re-measured their resistance. The result indicated that all heaters/sensors could survive the forming process with the resistance change less than 1%. However, only one μF tip prototype was constructed and utilized in further experiments to study the dynamics of the modified μF design [C].

After the μF tip with the modified μF film [C] was successfully assemble, the photo mask of the μF film design [C] in Figure 4.17 was carefully inspected under a high power optical microscope. Finally, the source of the broken orthogonal heaters/sensors was discovered. There were small cracks on the narrow bus of the orthogonal heater/sensor next to the center welding tabs. These cracks on

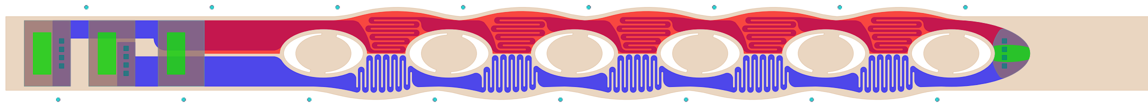

Figure 4.18: An SMA actuator with the µF film design [C*] that has identical heater/sensor layout with the µF film design [C] except the half coverage center tap on the top aluminum layer

the µF actuator strips could not be seen under an optical microscope because they were covered by the aluminum RIE mask. When these orthogonal heaters/sensors were subjected to high bending strain, these cracks propagated across the aluminum heater/sensor trace, causing broken orthogonal heaters/sensors in the µF film design [C].

4.6.2 Temperature and Strain Calibrations of the µF Film Design [C*]

Temperature and strain decoupling coefficients, utilized to extract temperature and strain from $\frac{V_s}{V_h}$ and $\frac{V_t}{V_h}$ signals, are computed using the non-orthogonal projection method from the temperature-only and strain-only data measured from the µF tip with the µF film design [C*]. These coefficients are presented as the H^{-1} matrix in Equation 4.26. Figure 4.19 (A) shows the relationship between measured $\frac{V_s}{V_h}$ and $\frac{V_t}{V_h}$ signals of the temperature-only (blue) and the full scale strain-only (green) data. (B) is the uncoupled temperature and strain from the signals presented in (A) using the H^{-1} matrix in Equation 4.26. The false strain measured from the µF film design [C*] is reduced to approximately 30% of the full scale strain presented in the green color. However, the magnitude of the false strain is still large, hence closed-loop controls are not implemented to control this µF tip. Additional analyses are conducted to gain more understanding in the dynamics of the µF film design [C*] below.

$$H = \begin{pmatrix} 1.0000 & 1.0000 \\ -0.0256 & 9.6786 \end{pmatrix}, \qquad H^{-1} = \begin{pmatrix} 0.9974 & -0.1030 \\ 0.0026 & 0.1030 \end{pmatrix} \tag{4.26}$$

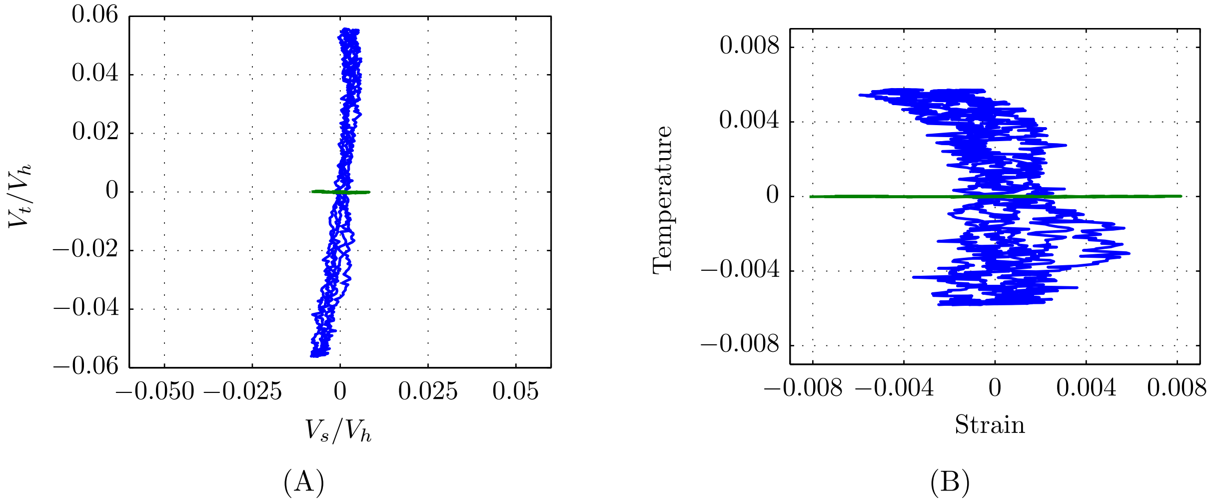

Figure 4.19: Comparison between uncalibrated (A) and calibrated (B) temperature and strain of the μF film design [C*] (blue: temperature-only, green: strain-only)

4.6.3 $\frac{V_s}{V_h}$ and $\frac{V_t}{V_h}$ Models of the μF Film Design [C*]

$\frac{V_s}{V_h}$ and $\frac{V_t}{V_h}$ models are constructed from signals output from the μF tip prototype with the μF film design [C*]. Figure 4.20 shows both simulated and measured $\frac{V_s}{V_h}$ and $\frac{V_t}{V_h}$ signals in the time domain when a step heating power is applied to this μF tip. The simulated $\frac{V_s}{V_h}$ and $\frac{V_t}{V_h}$ signals are constructed utilizing parameters indicated in Table 4.7. Each model is consisted of three parallel low-pass filters with remarkably different time constants leading to dynamic differences in both signals and $\frac{V_s}{V_h}$ drift. In addition, the $\frac{V_s}{V_h}$ signal is significantly noisier than the $\frac{V_t}{V_h}$ signal. Its magnitude is approximately only 30% of the $\frac{V_t}{V_h}$ signal. The possible source of this problem is because the center tap, which covers only the parallel heater/sensor pattern, causes unmatched thermal properties between parallel and orthogonal heater/sensor designs on the left and right sides of the μF film design [C*], respectively. This mismatch can lead to different heater/sensor thermal time constants.

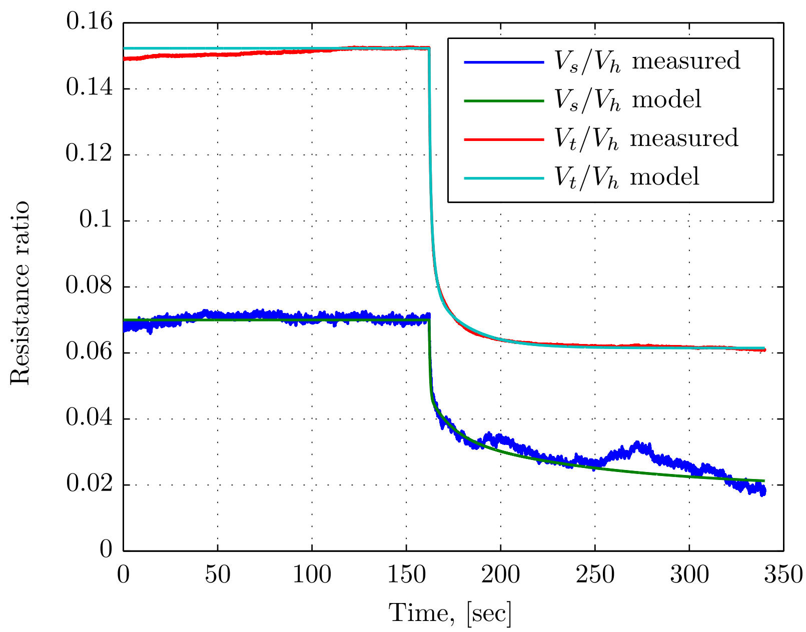

Figure 4.20: Step response of measured and simulated $\frac{V_s}{V_h}$ and $\frac{V_t}{V_h}$ signals from the μF film design [C*]

Table 4.7: Parameters of $\frac{V_s}{V_h}$ and $\frac{V_t}{V_h}$ models of the μF film design [C*]

Parameter	Value
A	0.0050 W
B	0.0700 V/V
C	0.1523 V/V
ΔP	0.0080 W
$\Delta V_s/V_h$	−0.0510 V/V
$\Delta V_t/V_h$	−0.0908 V/V
γ_1	0.4500
γ_2	0.2300
γ_3	0.3200

Parameter	Value
α_1	0.5000 s
α_2	12.0000 s
α_3	90.0000 s
δ_1	0.4000
δ_2	0.4000
δ_3	0.2000
β_1	0.5000 s
β_2	2.3000 s
β_3	19.5000 s

4.6.4 Temperature and Position Control Plant Models of the μF Film Design [C*]

Poles and zeros of the temperature and position control plant models are presented in Figure 4.21 and Table 4.8. Both models are stable and critically damped systems because all poles and zeros are real and located on the left-half complex plane. However, closed-loop controls are not

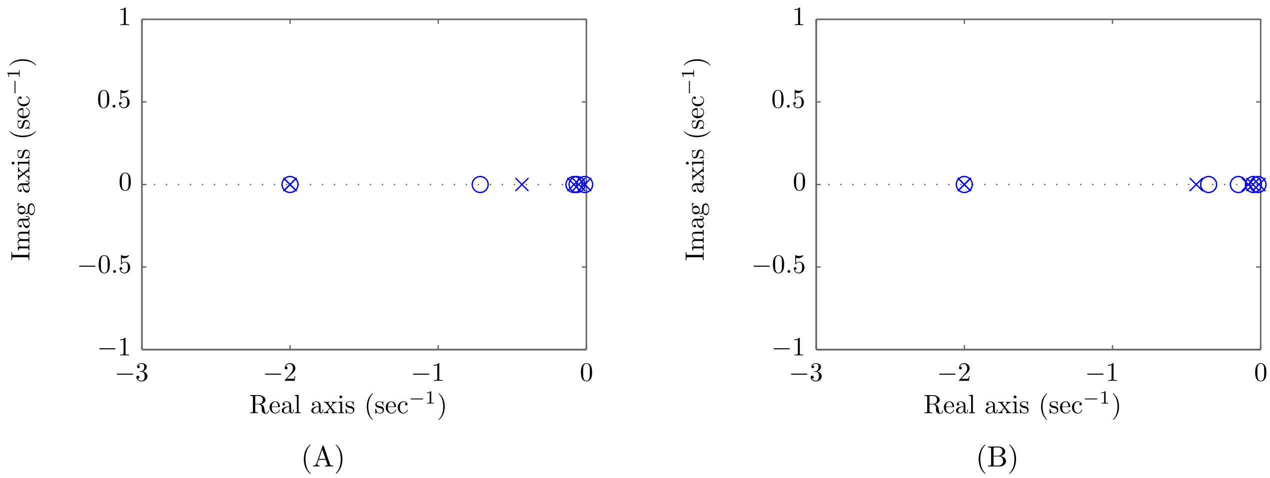

Figure 4.21: Pole and zero of the temperature (A) and position (B) control plant models of the μF film design [C*] plots

implemented on this μF tip with the modified μF film design [C*] because the false strain due to temperature is large compared to the full scale strain. In addition, the $\frac{V_s}{V_h}$ signal requires an additional filter circuit to reduce noise, which can lead to complexity in the temperature and strain extracting process and also can cause additional dynamics that does not present in the temperature and position control plant models.

Table 4.8: Poles and zeros of the temperature (A) and position (B) control plant models of the μF film design [C*]

(A)

poles	zeros
−2.0000	−2.0000
−2.0000	−0.7165
−0.4348	−0.0838
−0.0833	−0.0627
−0.0513	−0.0112
−0.0111	

(B)

poles	zeros
−2.0000	−2.0000
−2.0000	−0.3507
−0.4348	−0.1499
−0.0833	−0.0488
−0.0513	−0.0177
−0.0111	

4.6.5 Temperature and Strain Sensing Analyses of the μF Film Design [C*]

Dynamic ETM models of the μF film design [C*] are utilized to investigate how the heater/sensor pattern can cause large false strain. These models are slightly different from ETM models of the μF film design [B] because the μF film design [C*] consists of single aluminum heater/sensor layer that has parallel (RH_1) and orthogonal (RH_2) patterns on the left and right side of the actuator as indicated in Table 4.2. Hence, heaters/sensors in these models are divided into left and right sides of the μF actuator, instead of top and bottom as in the μF film design [B]. Temperature coefficient of resistances of both parallel and orthogonal heaters/sensors are equal ($\nu_{bp} = \nu_{bo} = \nu$) because they are fabricated on the identical aluminum layer. Equations 4.27 and 4.28 are ETM models of the parallel and orthogonal heaters/sensors, when a sinusoidal heating power $P = \Delta P \sin(\omega t)$ is applied to the μF film design [C*]. ΔT and $\Delta\epsilon$ are temperature and strain change due to the applied sinusoidal heating power. Ω, and θ are phase shifts of the resistance change due to temperature and strain of heaters/sensors. These phase shifts between parallel and orthogonal heaters/sensors are different ($\frac{\Omega_l}{\Omega_r} \neq 1$, $\frac{\theta_l}{\theta_r} \neq 1$) because thermal paths of heaters/sensors are dissimilar due to the half coverage center tap. Subscripts p, o, l, and r indicate parallel and orthogonal heater/sensor patterns, left and right sides of the μF film design [C*], respectively. η is a gauge factor of the heaters/sensors. $\Delta R|_{\Delta T}$ and $\Delta R|_{\Delta\epsilon}$ are resistance changes due to temperature and strain variations.

$$\begin{aligned} RH_1 =& R_p + \Delta R_p|_{\Delta T} + \Delta R_p|_{\Delta\epsilon} \\ \Delta R_p|_{\Delta T} =& R_p \nu \Delta T_l \sin(\omega t + \Omega_l) \\ \Delta R_p|_{\Delta\epsilon} =& R_p \eta_p \Delta\epsilon_l \sin(\omega t + \theta_l) \end{aligned} \tag{4.27}$$

$$\begin{aligned} RH_2 =& R_o + \Delta R_o|_{\Delta T} + \Delta R_o|_{\Delta\epsilon} \\ \Delta R_o|_{\Delta T} =& R_{bo} \nu \Delta T_r \sin(\omega t + \Omega_r) \\ \Delta R_o|_{\Delta\epsilon} =& R_o \eta_o \Delta\epsilon_r \sin(\omega t + \theta_r) \end{aligned} \tag{4.28}$$

There are two possible conditions, which can cause phase difference between $\frac{V_s}{V_h}$ and $\frac{V_t}{V_h}$ signals of the µF film design [C*]. First, the left and right sides of the µF film design [C*] have dissimilar thermal paths due to the asymmetric center tap. This difference can cause thermal time constant mismatch between the parallel and orthogonal heaters/sensors. Therefore Ω_l can be different from Ω_r. Second, the number of squares of the parallel and orthogonal patterns is not equal, which causes $\frac{R_o}{R_p} \neq 1$. Therefore the linearized sinusoidal $\Delta\frac{V_s}{V_h}$ and $\Delta\frac{V_t}{V_h}$ models constructed below will be simulated based on these conditions.

The linearized sinusoidal ETM models of $\Delta\frac{V_s}{V_h}$ and $\Delta\frac{V_t}{V_h}$ ratios, presented in Equations 4.29, and 4.31, can be constructed using the same technique as in Section 4.5.5.

$$\begin{aligned}\Delta\frac{V_s}{V_h} =& \frac{1}{(R_p+R_o+R_a)^2}\Big[(R_p(\alpha\cos(\Omega_r)+\beta\cos(\theta_r)) - (R_o+R_a)(\gamma\cos(\Omega_l)+\kappa\cos(\theta_l)))^2 \\ &+ (R_p(\alpha\sin(\Omega_r)+\beta\sin(\theta_r)) - (R_o+R_a)(\gamma\sin(\Omega_l)+\kappa\sin(\theta_l)))^2\Big]^{1/2} \\ &\sin\left(\omega t + \angle\Delta\frac{V_s}{V_h}\right)\end{aligned} \tag{4.29}$$

$$\angle\Delta\frac{V_s}{V_h} = \tan^{-1}\left(\frac{R_p(\alpha\sin(\Omega_r)+\beta\sin(\theta_r)) - (R_o+R_a)(\gamma\sin(\Omega_l)+\kappa\sin(\theta_l))}{R_p(\alpha\cos(\Omega_r)+\beta\cos(\theta_r)) - (R_o+R_a)(\gamma\cos(\Omega_l)+\kappa\cos(\theta_l))}\right) \tag{4.30}$$

$$\begin{aligned}\Delta\frac{V_t}{V_h} =& \frac{R_a}{(R_p+R_o+R_a)^2}\Big[(\alpha\cos(\Omega_r)+\beta\cos(\theta_r)+\gamma\cos(\Omega_l)+\kappa\cos(\theta_l))^2 \\ &+ (\alpha\sin(\Omega_r)+\beta\sin(\theta_r)+\gamma\sin(\Omega_l)+\kappa\sin(\theta_l))^2\Big]^{1/2} \\ &\sin\left(\omega t + \angle\Delta\frac{V_t}{V_h}\right)\end{aligned} \tag{4.31}$$

$$\angle\Delta\frac{V_t}{V_h} = \tan^{-1}\left(\frac{-(\alpha\sin(\Omega_r)+\beta\sin(\theta_r)+\gamma\sin(\Omega_l)+\kappa\sin(\theta_l))}{-(\alpha\cos(\Omega_r)+\beta\cos(\theta_r)+\gamma\cos(\Omega_l)+\kappa\cos(\theta_l))}\right) \tag{4.32}$$

Where:

$$\alpha = R_o \nu \Delta T_r$$
$$\beta = R_o \eta_o \Delta\epsilon_r \tag{4.33}$$
$$\gamma = R_p \nu \Delta T_l$$
$$\kappa = R_p \eta_p \Delta\epsilon_l$$

Consider the temperature-only case where $\Delta\epsilon = 0$, Equations 4.30, and 4.32 can be simplified to

$$\angle\Delta\frac{V_s}{V_h}|_{\Delta T} = \tan^{-1}\left(\frac{R_p R_o \nu \Delta T_r \sin(\Omega_r) - (R_o + R_a) R_p \nu \Delta T_l \sin(\Omega_l)}{R_p R_o \nu \Delta T_r \cos(\Omega_r) - (R_o + R_a) R_p \nu \Delta T_l \cos(\Omega_l)}\right) \tag{4.34}$$

$$\angle\Delta\frac{V_t}{V_h}|_{\Delta T} = \tan^{-1}\left(\frac{-R_o \nu \Delta T_r \sin(\Omega_r) - R_p \nu \Delta T_l \sin(\Omega_l)}{-R_o \nu \Delta T_r \cos(\Omega_r) - R_p \nu \Delta T_l \cos(\Omega_l)}\right) \tag{4.35}$$

The relationship between temperature-only condition $\Delta\frac{V_s}{V_h}$ and $\Delta\frac{V_t}{V_h}$ signals has minimum false strain when $\left|\angle\Delta\frac{V_s}{V_h}|_{\Delta T} - \angle\Delta\frac{V_t}{V_h}|_{\Delta T}\right| = n \times 180°,\ n = 0, 1, 2, \ldots$. For example, when $\Omega_l = \Omega_r = \Omega$, $\Delta\frac{V_s}{V_h}$ and $\Delta\frac{V_t}{V_h}$ do not have phase shift because $\angle\Delta\frac{V_s}{V_h}|_{\Delta T} = \angle\Delta\frac{V_s}{V_h}|_{\Delta T} = \Omega$. However, when $\Omega_l \neq \Omega_r$, it is not clear how each parameter can affect the magnitude of the false strain. Hence, the linearized $\Delta\frac{V_s}{V_h}$ and $\Delta\frac{V_t}{V_h}$ models from Equations 4.29 and 4.31 will be utilized to explore impacts of these parameters based on the two conditions, which can cause the phase difference in the µF film design [C*] as discussed earlier.

Figure 4.22 presents simulation results of both conditions with the following parameters: $R_p = R_a = 2000\Omega$, R_o is varied from $1600 - 2400\Omega$, $\nu = 1.7 \times 10^{-3} \frac{\Omega}{\Omega\,°\mathrm{C}}$, $\eta_p = 0.3$, and $\eta_o = 0.3 \times \eta_p = 0.09$, ΔT is varied 30 °C in the temperature-only case, and $\Delta\epsilon$ is varied from -0.01 to 0.01 in the strain-only condition. (A) is a plot between $\Delta\frac{V_s}{V_h}$ and $\Delta\frac{V_t}{V_h}$ of the temperature-only and strain-only simulation. This plot indicates that when resistance ratio between R_p and R_o change, it causes slopes between $\Delta\frac{V_s}{V_h}$ and $\Delta\frac{V_t}{V_h}$ of the temperature-only and strain-only conditions to vary. Therefore the non-orthogonal temperature and strain decoupling coefficients must be recomputed for each pair of R_p and R_o. (B) shows the relationship between phase difference between parallel and orthogonal heaters/sensors and normalized false strain with respect to magnitude of the full

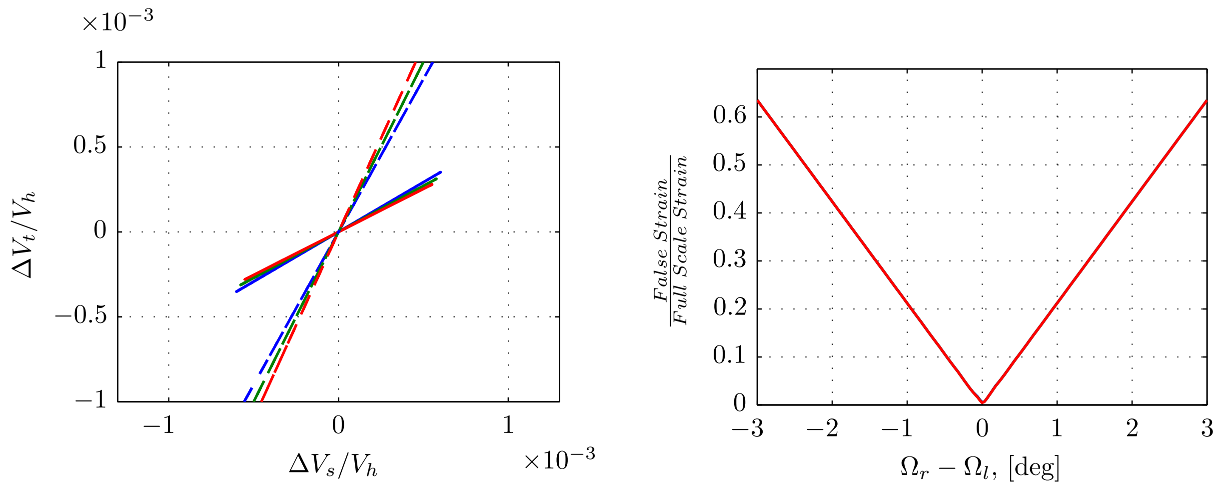

(A) (B)

Figure 4.22: (A) Temperature-only (dashed lines) and strain-only (solid lines) plots of the μF film design [C*] when blue: $\frac{R_o}{R_p} = 0.8$, green: $\frac{R_o}{R_p} = 1.0$, red: $\frac{R_o}{R_p} = 1.2$, (B) false strain due to phase shifts between parallel and orthogonal heater/sensor resistance changes when blue: $\frac{R_o}{R_p} = 0.8$, green: $\frac{R_o}{R_p} = 1.0$, red: $\frac{R_o}{R_p} = 1.2$

scale strain. This plot indicates that the μF film design [C*] also has false strain issue as in the μF film design [B]. Again, a small phase difference in the resistance changes causes large false strain, which can corrupt the strain measurement. Hence, the μF film design [C*] is not suitable to use as a position sensor in the μF tip.

4.6.6 Summary of Key Difficulties and Solutions of the μF Film Design [C*]

The μF film design [C*] still has large false strain due to temperature issue. The source of this false strain is because the parallel and orthogonal heaters/sensors have different thermal dynamics due to the thermal path discrepancies between the left and right sides of the μF film design [C*]. This dissimilarity causes the heating and cooling time constants of both heaters/sensors to be different. Therefore the $\frac{V_s}{V_h}$ signal does not have the same phase with the $\frac{V_t}{V_h}$ signal. It is important that the thermal paths of heaters/sensors must be identical not only between top and bottom but also between left and right sides of the μF actuator in order to minimize the phase difference between $\frac{V_s}{V_h}$ and $\frac{V_t}{V_h}$ signals. The µF film design [D] will be designed based on this constraint to ensure that the parallel and orthogonal heaters/sensors have matched thermal dynamics.

4.7 [D] One-Layer Pairwise Symmetric Design

The understanding accumulated from Sections 4.5.5 and 4.6.5 reveals the most critical constraint of µF film design, which is both parallel and orthogonal heaters/sensors must have identical thermal dynamic properties in order to minimize the phase shift between $\frac{V_s}{V_h}$ and $\frac{V_t}{V_h}$ signals. Identical thermal dynamic properties can be achieved when both types of heaters/sensors have matched thermal masses and thermal paths in all directions. Therefore the goal of the µF film design [D] is to design heaters/sensors based on this important constraint. The rest of the µF tip consists of a D-shape super elastic skeleton spring enabling the spine with integrated welding tabs and alignment features to be precisely welded at the center of the flat segment of the D-shape spring. Alignment features also have long narrow strip extended from both sides of the spine. When they are wrapped around the spring, they form narrow slots at the middle of the curve segment of the D-shape skeleton opposite to the spine. These slots are utilized to guide and align a µF actuator strip on the skeleton during the µF tip assembly process.

4.7.1 The µF Film Design [D] Layout

A basic method to achieve identical thermal path in all directions between parallel and orthogonal heaters/sensors is to construct both types of heaters/sensors on the same metal layer and arrange them symmetrically along the longitudinal axis of the µF actuator strip. On the other hand, the thermal mass is depended on the heating area under the heaters/sensors. Ideally, if the meandering parallel oriented heater/sensor is arranged such that it has square shape, the orthogonal oriented heater/sensor can be achieved by rotating the parallel heaters/sensors 90 degrees. However, the square shape configuration is not suitable for the µF film design because heaters must have total resistance at least 20 times higher than total bus resistance to dissipate 95% of the total heating power at heaters. In addition, the width of heater traces must be wider than 20µm in order to increase the reliability of heaters since they are fabricated directly on the SMA which has rough surface.

All of the μF films up to the μF film design [C*] were designed based on the knowledge and dimension of μF catheters targeted for lung disease treatment. This lung-size μF catheter had the diameter of 1mm. However, the studies of this dissertation were conducted in parallel with μF sinus surgical device research and development, which had the diameter approximately three times larger than the lung-size μF catheters. There were several key discoveries in the sinus surgical device research project and they could be used to improve the μF tip design in this dissertation. One important result was the mechanical model of the μF tip, which could be employed to determine optimal dimensions of the μF actuator strip and the skeleton spring configuration in order to maximize the range of motion and forces that the μF tip could produce. Therefore, the dimensions of the μF film design [D] and the skeleton spring of the next μF tip prototype (e.g. SMA thickness, width, length, spring wire dimension) would be constructed based on the output of this mechanical model.

Figure 4.23 (A) presents the μF film design [D], which has the parallel and orthogonal heaters/sensors arrangement such that they are left-right pairwise symmetrical. Both types of heater/sensor are fabricated on the same aluminum layer (blue color), therefore they have identical thermal paths to the top and bottom. Figure 4.23 (B) is the lung-size μF film design [C*].

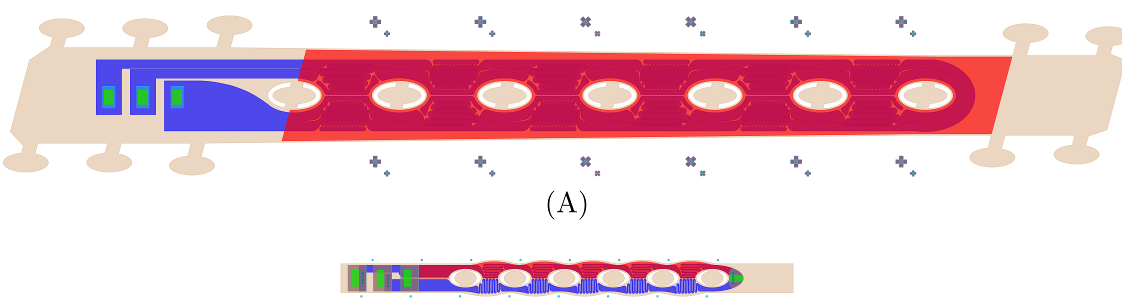

(A)

(B)

Figure 4.23: SMA actuator size and shape comparison between (A) the μF film design [D] and (B) the μF film design [C*]

Both parallel and orthogonal heaters/sensors are uniformly covered by an aluminum layer (translucent red) from an RIE protection mask used to protect the heaters/sensors during pad window and welding tab etching with plasma (detail in Chapter 5). The SMA pattern (light brown color) has the segment length of 2900µm, thickness of 45µm, and taper width varied from 2600µm at the proximal end to 2200µm at the distal end. This taper width actuator outline enables the µF tip to produce large range of motion and smooth µF tip's bending shape by creating large force at the proximal end and less force at the distal end. The welding tabs are located at the center of the strip in the active segments to allow the spring to twist during actuation and located on both sides at the distal and proximal ends to form flat areas for pads and end cap. The left, middle, and right pads are connected to orthogonal, parallel heaters/sensors and center tap, respectively. The µF film design [D] does not contain any via to maximize its reliability.

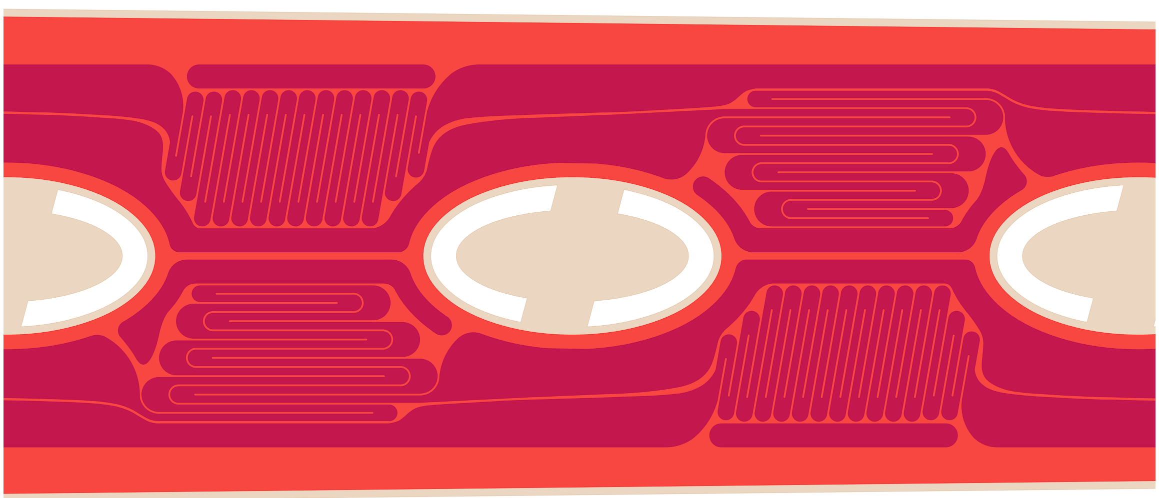

Figure 4.24: Zoom-in of the µF film design [D]

Only two SMA segments are indicated in Figure 4.24, the orthogonal and parallel heater/sensor patterns are alternated along the longitudinal axis of the µF tip to form a symmetric pair in every two segments. The spaces around heater/sensor traces are filled with aluminum in order to produce uniform thermal properties. In addition, the areas covered by the parallel and orthogonal heater/sensor patterns are approximately equal, hence the thermal mass of both of them are roughly the same. The orthogonal heaters/sensors are slightly tilted to align them to the minimum bending strain direction to increase gauge factor difference between parallel and orthogonal heaters/sensors. The μF film design [D] is fabricated on SMA actuators using co-fabrication method. The finished μF actuators are assembled to μF tip prototypes and utilized to study the dynamics of the μF film design [D]. The details of this study are discussed below.

4.7.2 Temperature and Strain Calibrations of the μF Film Design [D]

The non-orthogonal projection is also utilized to decouple temperature and strain from $\frac{V_s}{V_h}$ and $\frac{V_t}{V_h}$ signals of the μF film design [D]. Figure 4.25 (A) presents the measured $\frac{V_s}{V_h}$ and $\frac{V_t}{V_h}$ signals of both temperature-only and strain-only conditions. The slope of both lines are used to compute uncoupling coefficients in H^{-1} in Equation 4.36 for extracting temperature and strain from the measured signals. Interestingly, the temperature-only data (blue) and strain-only (green) plots do not indicate any loop. Figure 4.25 (B) is the extracted temperature and strain of the signals presented in (A) (blue: temperature-only data, green: strain-only data). This plot strongly indicates that the false strain of the μF film design [D] is minimal, approximately only 5% of the full scale strain. From this experiment result, one can conclude that identical thermal masses and thermal paths in both parallel and orthogonal heaters/sensors of the μF film design [D] can eliminate false strain in the measurement. Therefore the μF film design [D] is suitable to use to measure temperature and strain of the μF tip. This discovery is the first key contribution of this dissertation. A μF tip prototype then is assembled from a μF SMA actuator strip with the μF film design [D]. Temperature and position control plant models are constructed in MATLAB and Simulink to develop control algorithms and analyze the performance of the closed-loop control. Then, these algorithms will be implemented on the μF control hardware to conduct real-time control on the μF prototype.

$$H = \begin{pmatrix} 1.0000 & 1.0000 \\ 0.7573 & 1.8845 \end{pmatrix}, \qquad H^{-1} = \begin{pmatrix} 1.6719 & -0.8872 \\ -0.6719 & 0.8872 \end{pmatrix} \tag{4.36}$$

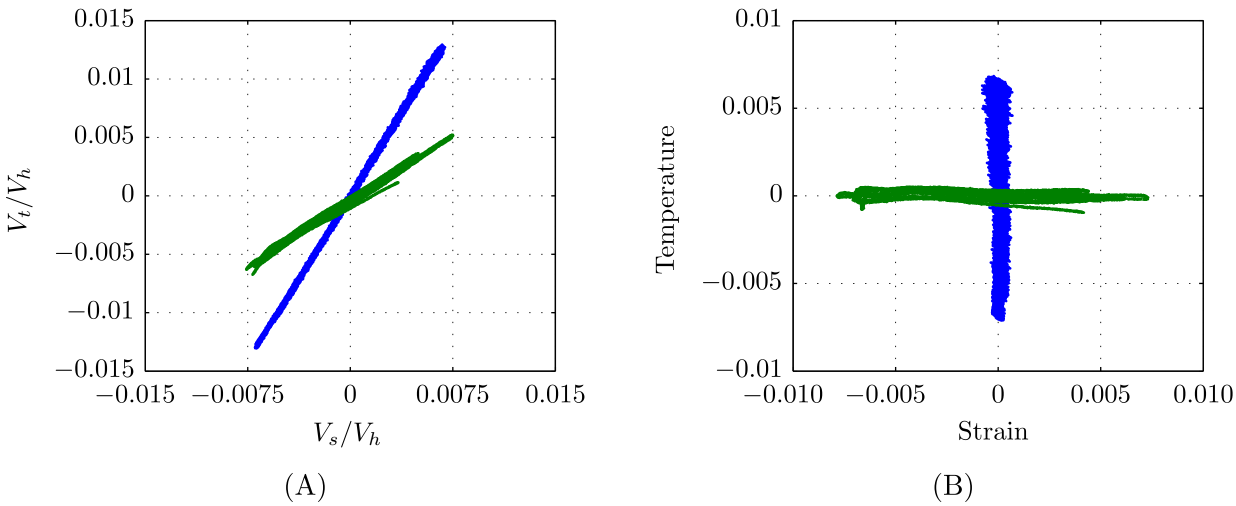

Figure 4.25: (A) measured $\frac{V_s}{V_h}$ and $\frac{V_t}{V_h}$ of the temperature-only and strain-only conditions of the µF film design [D] (B) temperature and strain extracted from the signals presented in (A) (blue: temperature-only, green: strain-only)

4.7.3 $\frac{V_s}{V_h}$ and $\frac{V_t}{V_h}$ models of the µF Film Design [D]

$\frac{V_s}{V_h}$ and $\frac{V_t}{V_h}$ models are constructed utilizing the method described in Section 4.2. A step heating power is applied to the µF tip, then both V_s and V_t signals are measured from the signal conditioning circuit. Both V_s and V_t signals are divided by the heating voltage V_h to create signals being independent from V_h. Figure 4.26 presents both measured and simulated $\frac{V_s}{V_h}$ and $\frac{V_t}{V_h}$ plots in time domain. These plots indicate that the simulated $\frac{V_s}{V_h}$ and $\frac{V_t}{V_h}$ signals are matched with the measured $\frac{V_s}{V_h}$ and $\frac{V_t}{V_h}$ signals. Equations 4.37 and 4.38 are transfer functions from heating power (ΔP_h) to $\frac{V_s}{V_h}$ and $\frac{V_t}{V_h}$. Both transfer functions are stable and minimum phase. Therefore, these models are suitable to use in control design. Table 4.9 lists the value of all parameters utilized to construct $\frac{V_s}{V_h}$ and $\frac{V_t}{V_h}$ simulation models. Both models consist of four parallel low-pass filters. However, two out of four time constants of these low-pass filters are slightly different (6% between α_3 and β_3, and 2.5% between α_4 and β_4). These differences are significantly small compared to the differences in the µF film designs [A], [B], and [C*]. In addition, both $\frac{V_s}{V_h}$ and $\frac{V_t}{V_h}$ models also have identical partition of unity DC gains (e.g. $\gamma_1, \ldots, \gamma_4 \equiv \delta_1, \ldots, \delta_4$). Hence, one can conclude that both $\frac{V_s}{V_h}$ and $\frac{V_t}{V_h}$ signals of the µF film design [D] have similar dynamics.

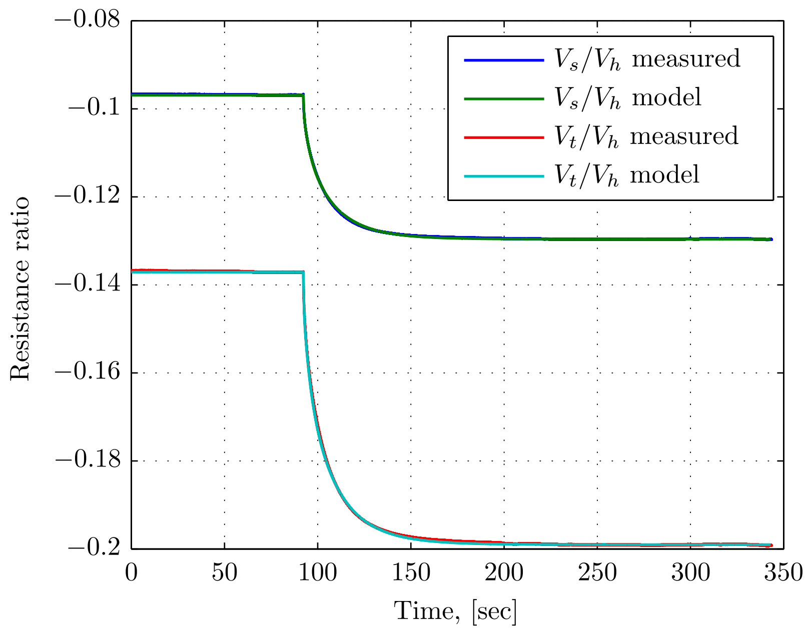

Figure 4.26: Step response of the measured and simulated $\frac{V_s}{V_h}$ and $\frac{V_t}{V_h}$ signals of the µF film design [D]

$$\frac{V_s/V_h}{\Delta P_h} = \frac{(s+0.0642)(s+0.1631)(s+0.9558)}{(s+0.0513)(s+0.0870)(s+0.3333)(s+3.9216)} \tag{4.37}$$

$$\frac{V_t/V_h}{\Delta P_h} = \frac{(s+0.0641)(s+0.1681)(s+0.9614)}{(s+0.0500)(s+0.0926)(s+0.3333)(s+3.9216)} \tag{4.38}$$

4.7.4 Temperature and Position Control Plants of the µF Film Design [D]

Temperature and position control plant models are constructed utilizing $\frac{V_s}{V_h}$ and $\frac{V_t}{V_h}$ models and H^{-1} uncoupling coefficients presented in Sections 4.7.3 and Equation 4.36. Figure 4.27 shows the pole-zero plots of both temperature and position control plant models. Table 4.10 lists all poles and zeros of both control plant models, which are stable and minimum phase. These results raise an

Table 4.9: Parameters of $\frac{V_s}{V_h}$ and $\frac{V_t}{V_h}$ models of the μF film design [D]

Parameter	Value
A	0.0400 W
B	−0.0969 V/V
C	−0.1371 V/V
ΔP	0.0200 W
$\Delta V_s/V_h$	−0.0327 V/V
$\Delta V_t/V_h$	−0.0619 V/V
γ_1	0.1200
γ_2	0.2000
γ_3	0.3000
γ_4	0.3800
α_1	0.2550 s

Parameter	Value
α_2	3.0000 s
α_3	11.5000 s
α_4	19.5000 s
δ_1	0.1200
δ_2	0.2000
δ_3	0.3000
δ_4	0.3800
β_1	0.2550 s
β_2	3.0000 s
β_3	10.8000 s
β_4	20.0000 s

interesting question: why do all four μF film designs presented in this dissertation have minimum phase position control plants?

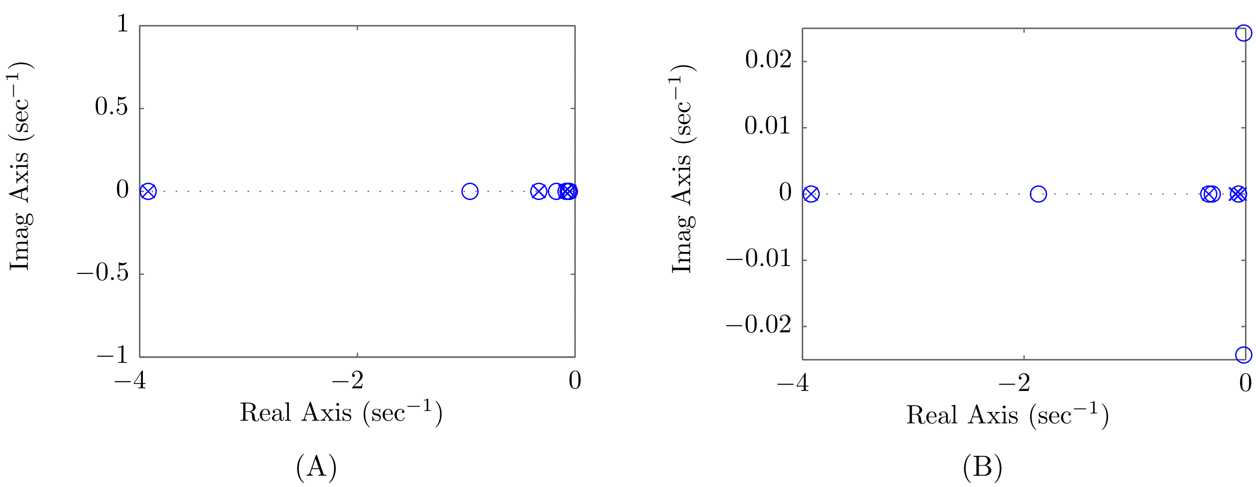

Figure 4.27: Pole and zero of the temperature (A) and position (B) control plant models of the modified μF film design [D] plots

One method of ensuring minimum phase dynamics can be realized as follows. Consider the $\frac{V_s}{V_h}$ and $\frac{V_t}{V_h}$ models in Figure 4.4, consisting of a sum of low-pass filter signals with corresponding time constants ($\alpha_1, \ldots, \alpha_m$, and, $\beta_1, \ldots, \beta_n$) and DC gains ($\gamma_1, \ldots, \gamma_m$, and, $\delta_1, \ldots, \delta_n$) as indicated

Table 4.10: Poles and zeros of the temperature (A) and position (B) control plant models of the modified μF film design [D]

(A)

poles	zeros
−3.9216	−3.9216
−3.9216	−0.9651
−0.3333	−0.3333
−0.3333	−0.1711
−0.0926	−0.0834
−0.0870	−0.0641
−0.0513	−0.0523
−0.0500	

(B)

poles	zeros
−3.9216	−3.9216
−3.9216	−1.8701
−0.3333	−0.3333
−0.3333	−0.3013
−0.0926	−0.0643
−0.0870	$-0.0169 + 0.0243i$
−0.0513	$-0.0169 - 0.0243i$
−0.0500	

in Section 4.2. Suppose α, β, γ, and δ are real and greater than zero. As before, γ, and δ are also a partition of unity. With above conditions, $\frac{V_s}{V_h}$ and $\frac{V_t}{V_h}$ models are always stable because poles of both models are the combination of each first order low-pass filter pole. In addition, both models also have minimum phase dynamics, which can be proved by using the Routh-Hurwitz stability criterion on the numerator of each model. The detail of this proof is provided in Appendix A. Position (S) and temperature (T) control plants are then constructed from the linear combinations of both $\frac{V_s}{V_h}$ and $\frac{V_t}{V_h}$ with the non-orthogonal calibration coefficients H^{-1}. Unfortunately, this calibration can generate a non-minimum phase position or temperature control plant model, even though the constituent models are minimum phase. For example, let:

$$\begin{aligned}\frac{V_s}{V_h} &= \frac{a}{s+a}\\ \frac{V_t}{V_h} &= \frac{b}{s+b}\\ S &= \frac{1}{\det(H)}\left(m_t\frac{V_s}{V_h} - \frac{V_t}{V_h}\right)\end{aligned} \tag{4.39}$$

Suppose $a = 3, b = 1$, $\frac{m_t}{\det(H)} = 1$, and $\frac{1}{\det(H)} = 2$, substitute these parameters in Equation 4.39

$$\frac{V_s}{V_h} = \frac{3}{s+3}$$
$$\frac{V_t}{V_h} = \frac{1}{s+1} \tag{4.40}$$
$$S = \frac{(s-3)}{(s+1)(s+3)}$$

Equation 4.40 shows that $\frac{V_s}{V_h}$, $\frac{V_t}{V_h}$ and S are stable because poles are located on the left half of the complex plane. $\frac{V_s}{V_h}$, $\frac{V_t}{V_h}$ are also minimum phase because both transfer functions have zero at the origin. However, S has non-minimum phase dynamics because the zero $= 3$ is on the right half of the complex plane. This example indicates that the sum of stable and minimum phase transfer functions can generate a stable transfer function with non-minimum phase dynamics.

However, consider the following special case, where $\frac{V_s}{V_h}$ and $\frac{V_t}{V_h}$ have identical dynamics, i.e. $m = n \in \Re$, $\alpha_1, \ldots, \alpha_m \equiv \beta_1, \ldots, \beta_n$, and $\gamma_1, \ldots, \gamma_m \equiv \delta_1, \ldots, \delta_n$. Let $X = \frac{\Delta V_s/V_h}{\Delta P}, Y = \frac{\Delta V_t/V_h}{\Delta P}$. Both X, and Y are constant real numbers. The transfer functions from ΔP to both $\frac{\Delta V_s}{V_h}$, and $\frac{\Delta V_t}{V_h}$ can be written as Equation 4.41

$$\frac{\Delta V_s}{V_h} = X\left(\frac{\gamma_1}{\alpha_1 s+1} + \frac{\gamma_2}{\alpha_2 s+1} + \ldots + \frac{\gamma_m}{\alpha_m s+1}\right)\Delta P$$
$$\frac{\Delta V_t}{V_h} = Y\left(\frac{\gamma_1}{\alpha_1 s+1} + \frac{\gamma_2}{\alpha_2 s+1} + \ldots + \frac{\gamma_m}{\alpha_m s+1}\right)\Delta P \tag{4.41}$$

Let

$$\Lambda(\gamma,\alpha) = \left(\frac{\gamma_1}{\alpha_1 s+1} + \frac{\gamma_2}{\alpha_2 s+1} + \ldots + \frac{\gamma_m}{\alpha_m s+1}\right) \tag{4.42}$$

Where $\Lambda(\gamma,\alpha)$ is stable and minimum phase. Next, temperature and strain can be uncoupled from $\frac{\Delta V_s}{V_h}$, and $\frac{\Delta V_t}{V_h}$ using H^{-1} in Equation 3.31.

$$\Delta S = \frac{1}{\det(H)}\left(m_t\frac{\Delta V_s}{V_h} - \frac{\Delta V_t}{V_h}\right)$$
$$\Delta T = \frac{1}{\det(H)}\left(-m_s\frac{\Delta V_s}{V_h} + \frac{\Delta V_t}{V_h}\right) \tag{4.43}$$

Substitute Equations 4.41 and 4.42 in Equation 4.43

$$\Delta S = \frac{1}{\det(H)}\left(m_t X - Y\right)\Lambda(\gamma,\alpha)\Delta P$$
$$\Delta T = \frac{1}{\det(H)}\left(-m_s X + Y\right)\Lambda(\gamma,\alpha)\Delta P \tag{4.44}$$

Equation 4.44 indicates that both ΔT and ΔS are stable and minimum phase if $\Lambda(\gamma, \alpha)$ is stable and minimum phase. Hence, one can conclude that stable and minimum phase temperature and position control plants can be achieved when the dynamics between $\frac{V_s}{V_h}$ and $\frac{V_t}{V_h}$ are matched. The realization of the effects of these dynamics on the minimum phase problem is the second key contribution of this dissertation. In addition, the dynamic similarity between $\frac{V_s}{V_h}$ and $\frac{V_t}{V_h}$ was shown in Section 4.7.3 to be a mandatory requirement to eliminate loops between $\frac{V_s}{V_h}$ and $\frac{V_t}{V_h}$, which can cause false strain in the measurement. Therefore, matching these dynamics is proposed as a fundamental design goal for heater/sensor films in the μF application.

4.7.5 Closed-loop Control Design and Implementation

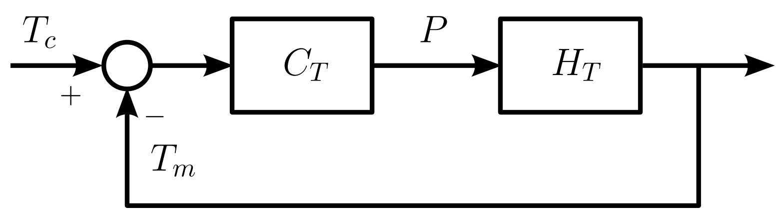

Figure 4.28: The μF closed-loop proportional and integral temperature feedback control algorithm

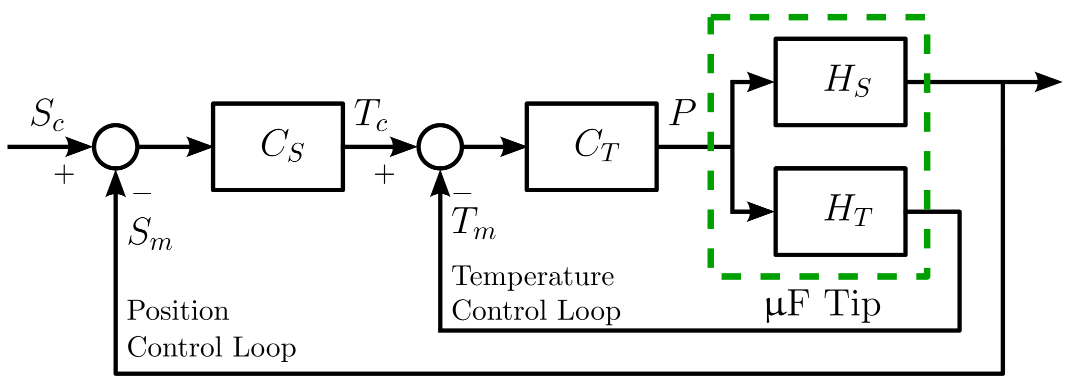

Figure 4.29: The μF closed-loop proportional and integral temperature and position feedback control algorithm

There are two closed-loop control algorithms (temperature-only, and position-temperature) implemented to control the deflection and utilized to evaluate performance of the μF tip. Both closed-loop control algorithms are implemented using proportional and integral (PI) controllers because they are simple and also can provide excellent tracking performance due to their infinite DC gains. The closed-loop PI control with temperature feedback technique feed back only the temperature of the μF tip. The simplified block diagram of this control algorithm is presented in Figure 4.28. However, the closed-loop PI control with position and temperature feedback control method relies on both temperature (the inner control loop) and position (strain, the outer control loop) of the μF tip. Temperature and position (strain) in both control algorithms are measured with the integrated temperature and strain sensors in the μF film. The block diagram of this algorithm is shown in Figure 4.29. Both control algorithms were designed and simulated in MATLAB and Simulink to ensure that the control loops are stable, and have expected responses and performance. These simulation models utilized the temperature ($H_T(s)$) and position ($H_S(s)$) control plants developed in Section 4.7.4. These Simulink models were then translated to C code, complied to an executable program, and transferred to the target computer, which was connected to the μF system through analog-to-digital and digital-to-analog converters, through the MATLAB xPC target module. Finally, these control algorithms were executed in real-time and the measurement data was recorded, and transferred back to the host computer to analyze the performance and the behavior of the closed-loop system. These results are described in detail below.

Closed-Loop PI Control with Temperature Feedback

The temperature control plant of the μF tip with μF film design [D] is stable and minimum phase. However most of the poles and zeros of this control plant are close to the imaginary axis, which can lead to slow response of the closed-loop system. To increase the performance of the closed-loop system, higher gains are used to shift these slow poles further away from the imaginary axis in the left-half complex plane. PI control was utilized to control the temperature due its low tracking error. The final proportional (KP_T) and integral (KI_T) gains, which are implemented in $C_T(s)$ in Figure 4.28, are $KP_T = 0.01$ $[\frac{\mathrm{W}}{\mathrm{C}}]$, $KI_T = 0.04$ $[\frac{\mathrm{W}}{\mathrm{C}\times\mathrm{s}}]$.

Figures 4.30 and 4.31 are the Bode and the Nyquist diagrams of the negative loop gain of this

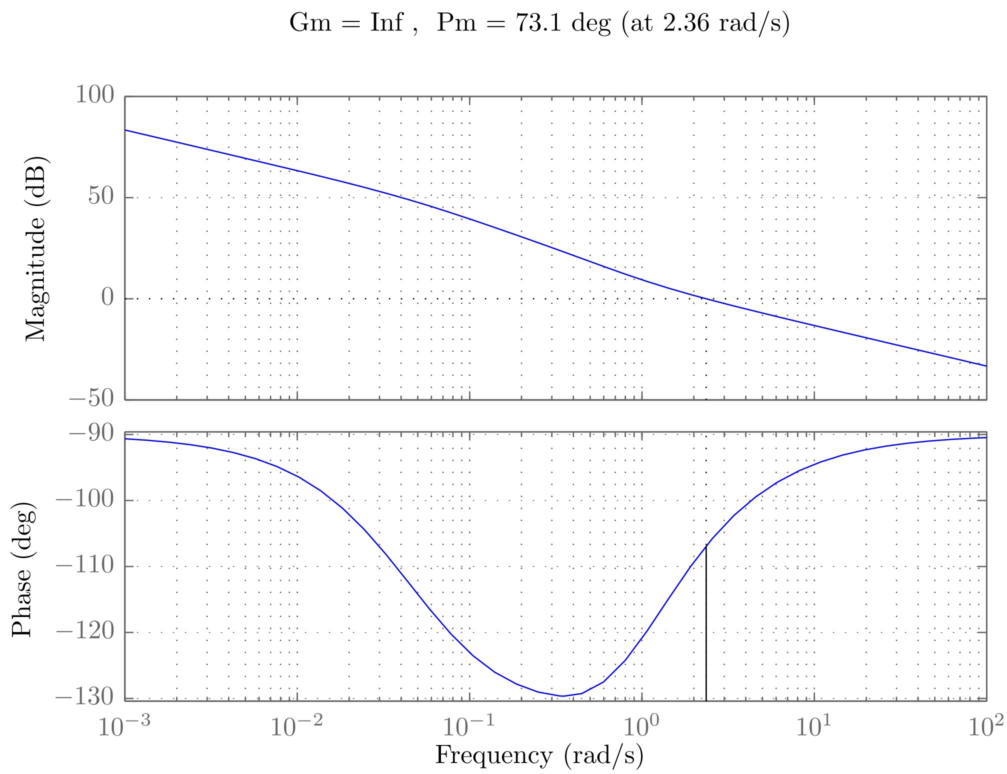

Figure 4.30: Bode diagram of the negative loop gain of the closed-loop temperature feedback control

temperature control system. The Nyquist diagram indicates that this closed-loop system is stable because the negative loop gain does not have any unstable poles and the Nyquist contour does not encircle -1. The bode diagram also confirms this conclusion because the negative loop gain has infinite gain margin, and the phase margin of 73.1 degrees at 2.36 rad/sec. Therefore, this closed-loop control is a well-behaved system with good stability margins. However the -3dB bandwidth of this closed-loop system is approximately only 0.5Hz, which is approximately 10 times lower than the temperature control bandwidth presented in [Aphanuphong, 2008]. The low bandwidth is expected because the size of this μF tip is almost 4 times larger than the μF tip presented in [Aphanuphong, 2008]. The response speed of the μF tip is mainly limited by the heating and cooling rates of the SMA, which depend on the size and thermal mass of the actuators.

Figure 4.32 is the plot of reference tip deflection (blue), measured tip deflection using external

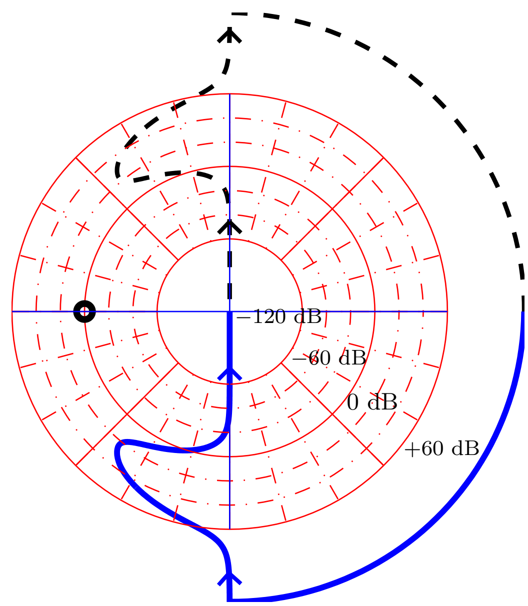

Figure 4.31: Nyquist diagram of the negative loop gain of the closed-loop temperature feedback control

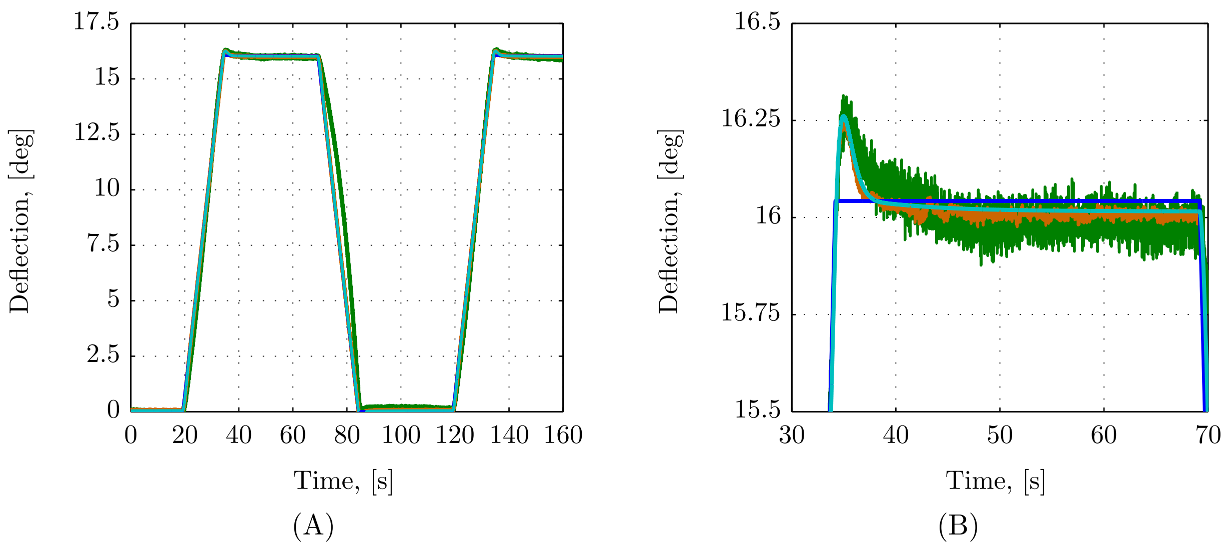

Figure 4.32: Tip deflection (green), reference (blue), simulated (cyan), and measured (brown) position calibrated from temperature vs. time

two dual-axis lateral effect cells (optical position sensor) from On-Trak Photonics, Inc. (green), and the μF film (brown) vs. time. The reference and measured deflection using the μF film are calibrated from reference temperature, and measured temperature, respectively. This reference temperature is also fed into the simulation model, then the simulated temperature tracking output is calibrated to position and plotted in cyan color. The overall result indicates that the tip deflection can be controlled through the temperature of the μF tip with tracking error less than 3% during cool down. This closed-loop control has overshoot and steady state error less than 1.5% and 1.0%, respectively. Furthermore the simulation model developed in Simulink can precisely capture the dynamics of the μF system with the error less than 0.5%.

Closed-Loop PI Control with Position and Temperature Feedback This control

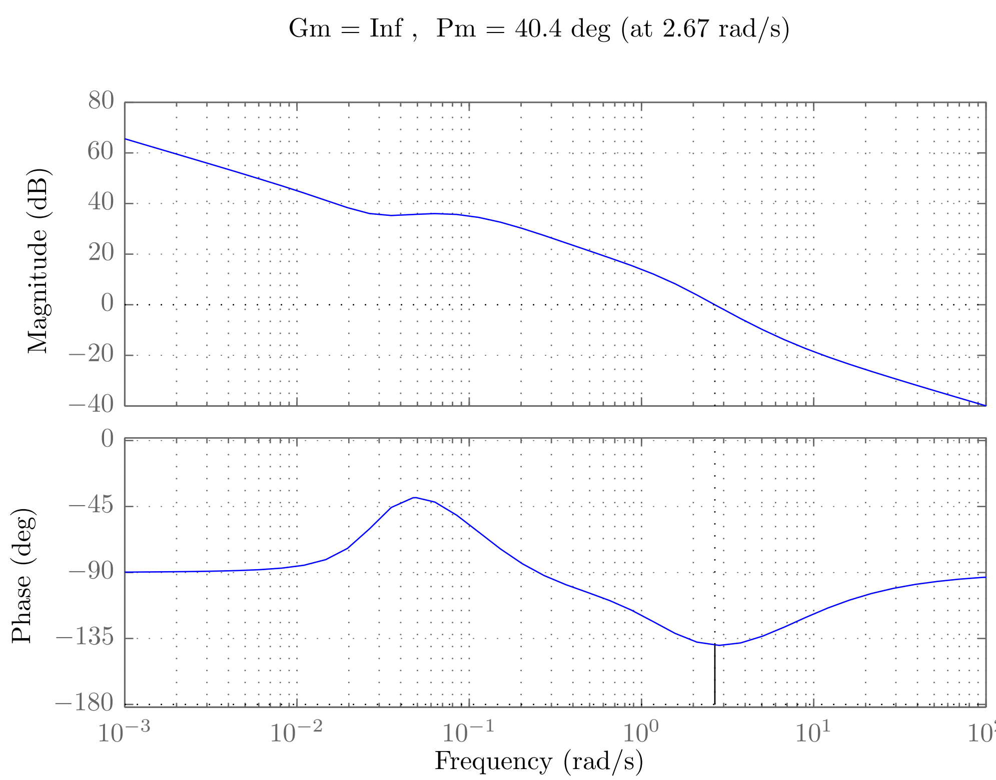

Figure 4.33: Bode plot of the negative loop gain of the closed-loop temperature and position feedback control

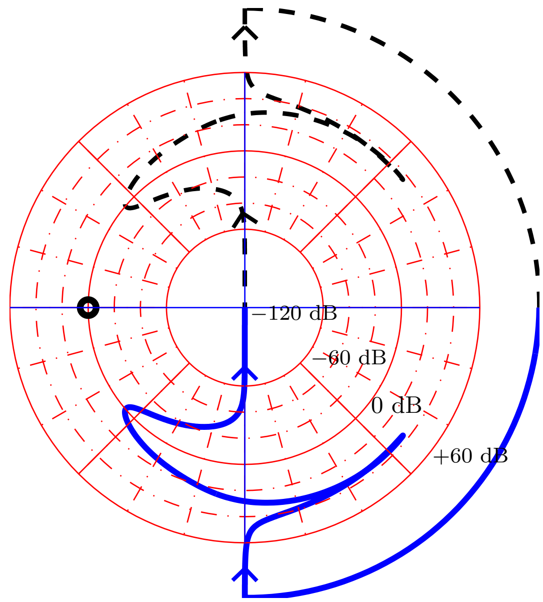

Figure 4.34: Nyquist plot of the negative loop gain of the closed-loop temperature and position feedback control

system consists of two closed-loop systems, the inner loop from T_c to T_m is the temperature control, which is designed and implemented earlier. The outer loop from S_c to S_m is the closed-loop control with the position (strain) feedback. The closed-loop temperature feedback is included in the position control algorithm because the study in Section 4.7 in [Aphanuphong, 2008] indicates that temperature control can be employed to reject temperature disturbances from the environment.

Both KP_T and KI_T gains of the inner loop utilize the values from the closed-loop temperature feedback in the previous section because they can produce a well behaved temperature system. The closed-loop position feedback in the outer loop is first modeled and simulated in MATLAB and Simulink to determine suitable proportional (KP_S) and integral (KI_S) gains. However, most of the poles of the position control plant presented in Section 4.7.4 are close to the imaginary axis, hence, this system has slow response speed. All of these slow poles must be shifted farther away from the imaginary axis in the left-half of the complex plane, resulting in the controller $C_S(s)$ which has

$KP_S = 100\ [\frac{\text{C}}{\text{V}}]$, and $KI_S = 600\ [\frac{\text{C}}{\text{V}\times\text{s}}]$.

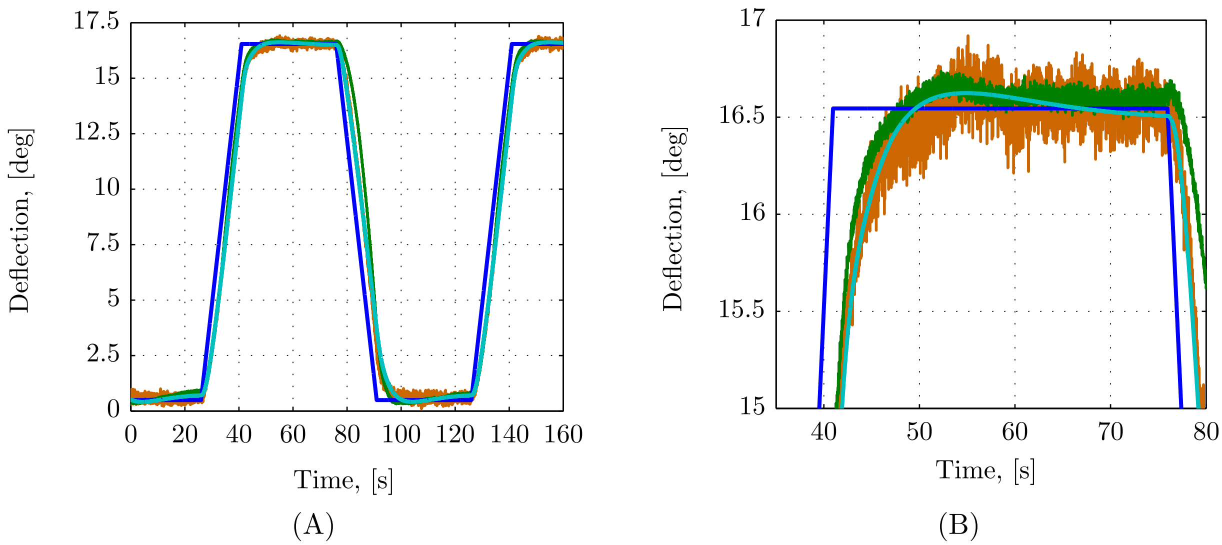

Figure 4.35: Measured and simulated deflection of the µF tip using the closed-loop PI control with position and temperature feedback, (blue: reference deflection, cyan: simulated position tracking, green: measured position with external position sensors, brown: measured position with the µF film)

Figures 4.33 and 4.34 are the Bode and Nyquist diagrams of the negative loop gain of the position control system from S_c to S_m. The negative loop gain of this system does not have any unstable poles in the right-half of the complex plane and the Nyquist contour of this negative loop gain does not encircle -1. Hence, this closed-loop system is stable. The Bode diagram also shows that this negative loop gain has infinite gain margin and the phase margin of 40.4 deg at 2.67 rad/sec. The -3dB bandwidth of this closed-loop control is 0.6Hz.

These control parameters were then implemented on the µF system. Figure 4.35 is the plot of the position control experiment. The green color indicates the deflection of the µF tip measured with optical position sensors. The blue and brown color plots are the reference and measured positions of the µF heaters/sensors scaled and calibrated to match with the tip deflection. The measured position is noisy because large control gains are employed in the closed-loop control to increase the performance of the µF tip. This reference position is also fed into the simulation model, which is utilized to design this closed-loop system. The cyan color is the scaled and calibrated position tracking response from the simulation model. This experiment shows that there is only a slight overshoot of approximately 1% in the tip deflection and position tracking for both measured and simulated responses. The 1% settling time was 7 seconds. The simulated position tracking can match with the measured position very well, which indicates that the position control plant identified in Section 4.7.4 can capture important dynamics for this closed-loop PI control.

4.7.6 Position Measurement Analysis of the μF Film Design [D]

As previously presented in Section 4.6.5, the left and right sides of the actuator strip can have slight different thermal paths due to the configuration of the μF tip. Therefore Ω_l may not be equal to Ω_r. It is interesting to see how this difference impact the dynamics of $\frac{V_s}{V_h}$ and $\frac{V_t}{V_h}$ signals of the μF film design [D]. Figure 4.23 (A) shows that the parallel and orthogonal heaters/sensors are evenly distributed on both sides of the μF actuator strip. Equations 4.45 and 4.46 are the sinusoidal ETM models of these heaters/sensors, which have half of each heater/sensor can be subjected to left and right side dynamics of the μF actuator. The subscripts b, p, o, l and r are bottom layer, parallel, orthogonal designs, and left, right sides of the actuator strip, respectively. The TCRs of both parallel and orthogonal heaters/sensors in this design are identical because they are fabricated on the same aluminum layer.

$$\begin{aligned} RH_1 =& R_p + \Delta R_p|_{\Delta T} + \Delta R_p|_{\Delta \epsilon} \\ \Delta R_p|_{\Delta T} =& \frac{R_p}{2}\nu\left(\Delta T_l \sin(\omega t + \Omega_l) + \Delta T_r \sin(\omega t + \Omega_r)\right) \\ \Delta R_p|_{\Delta \epsilon} =& \frac{R_p}{2}\eta_p\left(\Delta \epsilon_l \sin(\omega t + \theta_l) + \Delta \epsilon_r \sin(\omega t + \theta_r)\right) \end{aligned} \tag{4.45}$$

$$\begin{aligned} RH_2 =& R_o + \Delta R_o|_{\Delta T} + \Delta R_o|_{\Delta \epsilon} \\ \Delta R_o|_{\Delta T} =& \frac{R_o}{2}\nu\left(\Delta T_l \sin(\omega t + \Omega_l) + \Delta T_r \sin(\omega t + \Omega_r)\right) \\ \Delta R_o|_{\Delta \epsilon} =& \frac{R_o}{2}\eta_o\left(\Delta \epsilon_l \sin(\omega t + \theta_l) + \Delta \epsilon_r \sin(\omega t + \theta_r)\right) \end{aligned} \tag{4.46}$$

$$\begin{aligned}\Delta\frac{V_s}{V_h} =& \frac{1}{2(R_p+R_o+R_a)^2}\Big[\\ &(-\alpha(\Delta T_l\cos(\Omega_l)+\Delta T_r\cos(\Omega_r))+\beta(\Delta\epsilon_l\cos(\theta_l)+\Delta\epsilon_r\cos(\theta_r)))^2\\ &+(-\alpha(\Delta T_l\sin(\Omega_l)+\Delta T_r\sin(\Omega_r))+\beta(\Delta\epsilon_l\sin(\theta_l)+\Delta\epsilon_r\sin(\theta_r)))^2\Big]^{1/2}\\ &\sin\left(\omega t+\angle\Delta\frac{V_s}{V_h}\right)\end{aligned} \tag{4.47}$$

$$\angle\Delta\frac{V_s}{V_h} = \tan^{-1}\left(\frac{-\alpha(\Delta T_l\sin(\Omega_l)+\Delta T_r\sin(\Omega_r))+\beta(\Delta\epsilon_l\sin(\theta_l)+\Delta\epsilon_r\sin(\theta_r))}{-\alpha(\Delta T_l\cos(\Omega_l)+\Delta T_r\cos(\Omega_r))+\beta(\Delta\epsilon_l\cos(\theta_l)+\Delta\epsilon_r\cos(\theta_r))}\right) \tag{4.48}$$

$$\begin{aligned}\Delta\frac{V_t}{V_h} =& \frac{R_a}{2(R_p+R_o+R_a)^2}\Big[(\gamma(\Delta T_l\cos(\Omega_l)+\Delta T_r\cos(\Omega_r))+\kappa(\Delta\epsilon_l\cos(\theta_l)+\Delta\epsilon_r\cos(\theta_r)))^2\\ &+(\gamma(\Delta T_l\sin(\Omega_l)+\Delta T_r\sin(\Omega_r))+\kappa(\Delta\epsilon_l\sin(\theta_l)+\Delta\epsilon_r\sin(\theta_r)))^2\Big]^{1/2}\\ &\sin\left(\omega t+\angle\Delta\frac{V_t}{V_h}\right)\end{aligned} \tag{4.49}$$

$$\angle\Delta\frac{V_t}{V_h} = \tan^{-1}\left(\frac{-\gamma(\Delta T_l\sin(\Omega_l)+\Delta T_r\sin(\Omega_r))-\kappa(\Delta\epsilon_l\sin(\theta_l)+\Delta\epsilon_r\sin(\theta_r))}{-\gamma(\Delta T_l\cos(\Omega_l)+\Delta T_r\cos(\Omega_r))-\kappa(\Delta\epsilon_l\cos(\theta_l)+\Delta\epsilon_r\cos(\theta_r))}\right) \tag{4.50}$$

Where:

$$\begin{aligned}\alpha &= R_aR_p\nu\\ \beta &= (R_pR_o\eta_o-(R_o+R_a)R_p\eta_p)\\ \gamma &= (R_o+R_p)\nu\\ \kappa &= (R_o\eta_o+R_p\eta_p)\end{aligned} \tag{4.51}$$

Consider the temperature-only case where $\Delta\epsilon = 0$, Equations 4.48 and 4.50 can be simplified to

$$\angle\Delta\frac{V_s}{V_h}|_{\Delta T} = \tan^{-1}\left(\frac{\Delta T_l\sin(\Omega_l)+\Delta T_r\sin(\Omega_r)}{\Delta T_l\cos(\Omega_l)+\Delta T_r\cos(\Omega_r)}\right) \tag{4.52}$$

$$\angle\Delta\frac{V_t}{V_h}|_{\Delta T} = \tan^{-1}\left(\frac{\Delta T_l\sin(\Omega_l)+\Delta T_r\sin(\Omega_r)}{\Delta T_l\cos(\Omega_l)+\Delta T_r\cos(\Omega_r)}\right) \tag{4.53}$$

The analysis results in Equations 4.52, and 4.53 indicate that $\Delta\frac{V_s}{V_h}$ and $\Delta\frac{V_t}{V_h}$ signals with temperature-only condition are always in-phase because $\angle\Delta\frac{V_s}{V_h}|_{\Delta T}$ and $\angle\Delta\frac{V_t}{V_h}|_{\Delta T}$ are identical. Therefore the dynamic differences between left and right, which presented as Ω_l and Ω_r, cannot cause the phase shift between $\Delta\frac{V_s}{V_h}$ and $\Delta\frac{V_t}{V_h}$ in the temperature-only case. Therefore, one can conclude that the false strain due to temperature is always minimum in the μF film design [D].

4.7.7 Temperature and Strain Sensing Performance of the μF film design [D]

The experiment result in Section 4.7.2 indicates that the μF film design [D] is suitable to use as a temperature and strain sensors because it has minimum false strain. However, to be utilized as temperature and strain sensors, ideally, both parallel and orthogonal heaters/sensors must also have identical temperature coefficient of resistance (TCR) and the TCR of both heaters/sensors must be a constant over the operating temperature range. In addition, the both heaters/sensors must respond to strain differently to achieve independent temperature and strain measurement as discussed in Section 3.1.3. Additional experiments are conducted in this section to ensure that the μF film design [D] also satisfies both temperature and strain sensor conditions.

Temperature Measurement One important assumption in μF film design is when both parallel and orthogonal heaters/sensors are fabricated on the same aluminum layer, they have identical TCR because TCR depends on the crystal structure of the material used to construct sensors, but does not depend on the pattern of the sensors. This assumption can be validated by measuring the resistance of both parallel and orthogonal heaters/sensors of a flat μF actuator strip when temperature is varied.

Figure 4.36 shows the result of this experiment. The blue and green plots are the relationship between normalized resistance variation and temperature change from room temperature of parallel and orthogonal heaters/sensors of the μF film design [D], respectively. This plot indicates that the resistance changes of both heaters/sensors are linearly proportional to temperature change within the operating range. In addition, TCRs of both heaters/sensors, the slopes of both lines, are identical and constant. Since the TCRs of the heaters/sensors are the slopes of both lines, therefore one can conclude that both parallel and orthogonal heaters/sensors fabricated on the same aluminum layer have identical TCR.

aluminum is a suitable material to utilize as a heater/sensor metal layer of μF films.

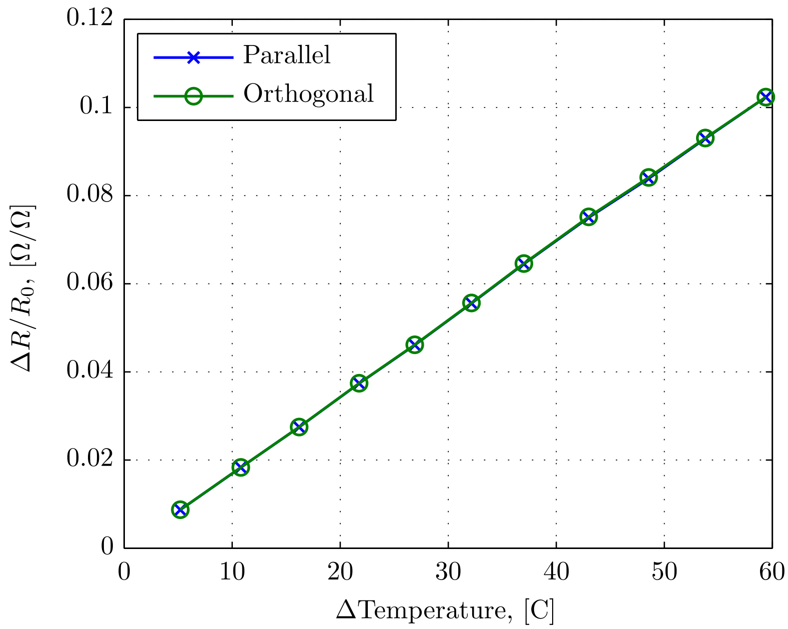

Figure 4.36: Normalized resistance changes of the parallel and orthogonal heaters/sensors of the μF film design [D] (single aluminum heater/sensor layer) when the temperature is varied

Strain Measurement Independent strain measurement in the μF films is achieved when parallel and orthogonal heaters/sensors respond to strain differently. Therefore, it is important to verify that resistance of parallel and orthogonal heaters/sensors change differently when they are subjected to similar strain. An experiment is setup to validate this assumption by stretching a μF tip with the μF film design [D] at room temperature then the resistance of both heaters/sensors are measured and recorded at every stretching position with an ohmmeter.

Figure 4.37 shows the result of this experiment. When the μF tip with the μF film design [D] is stretched, the normalized resistance changes of the parallel (blue) heater/sensor are approximately

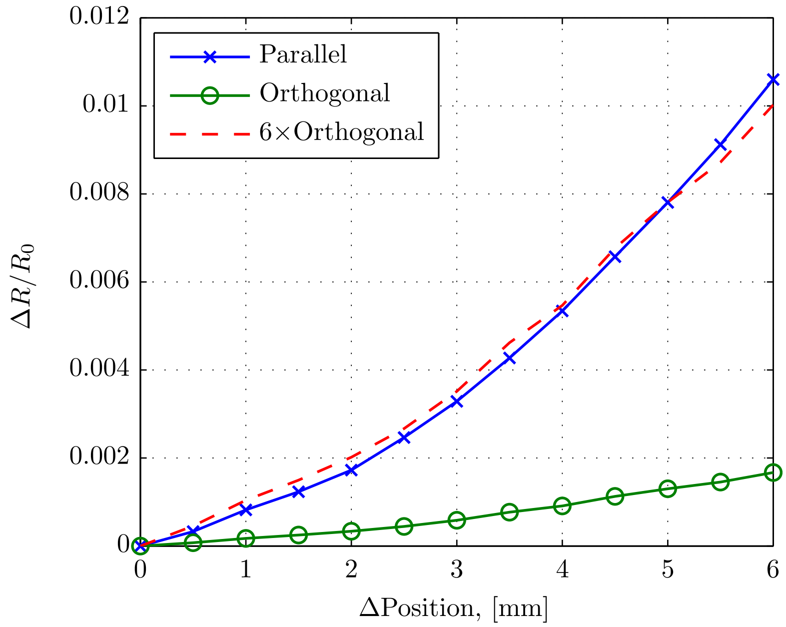

Figure 4.37: The relationship between normalized resistance changes of parallel (blue) and orthogonal (green) heaters/sensors of the μF film design [D] and stretched positions of the μF tip

6 times greater than the normalized resistance changes of the orthogonal (green) heater/sensor, which indicates that the gauge factor of the parallel heater/sensor is about 6 times greater than the gauge factor of the orthogonal heater/sensor. As discussed in Section 4.5.5, large gauge factor difference between both heaters/sensors causes the strain to be independent from the temperature. This independent strain can be extracted from $\frac{V_s}{V_h}$ and $\frac{V_t}{V_h}$ signals using non-orthogonal projection method described in Section 3.2.2. Therefore, one can conclude that the μF film design [D] is suitable to utilize as a strain sensor in the μF catheter.

4.7.8 Summary

Experiment results in this section indicates that the μF film design [D] is able to provide temperature and strain measurements with minimum false strain due to temperature. The minimum false strain property of the μF film design [D] is achieved when the parallel and orthogonal heaters/sensors have identical thermal dynamics and symmetrical design, e.g. matched thermal paths and masses in all directions. Closed-loop temperature and position controls are implemented to control and explore dynamic behaviors of the μF tip prototype with the μF film design [D]. These control algorithms are able to provide reasonable stability margins. However, the closed-loop control bandwidths of both temperature and position controls are low. This μF tip prototype has low control bandwidths because the heating and cooling rates are limited by the size of the μF tip prototype, which is approximately three times larger than the μF tip presented in [Aphanuphong, 2008]. Chapter 5 will be discussed the co-fabrication process, the third contribution of this dissertation. This unique fabrication technique enables μF films to be constructed directly on SMA actuators without utilizing silicone adhesive to bond μF films to SMA actuators.

Chapter 5

μF Tip Fabrication

A μF actuator used to be constructed by bonding a μF heater/sensor film to an SMA actuator strip with thin soft silicone adhesive in [Aphanuphong, 2008]. As discussed in Section 4.4.5, this process was problematic because the thin silicone adhesive could not be uniformly cured and the alignment between a μF heater/sensor film and an SMA actuator strip was difficult. Therefore an alternative fabrication technique was explored to eliminate the silicone adhesive from the construction process. The alternative fabrication method, called "co-fabrication", was developed and utilized to fabricate the μF actuators for the total of more than twenty prototypes in this dissertation as well as for other research projects built based on the μF technology.

The co-fabrication method utilizes the μF heater/sensor film, which is fabricated directly on a cured polyimide layer on the surface of an SMA sheet, to provide the outline for etching SMA actuators. Therefore both μF heater/sensor films and SMA actuators can be constructed in a single fabrication process. However, in order to utilize the μF film as an SMA actuator outline, several additional layers are required to be built on top of the μF heater/sensor pattern. This chapter discusses the co-fabrication method step by step as illustrated in Figure 5.1, including layer profile, key problems and solutions of each step. Then, the techniques utilized to construct a D-shape skeleton spring and a spine are presented. Finally, the complete μF tip assembly process is described in detail.

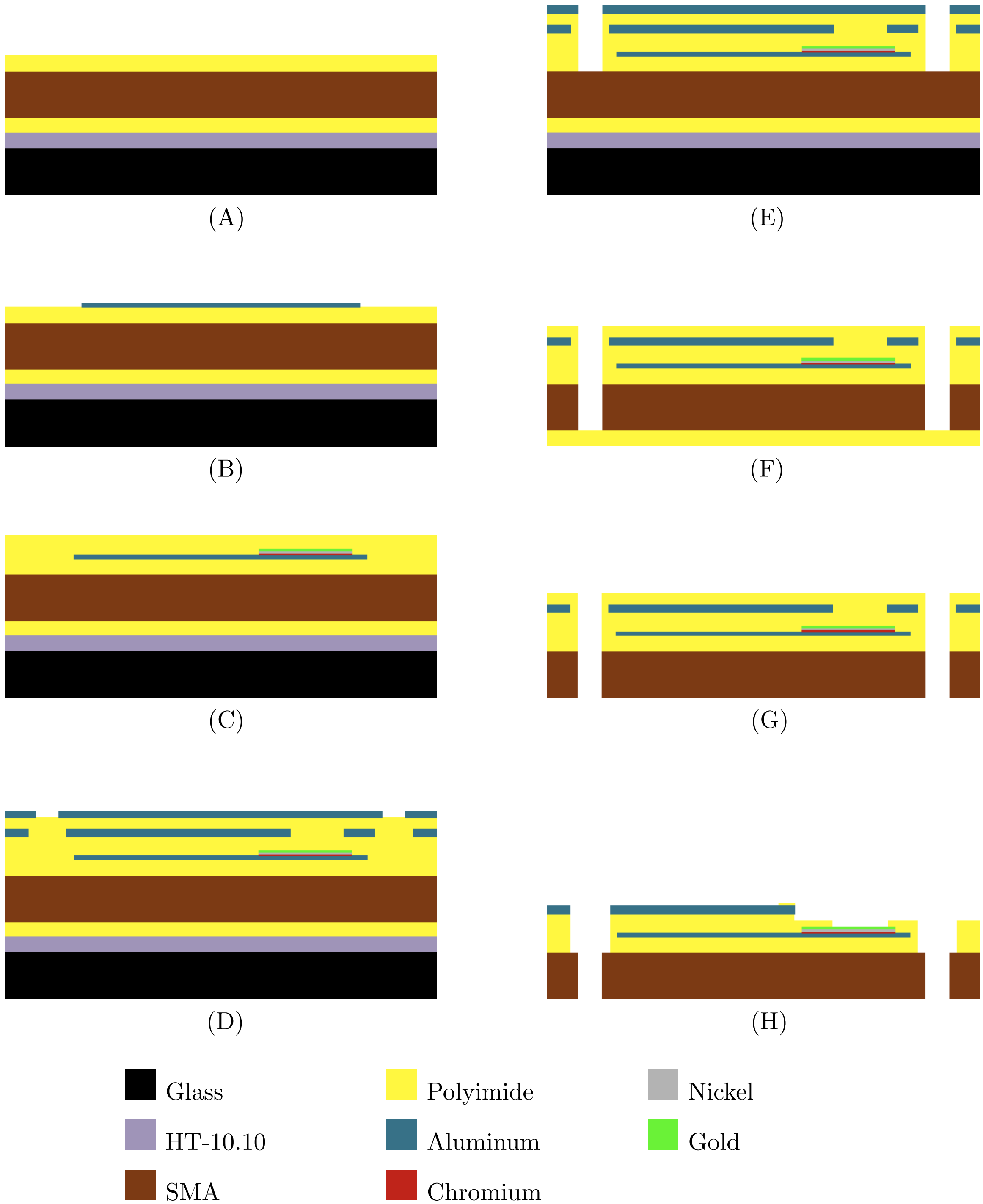

Figure 5.1: Start-to-finish layer profile of the µF actuator fabrication sequence (note: layer thickness is not to scale)

5.1 Substrate Preparation

The co-fabrication method enables the μF heaters/sensors to be built directly on the SMA surface. The thickness of the SMA sheet must be 45μm in order to maximize the μF tip range of motion by balancing forces between SMA actuators and the skeleton spring. However, the available SMA foil has the thickness of 75μm. Thus this foil must be thinned to 45μm using the following process before μF heaters/sensors are fabricated on its surface. The SMA foil is cut into a 2in×3in sheet. This SMA sheet is uniformly thinned to 45μm by immersing in a chemical mixture of hydrofluoric, nitric, and acetic acids (HNA) at the ratio of 1:3:6. The etch rate of an SMA in the HNA is approximately 0.12μm/minute. During the etching process, the SMA sheet is agitated and rinsed with DI water every 10 minutes to prevent the reaction products from accumulating on the SMA surface.

The back side surface of the 45μm thick SMA sheet must be coated with a polyimide layer (PI-2545, from HD-Microsystems) in order to protect this surface during later the SMA electro-etching process, presented in Figure 5.1 (F). Polyimide is selected because it has good dielectric and mechanical properties, strong adhesion, and the fully cured polyimide can withstand most chemical using in the the co-fabrication process. Before the polyimide layer is spun on the SMA surface, the SMA sheet is bonded to a glass slide with double-sided tape to provide a backing support. After the SMA sheet is coated with the polyimide, it is heated on a hotplate at 120° for 3 minutes to vaporize the solvent in the polyimide. Then, this SMA sheet is un-taped from the glass slides and fully cured on a programmable hotplate with the following temperature profile. The sample is placed on a programmable hotplate at room temperature. The hotplate temperature is increased to 200°C at the rate of 240°C/hour. The temperature is held at 200°C for 30 minutes. After that, the temperature is ramped to 250°C at the rate of 200°C/hour and held at 250°C for 1 hour to fully polymerize the polyimide. Finally, the temperature is decreased to room temperature at 200°C/hour to finish the curing process. This thermal curing profile is established to avoid excessively large thermal stress in the cured polyimide and it is utilized to cure every polyimide layer in the μF actuator fabrication.

The SMA sheet with a cured polyimide layer on the back side surface is bonded to a temporary carrier substrate to provide the support during the subsequent fabrication process. Importantly, the SMA sheet must be cleanly released from the carrier substrate after it is subjected to three high temperature polyimide curing cycles. Most temporary bond adhesives are carbonized and permanently bonded to the SMA during this process. However WaferBOND HT-10.10 (from Brewer Science) can hold the SMA sheet flat on the substrate in the polyimide curing process and this SMA sheet can be released from the carrier substrate at the end of the fabrication. The residuals of the HT-10.10 can be dissolved with WaferBOND remover.

To achieve the uniform bond between the SMA sheet and the carrier substrate, HT-10.10 is spun on a cleaned glass slide with the thickness of 25μm. Then the HT-10.10 layer is partially polymerized on a hotplate at 100°C for 2 minutes, and 180°C for 2 minutes. Next, the SMA sheet with coated polyimide layer is laid flat on this glass slide (the cured polyimide layer is placed against the HT.10-10 layer). The sample is then inserted into a custom clamp, and uniformly applied the clamping pressure of 5psi. This clamp is put in a vacuum oven. The oven pressure is reduced to −23inHg and the oven temperature is ramped to 180°C at the rate of 240°C/hour. The temperature is held at 180°C for 15 minutes to establish the bond between the SMA sheet and the glass slide. Finally, the clamp is removed from the oven, and the bonded SMA sheet on the glass slide is carefully released from the clamp. This SMA sheet is ready for the subsequent μF film fabrication process.

Originally, the surface of the SMA sheet bonded to the glass slide was mechanically polished with 1μm diamond grains to provide the smooth and flat surface. During the long polishing period, the SMA was subjected to high shear stress. This high shear stress induced the brittle crystal structure in the SMA leading to cracked SMA actuators when they were bent. A high temperature annealing process could not be conducted on this polished SMA sheet because the polyimide and the HT-10.10 would be burned.

Typically, liquid polyimide trends to flow and level itself during the spin-on process. Hence, instead of polish, the SMA surface roughness is compensated by a thick spun-on polyimide layer. In addition, this polyimide layer is utilized as an insulation layer to prevent short circuits between SMA actuators and metal heaters/sensors. The polyimide layer with the cured thickness of 5μm is deposited on the SMA sheet, and then it is fully cured on a programmable hotplate with the temperature profile described earlier. Figure 5.1 (A) presents the cross section layer profile the SMA substrate, which is ready to fabricate the μF film upon. The black color indicates a temporary carrier substrate (a glass slide). The light magenta color represents the HT-10.10 temporary bond adhesive. Yellow color layers are cured polyimide (PI-2545) with the thickness of 3μm and 5μm on the back and front sides, respectively.

5.2 Aluminum Heater/Sensor Layer

The heater/sensor layer of the μF film is formed by a thin aluminum layer with the thickness of 0.100μm. This aluminum is deposited directly on the cured polyimide layer of the SMA substrate by using a DC magnetron sputtering system. Then this sputtered aluminum layer is patterned by using a wet-etching process.

The key problem of this fabrication step is the delamination of the sputtered aluminum from the cured polyimide due to their poor adhesion. However the adhesion between both layers can be improved by dry-etching the polyimide surface in an oxygen plasma for 1 minute before the aluminum deposition. Then the whole polyimide layer on the SMA surface is deposited with a 0.001μm thick sputtered aluminum layer using a DC magnetron sputtering system in an argon environment at the pressure of 5×10^{-3} Torr and the sputtering power of 120W. The desired heater/sensor pattern is formed on the aluminum surface using a 1μm thick positive photoresist layer. Then the sample is immersed in an aluminum etchant at 40°C to etch the unwanted aluminum area. The etch rate of the aluminum is approximately 8nm/second. Finally, the positive photoresist is dissolved with acetone and rinsed with isopropanol alcohol (IPA) to achieve a clean aluminum heater/sensor pattern.

Figure 5.1 (B) illustrates the cross section profile of the μF actuator after the aluminum layer is deposited. The dark green layer represents aluminum with the thickness of 0.100μm. Figure 5.2 shows the patterned aluminum layer with the μF film design [D]. The yellow area is the polyimide layer on the SMA surface. The dark blue area is the aluminum heaters/sensors. The light blue dashed box is the parallel heater/sensor (R_p). The orange dashed box is the orthogonal heater/sensor (R_o). The width of the heater/sensor traces is 20μm and the spacing between traces is 10μm.

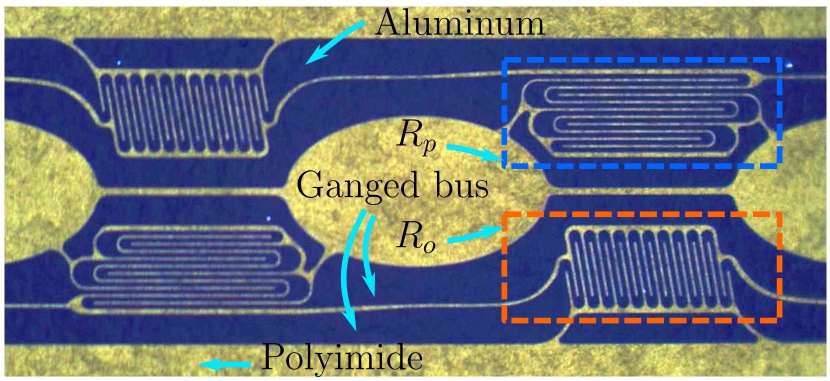

Figure 5.2: Fabricated aluminum heaters/sensors with the μF film design [D]

5.3 Pad and Polyimide Encapsulation Layer

Soldering is the selected method to connect copper signal interfacing wires to terminal pads on μF actuator because it provides good electrical connection and strong mechanical support. However, typical Sn-based solder cannot alloy with aluminum to establish the bonding and electrical connection. Multi-metal layer terminal pads, consisting of chromium, copper, and gold, are utilized in [Aphanuphong, 2008]. When the solder is melted on this pad structure, it rapidly scavenges the gold and copper layers to establish electrical and mechanical connections. Hence a thick copper layer is required to provide reliable connections. A thick sputtered copper layer is brittle and can be broken under small bending strain, resulting in open electrical connections between the external circuit and the μF heaters/sensors.

An alternative pad structure is investigated in this co-fabrication process to increase the reliability of the connections but reduce the fabrication time. The new pad structure must be thin, and strong, but not brittle. In addition, it must have good electrical and mechanical interconnections. Nickel is an alternative metal investigated in this fabrication because it can be soldered to with Sn-base solder paste. Its scavenging rate is also much lower than the copper, thus only a thin nickel layer is required. Thermal evaporation of nickel is also compatible with the μF film fabrication process.

These terminal pads are constructed on the aluminum heater/sensor layer by forming the pad lift-off pattern on the substrate using a negative photoresist with an undercut sidewall profile. The undercut profile is required to break the metal film deposited on the substrate and photoresist. The thickness of the negative photoresist is approximately 2.5μm. The undercut negative photoresist is cleaned in O_2 plasma for 15 seconds before the pad deposition process to ensure that all residuals are removed. Then, a thin chromium adhesion layer is deposited on the aluminum with the thickness of 0.005-0.010μm using a DC magnetron sputtering system. Then a nickel layer is thermally evaporated on the chromium with the thickness of 0.200μm. After that a thin layer of gold is thermally evaporated on the nickel with the thickness of 0.050-0.100μm. This gold layer is utilized to protect the nickel layer from oxidizing during the high temperature polyimide curing process. Then the sample is immersed in acetone to dissolve the photoresist to achieve clean pad patterns. Finally, a polyimide layer with the cured thickness of 1.5μm is spun on the whole sample surface and cured. This polyimide is employed to protect the aluminum heaters/sensors. However, the polyimide covering on the pads will be removed at the end of the fabrication to allow copper signal interfacing wires to be soldered.

Figure 5.1 (C) presents the cross section profile of the μF actuator that has this pad structure and a polyimide encapsulation covering the whole surface. The red, gray, and green are chromium, nickel, and gold layers, respectively.

5.4 Pad Window and SMA Groove Outline Masks

At this point, all required layers of μF heaters/sensors are fabricated. Additional layers are to enable the μF film to be utilized as a mask for patterning the SMA actuator. Two aluminum layers with each layer thickness of 0.200μm and a polyimide layer with the cured thickness of 1.5μm are constructed in this fabrication step. Both aluminum layers are deposited and patterned using the same method as the aluminum heater/sensor fabrication. The first aluminum layer from the top in Figure 5.1 (D) is to protect the heater/sensor pattern during the SMA grooved dry-etching process. The second aluminum layer is to shield the heaters/sensors during the pad window dry-etching process. These windows must be opened in order to allow the heaters/sensors to interface with an external sensing circuit. Aluminum is a selected material to fabricate these masks instead of polymer (e.g. photoresist etc.) because both dry-etching processes require masks that can withstand long plasma etching. In addition, aluminum is easy to deposit and pattern and it is compatible with the co-fabrication process since it has already been used as the heater/sensor material.

Figure 5.1 (D) is the cross section profile of the μF actuator after both aluminum masks are deposited and patterned. Two additional dark green layers from step (C) are the aluminum RIE protection masks. The top aluminum layer contains the SMA outline, which has narrow groove pattern. This aluminum layer preserves the heaters/sensors during a long polyimide dry-etching process. The bottom aluminum layer has pad and center welding tab window patterns, which are small rectangle and ellipse holes on top of the heater/sensor terminal pads and center welding tabs, respectively. The polyimide layer in between both aluminum layers is utilized to protect the μF film structure during the SMA electro-etching process. The detail of the process is discussed in Section 5.6. Figure 5.3 shows the bottom aluminum pattern. The dark blue area is the aluminum using to protect the μF film in the dry-etching process. This aluminum covers most of the μF film pattern except at pad windows, center and side welding tab areas, and the SMA groove outline. These opening areas allow the ionized plasma in the dry-etching process to remove the polyimide on the SMA surface.

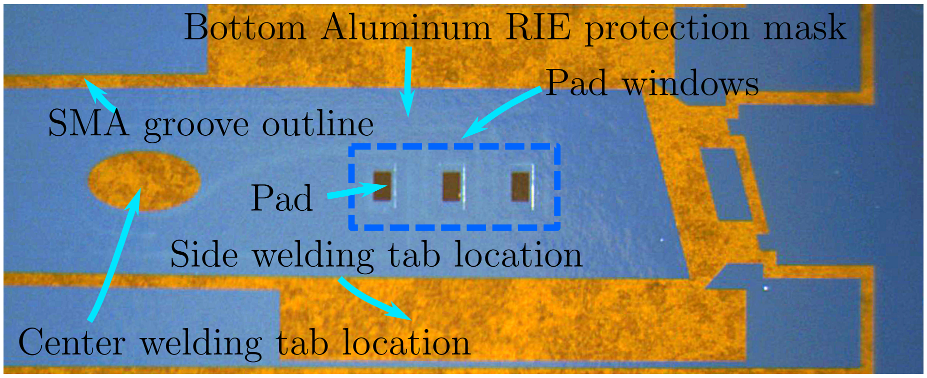

Figure 5.3: A μF actuator sample after the bottom aluminum layer is deposited and patterned

5.5 SMA Groove Outline Patterning with a Dry-Etching Process

The SMA actuator groove outline is still filled with cured polyimide. This polyimide must be removed before the SMA can be patterned with the electro-etching process. Typically, fully cured polyimide has excellent chemical resistance properties, thus it is not possible to wet-etch the cured polyimide without destroying the heaters/sensors. The only method to pattern the fully cured polyimide, which is also compatible with the co-fabrication process, is to dry-etch with ionized plasma. However, there are two important issues must overcome in the polyimide dry-etching process: polymer grass, and carbonization. Polymer grass is formed when the polyimide is not uniformly etched due to the redeposition of residuals on the polyimide surface. These residuals act as micro masks to block the ionized plasma from etching polyimide in those areas, leaving tall grass-like structures. These polyimide structures cannot be easily removed without destroying the μF film. However, polyimide grass can be avoided by utilizing a suitable gas mixture, low pressure, and low etching power during the dry-etching process. On the other hand, carbonization occurs when the polyimide is dry-etched for a long time causing the sample to be overheated and the polyimide to be burned,leaving black residuals over the sample surface. This issue can be averted by dry-etching the polyimide in multiple short periods to allow the sample to cool down.

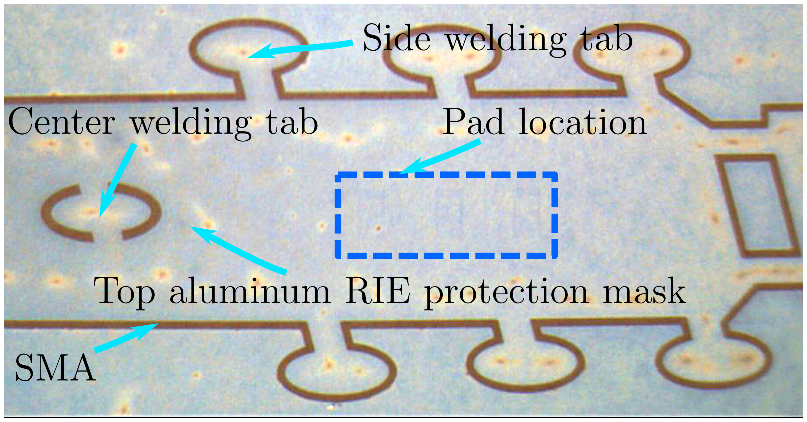

Figure 5.4: A μF actuator, which is covered with the top aluminum layer, after the polyimide in the groove outline is cleanly etched

To avoid both issues in the dry-etching process, the polyimide is dry-etched in the ionized plasma with the mixture of $CF_4 : O_2$ at the ratio of 10%:90%, the pressure of 50×10^{-3} Torr and the etching power of 100W. In addition, the dry-etching process is stopped for 10 minutes in every 15 minutes of the etching period to prevent the sample from overheating. The etch rate of polyimide with these process parameters is approximately 0.100μm/minute. When the polyimide inside the groove is cleanly removed, the SMA sheet is released from the glass carrier substrate by heating the sample to 180°C to liquify the HT-10.10 bond. Then the SMA is carefully slid off the carrier substrate. The residuals of HT-10.10 on the back side of the SMA sheet are dissolved with WaferBOND remover and rinsed with IPA.

Figure 5.1 (E) is the cross section profile of the μF actuator after the cured polyimide inside the grooves is etched away to expose the SMA surface underneath. It is important that the exposed SMA surface must be clean without any residuals because any residual can prevent the SMA from contacting with the electrolyte in the electro-etching process causing the SMA actuators to be non-uniformly etched. In addition, the bottom aluminum mask must be protected inside the polyimide to prevent the aluminum from being etched away in the electro-etch process. Figure 5.4 shows the μF actuator sample after the polyimide in the grooves is removed. The top aluminum mask is slightly etched in the dry-etching process. The SMA surface in the groove outline is cleanly exposed without any remaining residuals.

5.6 SMA Actuator Patterning with an Electro-Etching Process

Typically, most metals can be etched in a mixture of acids or bases (etchants). As previously described, SMA can be etched in HNA, but HNA is able to diffuse through photoresist and polyimide and then etch the aluminum inside µF films. In addition, HNA can release µF films from the SMA surface. Hence, HNA is not suitable to use as an SMA etchant in the co-fabrication process.

As discussed in Section 2.2 in [Aphanuphong, 2008], SMA can be etched using an electro-etching process. This electro-etching process utilizes lithium chloride in ethanol as its electrolyte, which does not attach the µF film. Originally, the uniformity of the etched pattern is poor, causing the actuator pattern to be overetched in some areas. In th co-fabrication process, the electro-etching process is modified to improve the uniformity and smoothness of the etched pattern. The uniform and smooth SMA pattern is achieved in the electro-etching process when the SMA is connected at the cathode (positive polarity of the power supply) and a large stainless steel plate, which is wider than the side of the SMA sample, is connected at the anode (negative polarity of the power supply). This large stainless steel plate enables the etching current to uniformly flow from cathode to anode. The concentration of the LiCl electrolyte is 1 mol/liter. The spacing between cathode and anode is set at two inches and 8V DC voltage is applied between them. The uniformity of the etched pattern is increased when a stirrer is set at the center of the sample in between the cathode and anode. The stirrer is utilized to flush the electro-chemical reaction products out of the grooves, to allow the SMA to constantly expose to the electrolyte.

One important limitation of the electro-etching process is that it cannot be used to etch large areas because the uniform current density in those areas is difficult to control. Therefore the SMA actuator pattern must be outlined in narrow grooves and the back side surface of the SMA sheet must be sealed with a cured polyimide layer to focus the current density in those grooves at the front side of the SMA. Theoretically, the lithium chloride in ethanol electrolyte is a mid salt and it cannot etch aluminum. However, the top aluminum mask is also slowly etched away during the electro-etching process. Therefore, it is important to completely encapsulate the rest of the μF film in the polyimide to prevent them from being etched. Figure 5.1 (F) illustrates the cross section profile of the μF actuator after the SMA inside the groove is etched through leaving the smooth and uniform SMA actuator pattern.

5.7 Back Side Polyimide and Pad Windows Etching with a Dry-Etching Process

Electrical current must be able to flow through the welding tabs and the skeleton spring where both surfaces are welded by using a resistive welding process. Therefore the polyimide on the back side surface of the SMA actuator, where the actuator strip contacted with the spring, must be removed. This polyimide layer can be removed using a dry-etching process with the same process parameters presented in Section 5.5. The SMA actuator pattern is flipped over to expose the polyimide on the back side surface to the ionized plasma in the dry-etching process. The sample is laid flat on a clean glass substrate with Kapton tape to seal around the edges of the sample (the μF film is placed against the glass surface). Then the polyimide is dry-etched to expose the SMA surface. Figure 5.1 (G) shows the cross section profile of the μF actuator after the back side surface polyimide is removed.

The pads on the front side of the μF actuator are still buried in the polyimide layer. This polyimide must be dry-etched to expose pads, which allow copper interfacing wires to connect to the μF heaters/sensors. However, before the polyimide can be dry-etched, the remaining top aluminum mask must be removed by immersing it in an aluminum etchant and then rinsing with DI water. In addition, this dry-etching process must stop before the ionized plasma etches through the polyimide to expose metal pads to etch the bottom aluminum mask around the pad windows. This bottom aluminum mask must be etched to prevent short circuits between copper wires. Then the polyimide is continuously etched until metal pads and the welding tabs are cleanly exposed without any residual to enable strong solder and mechanical connections.

Figure 5.1 (H) presents the cross section profile of the finished μF actuator, which is ready for subsequent assembly process. Figure 5.5 presents the finished μF actuator pattern, which has the bottom aluminum layer covering the heaters/sensors. This μF actuator is ready to be welded to a skeleton spring.

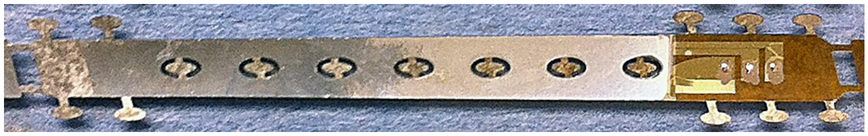

Figure 5.5: A single completely fabricated μF actuator strip

5.8 Skeleton Spring and Spine Fabrication

The skeleton spring is the core structure of the μF tip, which holds the μF actuator, and the spine and provides bias forces to compress the μF actuator. This spring is formed by winding a superelastic wire around a D-shaped mandrel. The superelastic wire is tightly clamped around its circumference during the high temperature shape-setting process in a furnace at 500°C for 15 minutes. Then, the mandrel is rapidly cooled to room temperature with nitrogen. The superelastic wire is released from the mandrel resulting in a D-shape spring covered with a thick oxide layer from the high temperature process. This thick oxide is removed by immersing the spring in HNA for 5 minutes to allow the μF actuator to be welded on. A superelastic (nickel-titanium, NiTi) is selected as the skeleton spring material rather than a precipitation-hardening steel (as in Aphanuphong [2008]) because it allows SMA actuator strips to be welded on the spring without the formation of intermetallics, that results in brittle weld spots.

The spine is another key element of the μF tip. It is used to prevent the skeleton from compressing or extending on one side, while allowing the spring at that point to tip and tilt as the SMA actuator segments to extend or contract. In addition, the spine has integrated alignment marks used to precisely and repeatedly align the μF actuator on the skeleton spring. The spine is made from an SMA foil. It shares the substrate preparation and the SMA etching process with the μF actuator fabrication, except there is only one cured polyimide layer on the front side of the SMA. The polyimide layer contains the spine outline pattern. A photodefinable polyimide (PI-2723) is utilized instead of the non-photodefinable (PI-2545) to pattern the spine outline to simplify the fabrication process.

5.9 μF Tip Assembly Process

A μF actuator, a skeleton spring, and a spine are assembled to a μF tip by hand under a microscope. The skeleton spring is clamped on a custom fixture to stretch and adjust the spacing between each spring turn to match with the segment spacing of the spine with the flat section of the D-shape spring point upward. All the welding tabs on the spine are preformed on a separate custom jig such that they can wrap around the spring wire. The spine is aligned on the skeleton spring at the middle of the flat section of the D-shape spring. Then all welding tabs and μF actuator alignment marks are spot welded on the spring with custom micro welding tongs. Then the skeleton spring is released from the fixture, flipped over and clamped back on the fixture to attach the μF actuator strip. The center and side welding tabs on the μF actuator are also preformed as in the spine. Then all actuator segments, where heaters/sensors are located, are carefully bent down (heaters/sensors facing upward). The slight bent sections lead actuator segments to smoothly bend into the skeleton spring when they are compressed. The pre-formed μF SMA actuator strip is aligned on the skeleton using alignment features provided from the spine. Then all center and side welding tabs are welded on the spring. The skeleton spring is released from the assembly fixture and copper wires are soldered on the heater/sensor pads. The μF tip is completely assembled and it is ready to utilize in subsequent experiments to investigate impacts of each μF film designed described in Chapter 4.

The μF actuator co-fabrication process, including key issues and solutions in every step, is presented in this Chapter. This method is able to simplify the μF actuator construction by combining the μF film and the SMA actuator construction in a single fabrication process. In addition, it also improves the reliability of the μF tips by enabling the μF actuators to be strongly and precisely attached on the skeleton springs. These μF tip prototypes are utilized in many

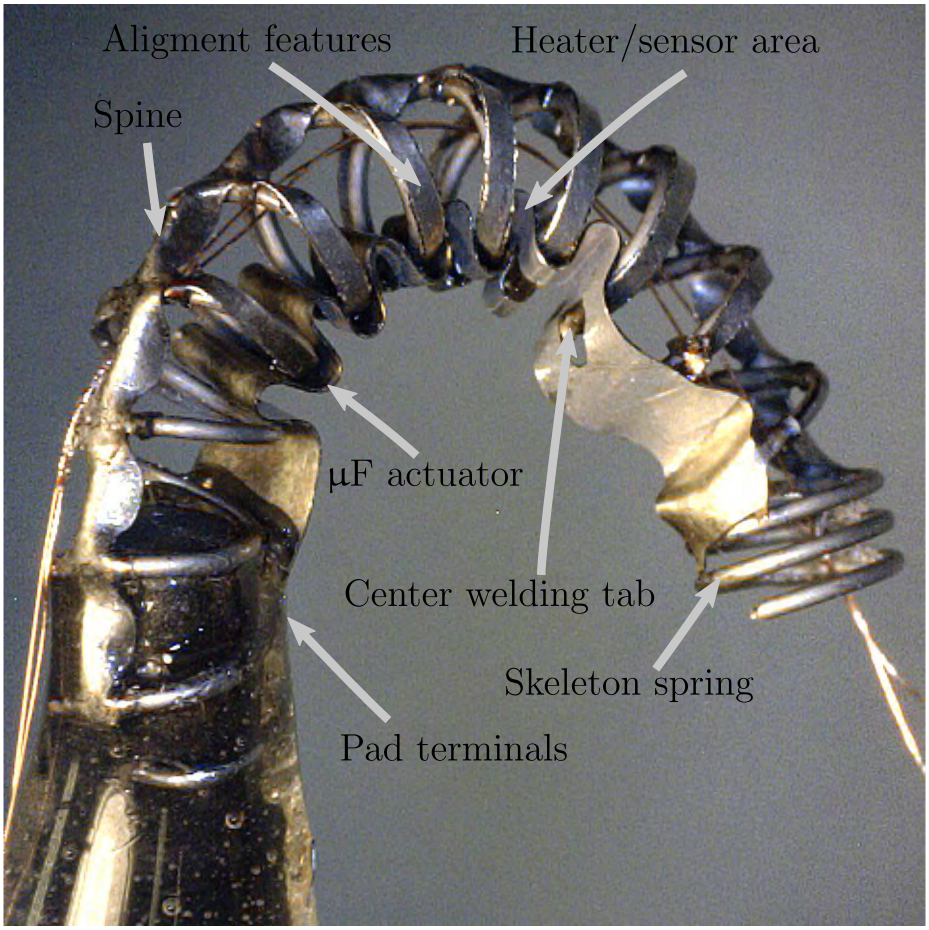

Figure 5.6: A complete μF tip

experiments described in this dissertation and other research projects based on the μF technology without any mechanical or μF actuator failure. This co-fabrication process shows a strong potential for the revolutionize of the μF tip construction.

Chapter 6

Conclusion

6.1 Summary

A μF tip prototype for each of the μF film design was fully assembled, analyzed, and utilized to study how each μF film design can impact the dynamics of the temperature and strain measurement of the μF tip. The understanding from this study was utilized to improve the overall μF film design and sensing performance in each design iteration. This μF film had two main functions: heaters to modulate the amount of heat to actuate the μF SMA actuator and sensors to measure the strain and temperature of the actuator. The concurrent heating and sensing functions on the μF film were measured with the modified Wheatstone bridge in the signal conditioning circuit. This μF film was designed as a multilayer thin film structure that could be fabricated by using an innovative fabrication process, called "co-fabrication", developed in this dissertation. Co-fabrication enabled the μF film to be fabricated directly on the SMA foil and utilized as an actuator outline mask to protect the foil during SMA etching.

The final μF film design consisted of only one layer of amorphous (sputtered) aluminum heater/sensor layer encapsulated in polyimide. This aluminum contains two distinct meandering patterns, which function as resistors connected in series, to heat the SMA actuator by using a Joule-heating method. The temperature and strain measurements of the μF film were provided from the resistance change of both meandering patterns due to the expansion or contraction of their geometry. Amorphous aluminum was utilized in the μF film because it provided a low Young's modulus, and a high ultimate tensile strength, which were advantageous in the high-strain operation of the μF film design.

Two distinct meandering patterns (parallel and orthogonal designs) on the aluminum layer were arranged in such a way that they alternated from one actuator segment to the next, and were pairwise symmetric along the longitudinal axis of the actuator strip. Their maximum strain sensitivity axis was approximately 90° apart. In addition, the actuator areas underneath both meandering patterns were approximately matched to provide similar thermal masses and thermal paths. The experiment results indicated that the μF film provided excellent performance in both temperature and strain sensing. This performance was achieved through the μF film design derived from an integrated understanding of how the elements in the μF tip, including control algorithms and fabrication techniques, were correlated.

6.2 Contributions

6.2.1 Elimination of False Measurements from the μF films

The electro-thermo-mechanical model of the the μF film was developed to analyze the impact of the orthogonal and parallel designs in the modified Wheatstone bridge in the signal conditioning circuit. The analysis result in Section 4.7 indicated that false strain extracted from $\frac{V_s}{V_h}$ and $\frac{V_t}{V_h}$ could be eliminated by matching the dynamics of both $\frac{V_s}{V_h}$ and $\frac{V_t}{V_h}$. This dynamic similarity in $\frac{V_s}{V_h}$ and $\frac{V_t}{V_h}$ was achieved by rearranging the parallel and orthogonal heaters/sensors such that they had similar thermal masses and thermal paths. This understanding led to the current μF film design, which had only one aluminum layer to match the top and bottom thermal paths, and the parallel and orthogonal heaters/sensors are alternately positioned along the longitudinal axis of the actuator strip. The experiment results in Figure 4.25 show that both false strain and false temperature in measured this μF film design were acceptably small. This understanding could be used to remove dynamical mismatch in other similar micro actuation schemes.

6.2.2 Design Constraints to Ensure Minimum Phase in the μF Tip Control Plants

The non-minimum phase dynamics in the position control plant prevented good close-loop position control. This work found a way to ensure minimum phase temperature and position control plants. The analysis in Section 4.7.4 indicated that minimum phase could be achieved from the stable, minimum phase $\frac{V_s}{V_h}$ and $\frac{V_t}{V_h}$ paths, if they had similar dynamics. Section 4.7 demonstrated an example of the μF film design, which such dynamic similarity. In addition, it was shown that the dynamic similarity of $\frac{V_s}{V_h}$ and $\frac{V_t}{V_h}$ paths was necessary to eliminate false temperature and strain measurements in the μF film.

6.2.3 Simplification of the μF Actuator Fabrication Process

The μF actuator was composed of two main elements: an SMA actuator and a μF film. The SMA patterning process in this dissertation was simplified by utilizing the μF film as a mask to protect the SMA during the patterning process. One polyimide and two aluminum layers had to be added on the μF film to enable this co-fabrication process. The first aluminum was to provide the groove outline of the SMA actuator pattern. The second aluminum layer was to protect the μF film during pad window opening process. The polyimide between the first and the second aluminum layers had to completely seal around edges of the second aluminum layer to prevent it from being etched during patterning of the SMA. This fabrication process significantly improved the alignment quality between the μF film and the SMA actuator and also reduced the complexity of the μF actuator construction.

The original electro-etching process in [Aphanuphong, 2008] could not produce smooth edge SMA patterns because the SMA was not uniformly etched. In this dissertation, this electro-etching process was optimized to increase the uniformity by constantly flushing the SMA patterns to remove the reaction products inside the grooves, and increasing the size of the stainless steel electrode on the anode to raise the uniformity of the etching current.

A plasma dry-etching process was utilized to etch the SMA groove outline in the μF film polyimide layer. It was important that the SMA surface inside the grooves had to be completely clean in order to achieve smooth edges of the SMA patterns. Two difficulties in dry-etching the polyimide were polymer grass and carbonized polyimide. Polymer grass formed on the polyimide surface when redeposited polymer residuals acted as a micro mask to prevent the ionized plasma from uniformly etching the polyimide, resulting tall grass-like polyimide structures on the SMA surface. Carbonized polyimide formed on the SMA surface when polyimide was overheated due to a long dry-etching period. These grass-like structures and carbonized polyimide could not be removed without destroying the μF film. However, the dry-etching process presented in Section 5.5 could etch the polyimide layer without polymer grass and carbonization on the SMA surface by modifying gas combination ratio, reducing pressure and power, and dividing a long etch period into multiple short etch periods.

6.3 Conclusion

Four different μF film designs are constructed and presented in this dissertation. The understanding accumulated from each design is utilized to construct dynamic electro-thermo-mechanical (ETM) models, which can be employed to predict the dynamical responses of the $\frac{V_s}{V_h}$ and $\frac{V_t}{V_h}$ signals. Surprisingly, the analysis results suggest that small dynamic differences due to the orthogonal and parallel heaters/sensor configuration can cause large dynamic mismatches between the $\frac{V_s}{V_h}$ and $\frac{V_t}{V_h}$, which cannot be captured by the static ETM models. It turns out that both orthogonal and parallel heaters/sensors must be symmetrical in order to eliminate their dynamic differences. The μF film design [D] is designed and constructed based on this principle. The false strain due to temperature measured from this μF film design is less than 5% of the full scale strain, which indicates excellent performance in the strain sensing functionality.

Non-minimum phase dynamics of the position control plant model are also another unexpected issue discovered in the μF actuators. The source of this issue turns out to be due to the combination of the dynamical differences between the orthogonal and parallel heaters/sensors and the temperature-strain calibration method. This problem can also be fixed by matching the dynamical properties of both heaters/sensors.

The principles discovered from these studies indicates that, at this scale, the dynamical differences are sensitive to the heater/sensor layout patterns. To achieve excellent performance in both temperature and strain sensing, the orthogonal and parallel elements must have nearly identical dynamical responses. This knowledge also can be applied to other micro actuators which require temperature and strain sensing functionality.

The co-fabrication technique, which allows sensors, actuators, and structure patterning to be fabricated in single construction process, is another important development of this dissertation. It eliminates silicone adhesive in the construction by fabricating the sensor film directly on the actuators. The sensor films also can be precisely aligned on the actuators. In addition, this technique can reduce the complexity in the construction and assembly by integrating the actuator patterns into the sensor films and utilizing them in the actuator fabrication. The application of the co-fabrication technique is not limited to only the μF actuators, but the fundamentals of this technique can be applied to other micro actuator constructions, which require sensors to be integrated on the micro actuators. It opens a new direction in micro actuator design and construction.

6.4 Future Work

The experiment results in this dissertation indicate that the μF film has good performance in both temperature and strain sensing for the existing application. Hence, this μF tip design is ready for further development. In particular for force feedback teleoperation, we need to further understand the relationship between the position error from the closed-loop position feedback control and the reaction force at the tip. For reusable medical devices, the strength, stability, and fatigue endurance of amorphous aluminum films must be better understood. For smaller μF device designs, a method to reduce the SMA surface roughness should be explored to reduce the need for a thick polyimide leveling layer. In the signal conditioning circuit, it would be interesting to understand why the input impedances of the differential amplifiers must be matched in order to eliminate phase differences between outputs, or if other instrumentation amplifiers suffer from this problem.

Bibliography

S. Aphanuphong. Embedded heaters and sensors for micro SMA actuators. Master's thesis, Department of Aerospace Engineering Sciences, University of Colorado at Boulder, Aug 2008.

K. Arai, S. Aramaki, and K. Yanagisawa. Feedback linearization for SMA (Shape Memory Alloy). In The Society of Instrument and Control Engineers 1995, (SICE '95), Proceedings of the 34th SICE Annual Conference, International Session Papers, pages 1383–1386, Hokkaido, Japan, 1995.

S. Aramaki, S. Kaneko, K. Arai, Y. Takahashi, H. Adachi, and K. Yanagisawa. Tube type micro manipulator using shape memory alloy (SMA). In Micro Machine and Human Science 1995, (MHS '95), Proceedings of the 6^{th} International Symposium on, pages 115–120, Nagoya, Japan, 1995.

Jumpei Arata, Mamoru Mitsuishi, Shinichi Warisawa, Katsuya Tanaka, Takashi Yoshizawa, and Makoto Hashizume. Development of a Dexterous Minimally-Invasive Surgical System with Augmented Force Feedback Capability. Intelligent Robots and Systems, 2005. (IROS 2005). 2005 IEEE/RSJ International Conference on, pages 3207–3212, 2005.

M. Chinmulgund, R. B. Inturi, and J. A. Barnard. Effect of ar gas pressure on growth, structure, and mechanical properties of sputtered Ti, Al, $TiAl$, and Ti_3Al films. Thin Solid Films, 270 (1-2):260–263, 1995.

Javad Dargahi and Siamak Najarian. An Integrated Force-position Tactile Sensor for Improving Diagnostic and Therapeutic Endoscopic Surgery. Bio-Medical Materials and Engineering, 14(2): 151–166, 2004.

P. Dario, R. Valleggi, M. Pardini, and A. Sabatini. A miniature device for medical intracavitary intervention. In Micro Electro Mechanical Systems 1991, (MEMS '91), Proceedings of the IEEE An Investigation of Micro Structures, Sensors, Actuators, Machines and Robots, pages 171–175, Nara, Japan, 1991.

P. Dario, C. Paggetti, N. Troisfontaine, E. Papa, T. Ciucci, M. C. Carrozza, and M. Marcacci. A miniature steerable end-effector for application in an integrated system for computer-assisted arthroscopy. In Robotics and Automation, Proceedings of the 1997 IEEE International Conference on, volume 2, pages 1573–1579, Albuquerque, NM, USA, 1997.

C. A. Dickinson and J. T. Wen. Feedback control using shape memory alloy actuators. Intelligent Material Systems and Structures, Journal of, 9(4):242–250, 1998.

C. A. Dickinson, D. C. Hughes, and J. T. Wen. Hysteresis in shape memory alloy actuators: the control issues. Smart Structures and Materials 1996: Mathematics and Control in Smart Structures, 2715(1):494–506, 1996.

M. H. Elahinia and H. Ashrafiuon. Nonlinear control of a shape memory alloy actuated manipulator. Vibration and Acoustics, Journal of, 124(4):566–575, 2002.

J Engel, J Chen, and C Liu. Strain Sensitivity Enhancement of Thin Metal Film Strain Gauges on Polymer Microscale Structures. Applied Physics Letters, 89(22), 2006.

Y. Fu, X. Li, H. Liu, Z. Liang, and X. Ma. Kinematics of micro bending robot using shape memory alloy for active catheter. In Robotics and Biomimetics 2006, (ROBIO '06), Proceeding of the IEEE International Conference on, pages 1594–1599, Kunming, China, 2006.

T. Fukuda, S. Guo, K. Kosuge, F. Arai, M. Negoro, and K. Nakabayashi. Micro active catheter system with multi degrees of freedom. In Robotics and Automation 1994, Proceedings of the 1994 IEEE International Conference on, pages 2290–2295, San Diego, CA, USA, 1994.

A Garcia-Alonso, J Garcia, E Castano, and F J Gracia. Strain Sensitivity and Temperature Influence on Sputtered Thin Films for Piezoresistive Sensors. Sensors and Actuators A: Physical, 37-38:784–789, 1993.

R. B. Gorbet and K. A. Morris. Closed-loop position control of preisach hystereses. Intelligent Material Systems and Structures, Journal of, 14(8):483–495, 2003.

R. B. Gorbet and R. A. Russell. A novel differential shape memory alloy actuator for position control. Robotica, 13:423–430, 1995.

D. Grant and V. Hayward. Controller for a high strain shape memory alloy actuator: quenching of limit cycles. In Robotics and Automation 1997, Proceedings of the 1997 IEEE International Conference on, volume 1, pages 254–259, Albuquerque, NM, USA, 1997a.

D. Grant and V. Hayward. Variable structure control of shape memory alloy actuators. Control Systems Magazine, IEEE, 17(3):80–88, 1997b.

D. Grant and V. Hayward. Constrained force control of shape memory alloy actuators. In Robotics and Automation 2000, (ICRA '00), Proceedings of the IEEE International Conference on, volume 2, pages 1314–1320 vol.2, San Francisco, CA, USA, 2000.

H P Grant, J S Przybyszewski, W L Anderson, and R G Claing. Thin Film Strain Gage Development Program. Technical report, NASA John H. Glenn Research Center at Lewis Field Cleveland, Ohio, Handnover, MD, USA, 1983.

Y. Haga, Y. Tanahashi, and M. Esashi. Small diameter active catheter using shape memory alloy. In Micro Electro Mechanical Systems, 1998, (MEMS '98), Proceedings of the 11^{th} Annual International Workshop on, pages 419–424, Heidelberg, Germany, 1998.

Y. Haga, T. Mineta, and M. Esashi. Multi-functional active catheter. Sensors Update, 8(1):147–186, 2001.

Y. Haga, M. Mizushima, T. Matsunaga, K. Totsu, and M. Esashi. Active bending ileus tube using shape memory alloy for treatment of intestinal obstruction. In Microtechnology in Medicine and Biology 2005, Proceedings of the 3rd IEEE/EMBS Special Topic Conference on, pages 249–252, Oahu, HI, USA, 2005.

P. M. Hall. The effect of expansion mismatch on temperature coefficient of resistance of thin films. Applied Physics Letters, 12(6):212–212, 1968.

T. Hasegawa and S. Majima. A control system to compensate the hysteresis by preisach model on SMA actuator. In Micromechatronics and Human Science 1998, (MHS '98), Proceedgins of the 1998 International Symposium on, pages 171–176, Nagoya, Japan, 1998.

Neville Hongan. Impedance Control: An Approach to Manipulation: Part -Theory, Part -Implementation, Part -Applcation. Journal of Dynamic Systems, Measurement, and Control, 171:1–24, 1985.

Mark Horowitz and Robert W Dutton. Resistance Extraction from Mask Layout Data. Computer-Aided Design of Integrated Circuits and Systems, IEEE Transactions on, 2(3):145–150, 1983.

K. Ikuta. Micro/miniature shape memory alloy actuator. In Robotics and Automation 1990, Proceedings of the 1990 IEEE International Conference on, pages 2156–2161, Cincinnati, OH, USA, 1990.

K. Ikuta, M. Tsukamoto, and S. Hirose. Shape memory alloy servo actuator system with electric resistance feedback and application for active endoscope. In Robotics and Automation, Proceedings of the 1988 IEEE International Conference on, volume 1, pages 427–430, Philadelphia, PA, USA, 1988.

S.W. James, M. L. Dockney, and R. P. Tatam. Simultaneous Independent Temperature and Strain Measurement Using In-Fibre Bragg Grating Sensors. Electronics Letters, 32(12):1133–1134, 1996.

Y. Kai and G. Chengin. Design and control of novel embedded sma actuators. Electrical & Electronics Engineering, Journal of, 2(2):513–520, 2002.

S. Kaneko, S. Aramaki, K. Arai, Y. Takahashi, H. Adachi, and K. Yanagisawa. Multi-freedom tube type manipulator with SMA plate. Intelligent Material Systems and Structures, Journal of, 7(3): 331–335, 1996.

N. B. Kha and K. K. Ahn. Position control of shape memory alloy actuators by using self tuning fuzzy pid controller. In Industrial Electronics and Applications 2006, The 1^{st} IEEE Conference on, pages 1–5, Singapore, 2006.

Won S. Kim. Developments of New Force Reflecting Control Schemes and an Application to a Teleoperation Training Simulator. In Robotics and Automation, 1992. Proceedings., 1992 IEEE International Conference on, volume 2, pages 1412–1419, Nice, France, 1992.

A. B. Koolwal, Byong Ho Park, B. Nelson, G. Niemeyer, and D. H. Liang. Amplitude-modulating switching feedback for position control of shape memory alloy actuators. In Biomedical Robotics and Biomechatronics 2006, (BioRob 2006), Proceeding of the First IEEE/RAS-EMBS International Conference on, pages 847–852, Pisa, Italy, 2006.

K. Kuribayashi. Improvement of the response of an SMA actuator using a temperature sensor. Robotics Research, The International Journal of, 10(1):13–20, 1991.

Gwo-Bin Lee, Fu-Chun Huang, Chia-Yen Lee, and Jiun-Jih Miau. A New Fabrication Process for a Flexible Skin with Temperature Sensor Array and Its Applications. Acta Mechanica Sinica, 20 (2):140–145, 2004.

H. J. Lee, J. J. Lee, and D. S. Kwon. Position control of an SMA actuator using sliding mode control with time delay estimation. International Journal of Assistive Robotics and Mechatronics, International Journal of Human-friendly Welfare Robotic Systems, 4(2):51–56, 2003.

K. F. Lei, Y. Yam, and P. Baranyi. Neural-fuzzy based control experiments on a shape memory alloy (SMA) positioning system. In American Control Conference, Proceedings of the 2001, volume 5, pages 3861–3865, Arlington, VA, USA, 2001.

Daniel J Lichtenwalner, Aaron E Hydrick, and Angus I Kingon. Flexible Thin Film Temperature and Strain Sensor Array Utilizing a Novel Sensing Concept. Sensors and Actuators A: Physical, 135(2):593–597, 2007.

G. Lim, K. Minami, M. Sugihara, M. Uchiyama, and M. Esashi. Active catheter with multi-link structure based on silicon micromachining. In Micro Electro Mechanical Systems 1995, (MEMS '95), Proceedings of the 1995 IEEE Conference on, pages 116–121, Amsterdam, Netherland, 1995.

G. Lim, K. T. Park, M. Sugihara, K. Minami, and M. Esashi. Future of active catheters. Sensors and Actuators A: Physical, 56(1-2):113–121, 1996.

Liwei Lin, Roger T Howe, and Albert P Pisano. A Passive, in Situ Micro Strain Gauge. In Micro Electro Mechanical Systems 1993, Proceedings An Investigation of Micro Structures, Sensors, Actuators, Machines and Systems. IEEE., pages 201–206, Fort Lauderdale, FL, USA, 1993.

Liwei Lin, Albert P Pisano, and R Howe. A Micro Strain Gauge with Mechanical Amplifier. Journal of Microelectromechanical Systems, 6(4):313–321, 1997.

N. Ma, G. Song, and H. J. Lee. Position control of shape memory alloy actuators with internal electrical resistance feedback using neural networks. Smart Materials and Structures, 13(4): 777–783, 2004.

S. Maeda, K. Abe, K. Yamamoto, O. Tohyama, and H. Ito. Active endoscope with SMA (Shape Memory Alloy) coil springs. In Micro Electro Mechanical Systems 1996, (MEMS '96), Proceedings of the IEEE An Investigation of Micro Structures, Sensors, Actuators, Machines and Systems, pages 290–295, San Diego, CA, USA, 1996.

S. Majima, K. Kodama, and T. Hasegawa. Modeling of shape memory alloy actuator and tracking control system with the model. Control Systems Technology, IEEE Transactions on, 9(1):54–59, 2001.

Lisa C Martin, John D Wrbanek, and Gustave C Fralick. Thin Film Sensors for Surface Measurements. Technical report, NASA John H. Glenn Research Center at Lewis Field Cleveland, Ohio, Handnover, MD, USA, 2001.

Greig L. McCreery, Ana Luisa Trejos, Rajni V Patel, Michael D. Naish, and Richard a. Malthaner. Evaluation of Force Feedback Requirements for Minimally Invasive Lung Tumour Localization. In 2007 IEEE/RSJ International Conference on Intelligent Robots and Systems, pages 883–888, San Diego, CA, USA, 2007.

G. T. Mearini and R. W. Hoffman. Tensile properties of aluminum/alumina multi-layered thin films. Electronics Materials, Journal of, 22(6):623–629, 1993.

S. M. Melle, K Liu, and R. M. Measures. A Passive Wavelength Demodulation System for Guided-Wave Bragg Grating Sensors. Photonics Technology Letters, IEEE, 4(5):516–518, 1992.

T. Mineta, T. Mitsui, Y. Watanabe, S. Kobayashi, Y. Haga, and M. Esashi. Batch fabricated flat winding shape memory alloy actuator for active catheter. In Micro Electro Mechanical Systems 2000, (MEMS '00), Proceedings of the Thirteenth Annual IEEE International Conference on, pages 375–380, Miyazaki, Japan, 2000.

W. W. Morey, G. Meltz, and W. H. Glenn. Fiber Optic Bragg Grating Sensors. Proceeding of SPIE: Fiber Optic and Laser Sensors VII, 1169:98–107, 1989.

Liya Ni and David W L Wang. A gain-switching control scheme for position-error-based bilateral teleoperation: Contact stability analysis and controller design. The International Journal of Robotics Research, 23(3):255–274, 2004.

Chi Shiang Pan and Wensyang Hsu. A Microstructure for In Situ Determination of Residual Strain. Microelectromechanical Systems, Journal of, 8(2):200–207, 1999.

K. T. Park and M. Esashi. A multilink active catheter with polyimide-based integrated cmos interface circuits. Microelectromechanical Systems, Journal of, 8(4):349–357, 1999.

H. J. Patrick, G. M. William, A. D. Kersey, J. R. Pedrazzani, and A. M. Vengsarkar. Hybrid Fiber Bragg Grating/Long Period Fiber Grating Sensor for Strain/Temperature Discrimination. Photonics Technology Letters, IEEE, 8(9):1223–1225, 1996.

Jan Peirs, Joeri Clijnen, Dominiek Reynaerts, Hendrik Van Brussel, Paul Herijgers, Brecht Corteville, and Sarah Boone. A Micro Optical Force Sensor for Force Feedback During Minimally Invasive Robotic Surgery. Sensors and Actuators A: Physical, 115(2-3):447–455, 2004.

O. Piccin, L. Barb e, B Bayle, M De Mathelin, and A Gangi. A Force Feedback Teleoperated Needle Insertion Device for Percutaneous Procedures. The International Journal of Robotics Research, 28(9):1154–1168, 2009.

L Que, M Li, L Chu, and Y Gianchandani. A Micromachined Strain Sensor with Differential Capacitive Readout. In Micro Electro Mechanical Systems, 1999. MEMS '99. Twelfth IEEE International Conference on, pages 552–557, Orlando, FL, USA, 1999.

R. A. Russell and R. B. Gorbet. Improving the response of SMA actuators. In Robotics and Automation 1995, Proceedings of the 1995 IEEE International Conference on, volume 3, pages 2299–2304, Nagoya, Japan, 1995.

Alana Sherman, Murat Cenk Cavusoglu, and Frank Tendick. Comparison of Teleoperator Control Architectures for Palpation Task. In Symposium on Haptic Interfaces for Virtual Environments and Teleoperator Systems. ASME, pages 1–8, Orlando, FL, USA, 2000. Citeseer.

Gang Song and Shuxiang Guo. A Novel Force Feedback-based Teleoperation System for Medical Application. International Journal of Innovative Computing, Information and Control, 3(3): 737–750, 2007.

R J Stephen, K Rajanna, Vivek Dhar, K G K Kumar, and S Nagabushanam. Thin-film Strain Gauge Sensors for Ion Thrust Measurement. Sensors Journal, IEEE, 4(3):373–377, 2004.

H. Takizawa, H. Tosaka, R. Ohta, S. Kaneko, and Y. Ueda. Development of a microfine active bending catheter equipped with mif tactile sensors. In Micro Electro Mechanical Systems 1999, (MEMS '99), Proceeding of the Twelfth IEEE International Conference on, pages 412–417, Orlando, FL, USA, 1999.

M Tavakoli, R V Patel, and M Moallem. Haptic Interaction in Robot-assisted Endoscopic Surgery: A Sensorized End-effector. The International Journal of Medical Robotics and Computer Assisted Surgery, 1(2):53–63, 2005.

N. Troisfontaine, P. Bidaud, and P. Dario. Control experiments on two SMA based micro-actuators. In Experimental Robotics V, The Fifth International Symposium on, pages 490–499, Barcelona, Spain, 1997.

Christopher R Wagner, Nicholas Stylopoulos, and Robert D Howe. The Role of Force Feedback in Surgery: Analysis of Blunt Dissection. In Haptic Interfaces for Virtual Environment and Teleoperator Systems, 2002. HAPTICS 2002. Proceedings. 10th Symposium on, pages 68–74, Orlando, FL, USA, 2002.

Christopher R Wagner, Nicholas Stylopoulos, Patrick G Jackson, and Robert D Howe. The Benefit of Force Feedback in Surgery: Examination of Blunt Dissection. Presence: Teleoperators & Virtual Environments, 16(3):252–262, 2007.

F. Warkusz. The size effect and the temperature coefficient of resistance in thin films. Journal of Physics D: Applied Physics, 11(5):689–694, 1978.

G. R. Witt. The Electromechanical Properties of Thin Films and the Thin Film Strain Gauge. Thin Solid Films, 22(2):133–156, 1974.

John D Wrbanek, Gustave C Fralick, Lisa C Martin, and Charles A Blaha. A Thin Film Multifunction Sensor for Harsh Environments. Technical report, NASA John H. Glenn Research Center at Lewis Field Cleveland, Ohio, Handnover, MD, USA, 2001.

Appendix A

Stability and Minimum Phase Dynamic Analysis of $\frac{V_s}{V_h}$

A.1 $\frac{V_s}{V_h}$ Models with Two Poles

Let: $\alpha_1, \alpha_2, \gamma_1, \gamma_2 \in \Re$ and > 0, $\gamma_1 + \gamma_2 = 1$, and $G_s = \frac{\Delta V_s/V_h}{\Delta P}$

$$\begin{aligned}\frac{V_s}{V_h} &= G_s\left(\frac{\gamma_1}{\alpha_1 s+1}+\frac{\gamma_2}{\alpha_2 s+1}\right)\Delta P\\ &= G_s\left(\frac{(\gamma_1\alpha_2+\gamma_2\alpha_1)s+(\gamma_1+\gamma_2)}{(\alpha_1 s+1)(\alpha_2 s+1)}\right)\end{aligned}$$

$\frac{V_s}{V_h}$ is stable with poles at $-\frac{1}{\alpha_1}, -\frac{1}{\alpha_2}$ and it is minimum phase with zero at $-\frac{(\gamma_1+\gamma_2)}{(\gamma_1\alpha_2+\gamma_2\alpha_1)}$.

A.2 $\frac{V_s}{V_h}$ Models with Three Poles

Let: $\alpha_1, \alpha_2, \alpha_3, \gamma_1, \gamma_2, \gamma_3 \in \Re$ and > 0, $\gamma_1 + \gamma_2 + \gamma_3 = 1$, and $G_s = \frac{\Delta V_s/V_h}{\Delta P}$

$$\begin{aligned}\frac{V_s}{V_h} &= G_s\left(\frac{\gamma_1}{\alpha_1 s+1}+\frac{\gamma_2}{\alpha_2 s+1}+\frac{\gamma_3}{\alpha_3 s+1}\right)\Delta P\\ &= G_s\left(\frac{as^2+bs+c}{(\alpha_1 s+1)(\alpha_2 s+1)(\alpha_3 s+1)}\right)\Delta P\end{aligned}$$

Where:

$$a = \gamma_1\alpha_2\alpha_3 + \gamma_2\alpha_1\alpha_3 + \gamma_3\alpha_1\alpha_2$$

$$b = \gamma_1(\alpha_2+\alpha_3) + \gamma_2(\alpha_1+\alpha_3) + \gamma_3(\alpha_1+\alpha_2)$$

$$c = \gamma_1 + \gamma_2 + \gamma_3$$

$\frac{V_s}{V_h}$ is stable with poles at $-\frac{1}{\alpha_1}, -\frac{1}{\alpha_2}, -\frac{1}{\alpha_3}$ and zeros at $\frac{-b\pm\sqrt{b^2-4ac}}{2a}$. However, it is not obvious that these zeros are in the left or right half of the complex plane. One method to determine the location of these zeros is to use Routh-Hurwitz stability criterion. For second-order polynomial $P(s) = as^2 + bs + c$, all roots are in the left half complex plane when $a, b, c > 0$. Therefore, $\frac{V_s}{V_h}$ model is minimum phase because a, b, and c are greater than 0.

A.3 $\frac{V_s}{V_h}$ Models with Four Poles

Let: $\alpha_1, \alpha_2, \alpha_3, \alpha_4, \gamma_1, \gamma_2, \gamma_3, \gamma_4 \in \Re$ and > 0, $\gamma_1 + \gamma_2 + \gamma_3 + \gamma_4 = 1$, and $G_s = \frac{\Delta V_s/V_h}{\Delta P}$

$$\begin{aligned}\frac{V_s}{V_h} &= G_s\left(\frac{\gamma_1}{\alpha_1 s+1} + \frac{\gamma_2}{\alpha_2 s+1} + \frac{\gamma_3}{\alpha_3 s+1} + \frac{\gamma_4}{\alpha_4 s+1}\right)\Delta P \\ &= G_s\left(\frac{as^3 + bs^2 + cs + d}{(\alpha_1 s+1)(\alpha_2 s+1)(\alpha_3 s+1)(\alpha_4 s+1)}\right)\Delta P\end{aligned}$$

Where:

$a = \gamma_1\alpha_2\alpha_3\alpha_4 + \gamma_2\alpha_1\alpha_3\alpha_4 + \gamma_3\alpha_1\alpha_2\alpha_4 + \gamma_4\alpha_1\alpha_2\alpha_3$

$b = \gamma_1(\alpha_2\alpha_3 + \alpha_3\alpha_4 + \alpha_2\alpha_4) + \gamma_2(\alpha_1\alpha_3 + \alpha_3\alpha_4 + \alpha_1\alpha_4) + \gamma_3(\alpha_1\alpha_2 + \alpha_2\alpha_4 + \alpha_1\alpha_4) + \gamma_4(\alpha_1\alpha_2 + \alpha_2\alpha_3 + \alpha_1\alpha_3)$

$c = \gamma_1(\alpha_2 + \alpha_3 + \alpha_4) + \gamma_2(\alpha_1 + \alpha_3 + \alpha_4) + \gamma_3(\alpha_1 + \alpha_2 + \alpha_4) + \gamma_4(\alpha_1 + \alpha_2 + \alpha_3)$

$d = \gamma_1 + \gamma_2 + \gamma_3 + \gamma_4$

$\frac{V_s}{V_h}$ model is stable because it has poles at $-\frac{1}{\alpha_1}, -\frac{1}{\alpha_2}, -\frac{1}{\alpha_3}, -\frac{1}{\alpha_4}$. From Routh-Hurwitz stability criterion, third-order polynomial $P(s) = as^3 + bs^2 + cs + d$, all roots are in the left half complex plane when $a, b, c, d > 0$. and $bc > ad$. Therefore, $\frac{V_s}{V_h}$ model is minimum phase because a, b, c, and d are greater than 0 and $bc - ad > 0$.